Experimental Quantum Information Processing with Photons

by

Jonathan Lavoie

A thesis
presented to the University of Waterloo
in fulfillment of the
thesis requirement for the degree of
Doctor of Philosophy
in
Physics

Waterloo, Ontario, Canada, 2013

I hereby declare that I am the sole author of this thesis. This is a true copy of the thesis, including any required final revisions, as accepted by my examiners.

I understand that my thesis may be made electronically available to the public.

Abstract

This thesis describes experimental generation, manipulation and measurement of quantum information using photon pairs emitted in bulk crystals. Multi-photon sources engineered during the course of this thesis have proven to be ideal for original contributions in the field of optical quantum information.

In the first part of this dissertation, we study nonlocality, bound entanglement and measurement-based quantum computing using entangled resources produced by our source. First, we produced and characterised three-photon GHZ polarisation states. We then experimentally violate the long-standing Svetlichny's inequality with a value of 4.51 ± 0.14, which is greater than the classical bound by 3.6 standard deviations. Our results agree with the predictions of quantum mechanics, rule out nonlocal hidden-variable theories and certify the genuine tripartite entanglement achievable by our source. Second, with four-photon polarisation states, we demonstrate bound entanglement in Smolin states and realize all of their conceptually important characteristics. Our results highlight the difficulties to achieve the critical condition of undistillability without completely losing entanglement. We conclude the first part by simulating, for the first time, valence-bond solid states and use them as a resource for measurement-based quantum computing. Affleck-Kennedy-Lieb-Tasaki states are produced with 87% fidelity and single-qubit quantum logic gates reach an average fidelity of 92 % over all input states and rotations.

In the second part of this dissertation, we explore controlled waveform manipulation at the single-photon level. Specifically, we shrink the spectral bandwidth of a single photon from 1740 GHz to 43 GHz and demonstrate tunability over a range 70 times that bandwidth. The results are a considerable addition to the field of quantum frequency conversion and have genuine potential for technological applications.

Acknowledgements

There are many colleagues and friends I should thank for having made my graduate studies an unforgettable experience. First, thanks to Kevin Resch and the Quantum Optics and Quantum Information Group at the Institute for Quantum Computing (IQC). I could not have chosen a better environment to start my career. Specifically, thanks to Rainer Kaltenbaek, Deny Hamel, Kent Fisher, John Donohue, Mike Mazurek, Robert Prevedel, Krister Shalm, Logan Wright, Megan Agnew, Lydia Vermeyden and Madeleine Bonsma for the good time in the lab, for all our valuable discussions, and for your help any time it was needed. I also acknowledge help, advice and fruitful collaborations with Marco Piani, Norbert Lütkenhaus, Alessandro Fedrizzi, Bei Zeng, Rolf Horn, Aimee Heinrichs, Catherine Holloway, Juan Miguel Arrazola, Oleg Gittsovich, Martin Laforest, Osama Moussa, Piotr Kolenderski and Chris Erven with everyone from the "GHZ experiment".

I thank Raymond Laflamme, Michele Mosca and all the supporting staff and members of IQC for making this institute a world-class facility to study and control the weirdness of quantum mechanics. Thanks to Matt Cooper, Steve Weiss and Vito Logiudice for their technical support, advice and pleasant discussions. I also appreciate the support from the Department of Physics, especially from Judy McDonnell for her administrative assistance during all my graduate studies.

I made a lot of close friends in Waterloo and I particularly thank Troy, Oleg, Kasia, Peter, Jean-Luc, Florian, Audrey, Agnes, Ansis, Yuval, Kasia S., Aharon, Claire, Tomas JOC, Robert K., Laura, Jacek, Barbara, Diana, Irina, Josef, Anastasia, Yoah, Johan, Mada and Alex for their good company. I will carry your friendship with me anywhere I am. I also thank all my family for their support and understanding that each step I make away from them also brings me closer to my final goals.

I am sincerely grateful to financial help from the Natural Sciences and Engineering Research Council of Canada (NSERC), the Department of Physics & Astronomy, IQC and the Ontario Graduate Scholarship Program (OGS).

A very special thank you to Florian Ong for his useful comments on this thesis, and to the members of my committee for their time and support: Kevin Resch, Donna Strickland, Thomas Jennewein, Dayan Ban and Paul Kwiat.

Table of Contents

List of Tables

List of Figures

List of Abbreviations

Symbol	Synonym	Definition
$\|A\rangle$	$\|-\rangle$, $\|-45°\rangle$	Anti-diagonally polarised photon
$\|D\rangle$	$\|+\rangle$, $\|45°\rangle$	Diagonally polarised photon
$\|H\rangle$		Horizontally polarised photon
$\|V\rangle$		Vertically polarised photon
$\|L\rangle$	$\|\circlearrowleft\rangle$	Left-circular polarised photon
$\|R\rangle$	$\|\circlearrowright\rangle$	Right-circular polarised photon
AKLT		Affleck-Kennedy-Lieb-Tasaki
APD		Avalanche photodiode
BBO		β-Barium-Borate
Bell states	$\|\phi^{\pm}\rangle$, $\|\psi^{\pm}\rangle$	$\frac{1}{\sqrt{2}}(\|HH\rangle \pm \|VV\rangle)$, $\frac{1}{\sqrt{2}}(\|HV\rangle \pm \|VH\rangle)$
BiBO		Bismuth-Borate
BS		Beam-splitter
CHSH		Clauser-Horne-Shimony-Holt
FWHM		Full-width at half maximum
GHZ		Greenberger-Horne-Zeilinger
HOM		Hong-Ou-Mandel
HWP	$\lambda/2$	Half-wave plate
LCR		Liquid crystal retarder
LHV		Local hidden-variable
LOCC		Local operations and classical communication
X, Y, Z	σ_x, σ_y, σ_z	Pauli matrices
PBS		Polarising beam-splitter
PMT		Photomultiplier tube
PPT		Positive under partial transposition
QM		Quantum mechanics
QST		Quantum state tomography
QWP	$\lambda/4$	Quarter-wave plate
RMS		Root mean square
SFG		Sum-frequency generation
SPDC		Spontaneous parametric downconversion

Chapter 1

Overview

One Source to create them all, One Source to study them
One Source to publish them all, and in this thesis bind them

From the Lab of IQC where the Shadows lie

In this thesis, we discuss the experimental generation and manipulation of correlated photon pairs from spontaneous parametric downconversion (SPDC), in bulk crystals. We control photonic quantum states to experimentally explore diverse topics at the heart of quantum information science. First, we encode information onto multi-photon polarisation states, to investigate nonlocal realistic models and demonstrate the first violation of Svetlichny's inequality. Second, we produce and characterise Smolin bound-entangled states, a family of "noisy" quantum states, which entanglement cannot be purified, but yet attractive for some communication tasks. Third, using four-photon polarisation states and linear optical elements, we demonstrate elementary measurement-based information processing gates with a simulated valence-bond solid, an entangled resource state distinct from the orthodox *cluster states*. Finally, we successfully tailor the waveform of a single photon by converting its energy and manipulating its spectral bandwidth. Our SPDC source of photonic states is ideal to study those topics central to quantum information: nonlocality, entanglement, quantum computation and communication.

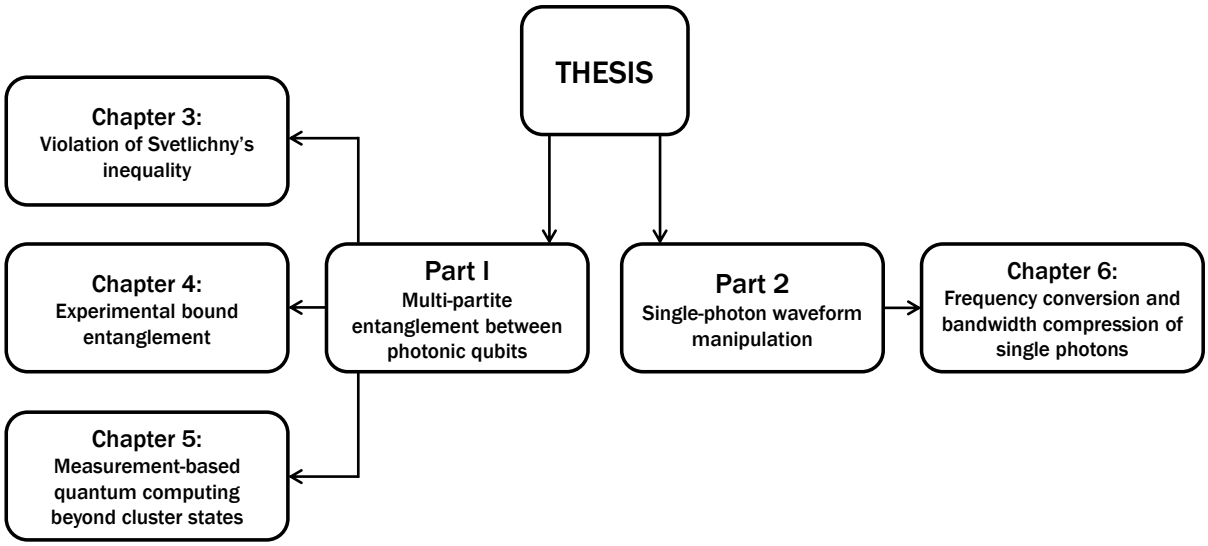

1.1 Quantum information science

Quantum information science [2, 3, 4, 5] deals with processing and exchanging information by fully taking advantage of the laws of quantum mechanics. This is a new paradigm predicted to revolutionize the way we process information. The main research areas in this field include quantum computing, quantum simulation, quantum communication and metrology.

A quantum computer is a device performing quantum information processing. In analogy with the "bits" of today's (classical) computers, quantum bits, or qubits, are the fundamental bricks of quantum computing. Unlike classical bits whose value is either 0 or 1, qubits can be placed in a *superposition* of these two states. A systematic series of gates on qubits in a superposition can run calculations in parallel, increasing the computation speed of quantum computers exponentially. It has been shown theoretically that such computers could in consequence solve certain problems more efficiently than their

classical counterpart. For example, public key cryptosystems rely on the difficulty of finding the prime factors of an integer, for which no efficient algorithm exists on a classical computer [2]. Using the laws of quantum mechanics, Peter Shor proposed a fast quantum algorithm [6] for factoring that could jeopardize everyday's encrypted transactions if implemented. Another efficient algorithm is from Lov Grover, who showed how a quantum computer could speed up a search conducted through an unstructured data base [7]. Seminal works from Shor and Glover are examples of algorithms which stimulated research in quantum computing. Another major application of quantum computers is the possibility to efficiently simulate other quantum systems [8], something that classical computers can't do efficiently in many interesting and important cases [2].

While the theory of computing with quantum systems predicts higher communication and computation power, its physical implementation remains a formidable challenge. Some requirements, known as the DiVincenzo criteria, were proposed for implementing quantum computation [9]. The physical system should be scalable with well characterized qubits, which can be initialized to any state. It should also be possible to apply a set of *universal* gates [10], acting upon the physical system faster than decoherence times [11]. Finally, it should be possible to interact with any specific qubit, a crucial step to measure the result of a computation. Several physical systems are close to fulfill those requirements. Among the most promising implementations of a quantum computer stand trapped ions [12], NV centers in diamond [13], phosphorus-doped silicon [14], superconducting circuits [15] and optical implementations [16].

Communication using the laws of quantum mechanics is an important branch of quantum information science. The protocols are relatively less involved than the computation part, and use "flying qubits", which generally consist of photons. It is possible to transmit two classical bits of information, while transmitting only one quantum bit with the superdense coding protocol [17, 18, 19] or to *teleport* a quantum bit between two remote locations [20, 21]. Quantum cryptography is a noticeable application of quantum information. Quantum key distribution (QKD) is the most mature technology, and commercially available. This technology allows one to distribute a sequence of qubits (photons) to construct a secret key [22] over a public channel, whose secrecy is guaranteed by fundamental rules of quantum mechanics [23].

1.2 Nonlocality and Bell's inequalities

In quantum mechanics (QM), we represent the state of a quantum system with a unit *ket* vector, $|\psi\rangle$, in a vector space. A qubit, for example, is the most basic quantum mechanical system: a state represented by $|0\rangle$, $|1\rangle$ or in a superposition of $|0\rangle$ and $|1\rangle$. A system can be composed of more than one particle (qubit). For a particle in a state $|\psi_A\rangle$ and another in the state $|\psi_B\rangle$, the *separable* bi-partite system is described by

$$|\psi_{AB}\rangle = |\psi_A\rangle \otimes |\psi_B\rangle, \tag{1.1}$$

where $\otimes$ designates the tensor product. For example, if $|\psi_{AB}\rangle = \frac{1}{2}(|0_A\rangle \otimes |0_B\rangle + |0_A\rangle \otimes |1_B\rangle + |1_A\rangle \otimes |0_B\rangle + |1_A\rangle \otimes |1_B\rangle)$, then it is clear that $|\psi_A\rangle = \frac{1}{\sqrt{2}}(|0\rangle + |1\rangle) = |\psi_B\rangle$. What does it mean if the state is described by

$$|\psi_{AB}\rangle = \frac{1}{\sqrt{2}}(|0_A\rangle \otimes |1_B\rangle - |1_A\rangle \otimes |0_B\rangle)^{1}? \tag{1.2}$$

Such state cannot be factorized in a form $|\psi_A\rangle \otimes |\psi_B\rangle$, for any $|\psi_A\rangle$ and $|\psi_B\rangle$. In general, when a composite quantum state has no factorable representation, it is said to be *entangled*.

The concept of *nonlocality* was introduced before the advent of quantum information science. It finds its roots in the existence of entangled states. Consequences of such states in the quantum world led Einstein, Podolsky and Rosen (EPR) [24], in 1935, to criticise the (in)completeness of QM. Here is how one could summarize the EPR argument of incompleteness of QM [2].

Let's consider two distant particles, A and B, jointly described by the entangled state in Eq. 1.2, and an observable σ_z, with eigenstates $|0\rangle$ and $|1\rangle$ and corresponding eigenvalues $+1$ and -1, i.e., $\hat{\sigma}_z|0\rangle = |0\rangle$ and $\hat{\sigma}_z|1\rangle = -|1\rangle$. In QM, an observable ($\sigma_z$) is a physical quantity that can be measured[3] and represented by an Hermitian matrix operator, here $\hat{\sigma}_z$. The possible measurement results of an observable are the eigenvalues of this operator.

[1] This state is called the Singlet state.

[2] Our simplified description is not exactly the same as the original EPR's but contains the essence of their main arguments and follows the interpretation of Redhead [25].

[3] For example position, momentum, angular momentum, spin, polarisation, etc, ...

We choose to measure σ_z^A on system A and get one of two outcomes. If the outcome was $+1$ the joint state is reduced to $|0_A\rangle \otimes |1_B\rangle$, or to $|1_A\rangle \otimes |0_B\rangle$ if the outcome was -1. The state of system B is then perfectly known (with probability 1) to an observer, with an eigenvalue given by λ_z^B, corresponding to $+1$ or -1 depending on the outcome of A. According to EPR, the state of system B, the *element of reality*, exists and has a sharp value. From their *locality* principle, all elements of reality belonging to one system should not be affected by measurements made on another system, especially *at a distance*. Because what is done on system A cannot affect the state on B, this sharp value λ_z^B can be brought back in time, when the system was still in the singlet state $|\psi_{AB}\rangle$ of Eq. 1.2; by the EPR locality principle, λ_z^B exists at that time. The Copenhagen complementary interpretation of QM tells us that if a system is *not* in an eigenstate of an observable, then the value of that observable is undefined, or even "meaningless" [26]. Since $|\psi_{AB}\rangle$ is not an eigenstate of σ_z^B, this contradicts the sharp value from the locality argument. In fact, for the singlet state, the state of B is inherently random. According to EPR, fixing this *paradox* by relaxing their locality principle would be unphysical and therefore, QM has to be incomplete.

How do we "complete" QM then? One alternative is to use the realist interpretation of QM that incorporates hidden variables. In this view, all observables, in all states, have sharp values waiting to be revealed. When supplemented with the locality principle, and considering two distant particles, realism and locality (the local hidden-variable (LHV) model) imply Bell's inequality. In response to EPR, the first inequality [27] from measurable correlation coefficients was derived by John Bell in 1964. However, the "most famous" Bell's inequality is from 1969 by John Clauser, Michael Horne, Abner Shimony and Richard Holt (CHSH), which can be tested experimentally [28]. We assume a source emitting pairs of particles travelling in opposite directions towards their measurement station, A and B, respectively. The setup is illustrated in Fig. 1.1. The source emits two entangled single photons travelling in opposite directions, and each measurement device measures the polarisation-projection along any direction, for example the horizontal-vertical "direction". There are two directions (measurement settings) for A $(\mathbf{a}, \mathbf{a}')$ and two for B $(\mathbf{b}, \mathbf{b}')$ and the outcome of the n^{th} single measurement (a_n, a'_n, b_n, b'_n) for each is restricted to ± 1. We

can form the expression

$$\Gamma_n = a_n b_n + a_n b'_n + a'_n b_n - a'_n b'_n. \tag{1.3}$$

If we rearrange Eq. 1.3 into

$$a_n(b_n + b'_n) + a'_n(b_n - b'_n) \tag{1.4}$$

it is easy to see that the value of Γ_n can only be $+2$ or -2, because if $b_n + b'_n = 2$, then $b_n - b'_n = 0$ and vice-versa. What is more subtle though, is that there is a crucial assumption (and essential ingredient for our derivation) when going from Eq. 1.3 to Eq. 1.4: we assume that the (sharp) value of a_n (or a'_n) is the same whether b_n or b'_n is measured. In other words, we assume that the settings of B do not affect a_n. This is the *locality* assumption, and the sharp value of each term in Eq 1.3 is assuming *realism*.

Correlation coefficients are defined by considering N events (an event is the source producing one pair followed by a polarisation-measurement on both sides), and calculating the average value of Γ

$$\left| \frac{1}{N} \sum_{n=1}^{N} \Gamma_n \right| = \left| \frac{1}{N} \sum_{n=1}^{N} a_n b_n + \ldots \right| \tag{1.5}$$

Since $\Gamma_n = \pm 2$, we have that LHS≤ 2, and each term in the RHS is a correlation coefficient, e.g.

$$c(\mathbf{a}, \mathbf{b}) = \lim_{N \to \infty} \frac{1}{N} \sum_{n=1}^{N} a_n b_n. \tag{1.6}$$

The inequality given by

$$|c(\mathbf{a}, \mathbf{b}) + c(\mathbf{a}, \mathbf{b}') + c(\mathbf{a}', \mathbf{b}) - c(\mathbf{a}', \mathbf{b}')| \leq 2$$

is the CHSH-Bell inequality. If we now specify the state being produced each time by the source, for example singlet states, it can be shown that with a suitable set of measurement settings, quantum mechanics predicts a violation of Eq 1.7. The list of reported experiments in conflict with CHSH-Bell inequalities is extensive (see for example Ref. [29, 30, 31, 32, 33]), and one should conclude that local-hidden variable models are inadequate to describe the correlations present in nature (modulo *loopholes* present in all experiments to date).

Extending LHV models to three particles also lead to Bell inequalities, again in contradiction with QM [34]. However, when more than two particles are involved, the concept

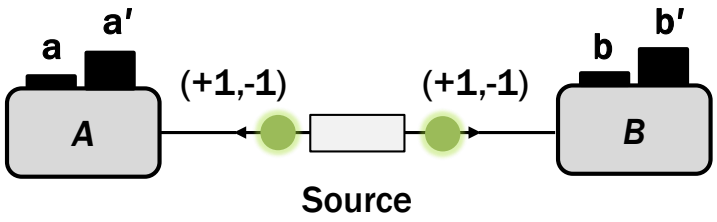

Figure 1.1: **Schematic illustration of a Bell experiment**. The source emits two particles towards station A and B. Measurements parallel to $\mathbf{a}$ and $\mathbf{a}'$, ($\mathbf{b}$ and $\mathbf{b}'$) reveals the state of the particles, ± 1. The experiment is repeated N times and correlations between measurement outcomes are inserted onto Bell's inequality.

of nonlocality is not as simple, because a violation of a three-body Bell-type inequality, for example Mermin's inequality [34], fails to capture the idea of true, or *genuine* multi-partite nonlocality. The observed correlations between measurement outcomes could be explained by a *hybrid* model for which only two particles are nonlocally correlated but not with the third one, illustrated in Fig. 1.2b. The study of multi-partite nonlocality was initiated by Svetlichny [35] in 1987, and his work triggered fundamental questions about the role played by nonlocality in quantum information science [36]. In Chapter 3, we cover the generation of three-body polarisation-entangled states and offer the first experimental violation of Svetlichny's original inequality.

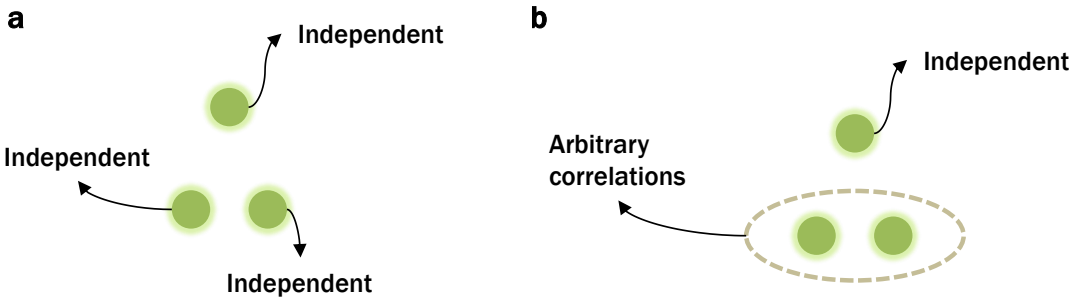

Figure 1.2: **Local vs Nonlocal hidden-variable models**. **a**, LHV models assume a predetermined value of each measurement outcome, on every particle. It also assumes that each outcome is independent of any other measurement settings on remote particles. **b**, Svetlichny's model is a nonlocal hidden-variable model. A subset of two qubits is nonlocally correlated and one qubit is classically correlated with the rest; outcomes on the bipartite subsystem and on the single one are statistically independent from each other. Both models can be experimentally tested.

1.3 The mysterious bound entanglement

Entanglement is a resource for quantum information processing that our source is capable of generating. It is a basis for quantum cryptography, quantum teleportation and quantum computation. Shared entangled resources allow, for example, two parties A and B to obtain a key for encrypted communication [37] or for teleporting information [20] from one side to another. However, entangled *pure* states (describing complete knowledge about the system) may have been polluted by the environment, while distributing the quantum resource. Imperfect correlations will harm any protocol and the resulting states are generally a mixture of pure states described by a *density matrix*:

$$\rho_{AB} = \sum_k p_k |\psi^k\rangle\langle\psi^k| \tag{1.7}$$

where p_k is the probability of the system to be in the pure state $|\psi^k\rangle$. There exists *distillation* algorithms [38] that allow multiple copies of ρ_{AB} to reverse the process of

noise, via local operations and classical communication (LOCC) between A and B, and retrieve entanglement in its pure form. Entangled states which cannot be distilled into pure entanglement, as depicted in Fig. 1.3, are called *bound entangled* [39].

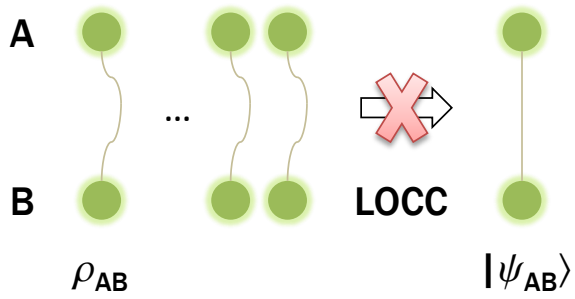

Figure 1.3: **Bound entangled states cannot be distilled**. For bound entangled states, multiple copies of ρ_{AB} shared between A and B cannot lead to a pure entangled state $|\psi_{AB}\rangle$ via LOCC.

Understanding bound entanglement is "one of the deepest problem in quantum information theory and the key to unraveling several mysteries of entanglement" [40]. Our objective in Chapter 4, is to promote bound entangled states from just a curious mathematical construction to an achievable one through experiments. Successful generation and characterisation of bound entangled states shared between four photonic qubits demonstrate the higher degrees of control over our source and highlight once more the role of photonic qubits to reveal mysteries.

1.4 Optical quantum information

Most of optical quantum computation and quantum communication protocols rely on single-photon, and single-photon sources, for which the probability of a multiple-photon emission should be low relative to the probability of a single-photon emission [41]. There

exists different methods for generating flying qubits and real-world sources are not perfect [42]. Single-photon sources can be defined as deterministic, with photons emitted on-demand, or probabilistic. Examples of the former includes single neutral atoms, single ions, single molecules, quantum dots and color centers in diamonds [41]. In the ideal case, those quantized individual system, when triggered, produce one and only one photon into a desired mode with unit efficiency. The ideal single photon source, however, does not exists yet [16]. Probabilistic sources can be more advantageous, since they allow the generation of correlated pairs of photons and can always be used as a deterministic source by *heralding* techniques. In contrast with the triggered single photon source, pairs are generated randomly, Poisson-distributed, and multiple pairs can be produced at each pump pulse. For any type of sources, even if ideal, they are nondeterministic in practice due to the imperfect collection efficiency of the photons produced [16].

One of the most common sources of photon pairs today relies on spontaneous parametric downconversion (SPDC). The emission of photon pairs is caused by a pump laser interacting with a material with a $\chi^{(2)}$ optical nonlinearity. Once photon pairs are generated from SPDC, information encoding is not limited to polarisation, but can also rely on different degrees of freedom, for example time bin, or path encoding [43]. Other photon sources, including photon pairs generation in waveguides, four-wave mixing in fibers, or other unique techniques are discussed in Ref. [41].

Single photons are so far the best media to encode and transmit quantum information for quantum communication protocols: they travel at the speed of light, interact weakly with their environment, and can be manipulated with linear optics. SPDC sources were used to demonstrate quantum key distribution with the polarisation degree of freedom [22] or with time bins [44]. Communication over several kilometers in free-space was demonstrated [45] and the door is now open to operations between ground and satellites in low earth orbit [46]. Single photons can also be transmitted over long distances inside optical fiber [47], but since loss increase with distance, the use of quantum repeaters become essential. The role of quantum repeater protocols is to reduce loss and decoherence during transmission of quantum states over long distances. A quantum repeater typically consists of quantum memories, for example atomic ensembles [48], and relies on entanglement swapping [49]. Detectors also play a key role in optical quantum communication, especially

for the reliability of quantum key distribution protocols and long distance communication. For a comprehensive review on single-photon detectors see Ref. [41].

In section 1.1 we mentioned possible physical architectures for quantum information processing, mostly in solid-state devices. Optical approaches to quantum computation are also attractive due to the weak interaction of photons with the environment and straightforward manipulations with linear optical elements. An important breakthrough from Knill, Laflamme and Milburn (KLM) showed that quantum computation with only linear optical elements was possible, and efficient [50]. Quantum computation with the KLM scheme is modeled with the quantum *circuit model*, for which qubits are initialized and subjected to a sequence of quantum logic gates, and finally measured. This is illustrated in Fig 1.4a and common to most of physical implementations. Measurement-based quantum computation (MBQC) is a different model for which computation is executed with projective measurements on highly entangled resource states, the cluster states [51]. MBQC on cluster states represents an appealing alternative approach with advantages [52] over the linear optical quantum computing [43]. The general scheme is illustrated in Fig. 1.4b. Cluster states were experimentally generated using photonic qubits, and successful measurement-based computation demonstrated [53, 54].

One very appealing candidate for quantum computer uses a quantum state first described by Affleck, Kennedy, Lieb, and Tasaki (AKLT), and found by cooling down the right solid-state system to its ground state. By addressing the individual spin-systems in the solid, it has been shown theoretically that quantum information could be encoded, manipulated and extracted. Similarly to cluster states, AKLT states rely on the measurement-based model (also called one-way model) for computation (sketched in Fig. 1.4b). AKLT is a one-dimensional chain of qutrits (three-level) which encodes one logical qubit. In Chapter 5 we devised the means to construct the AKLT state by using our source of photonic qubits. Since the system is optics, rather than solid-state, our approach uses linear optical components rather than cooling. Our implementation is an example of how a quantum system, e.g. a solid state, can be simulated with another, here an entangled multi-partite photonic state.

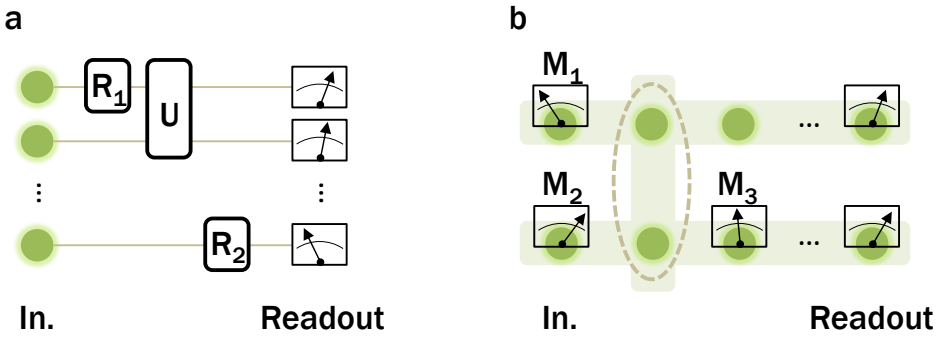

Figure 1.4: **Models for universal quantum computing**. **a**, In the circuit model, computation proceeds by first initializing (In.) independent qubits and dynamically altering their states via unitary single-qubit gates (R_i) and gates between the qubits (U). After computation, i.e. concatenation of all one-qubit and two-qubit gates, the result is extracted by performing appropriate measurements on the final state (readout). **b**, In the measurement-based scheme, information processing follows by single-qubit *projective measurements* (M_i) and also involves coupling interactions. The main difference with the circuit model is that each wire (horizontal line) is initially in an highly entangled state and encodes one logical qubit. For computation to be universal, wires must be coupled at the right moment.

1.5 Quantum frequency conversion

Quantum frequency conversion (QFC) is the quantum version of optical frequency conversion [55]. It relies on nonlinear interactions to convert the carrier frequency of quantum states of light, while maintaining its quantum characteristics. It was first proposed [56] and experimentally demonstrated [57] by Prem Kumar and colleagues. QFC has technological importance for different applications but here we frame our discussion in the context of quantum information transfer among different media for communication, detection and storage.

Quantum information processing and communication systems of the future will most likely be composed of different types of physical architecture [58]. Such an hybrid *network*

(see Fig. 1.5) could be made of photonic quantum emitters, waveguides and processors or quantum memories. Each computational node absorbs and emits photons (holding the quantum information) at its own frequency and spectral bandwidth. For example, the properties of photons emitted from a SPDC source can be very different from the natural resonant frequency and line shape of a quantum memory, or from the optimal frequency for transmission into optical fibers, for which the lowest attenuation is in the infrared (~ 1.5 μm). The different operating frequencies make the nodes incompatible with each other, and information can be lost. Single photon detectors are also better at visible wavelengths [59].

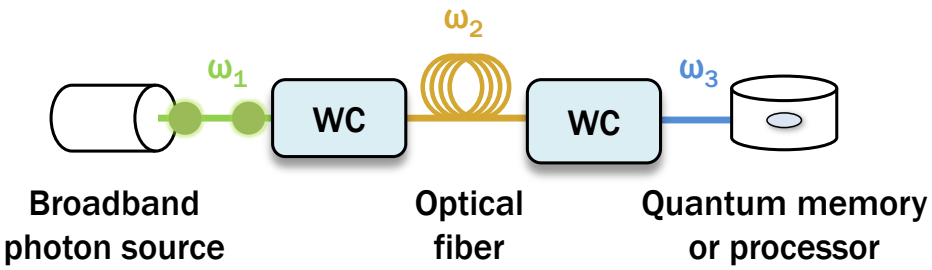

Figure 1.5: **A simplified quantum network**. In this example, a network is composed of a broadband single photon source, an optical fiber and a quantum memory. Each architecture (the nodes) operates at different central frequencies, ω_i. Waveform converters (WC) match the spectral properties and temporal shape between each node to avoid excessive loss.

Quantum communication within the network can be greatly improved by converting single photons from one central frequency to another and tailoring their waveform. The idea of improving detection efficiency by converting infrared light to visible through sum-frequency generation in $\chi^{(2)}$ media has been experimentally observed [60, 61]. Other experiments followed using waveguides [62] or pump-resonant cavity [63] to improve conversion efficiencies. Cascaded upconversion schemes also exist to convert light form infrared to the green band in a two-step upconversion [64]. The first experiment showing successful entanglement-preserving (time-bin) frequency conversion was by Tanzilli and colleagues [65]. Difference-frequency mixing [66] is also attractive for visible-to-telecom

quantum frequency conversions [67, 68, 69]. Four-wave-mixing in $\chi^{(3)}$ media can lead to a frequency *translation* of a smaller amplitude [70], in contrast with the large frequency shifts offered by sum-frequency and difference-frequency generations in $\chi^{(2)}$ media.

This is an exciting field, and many physicists are currently working to manipulate coherent wavepacket states of single photons [71]. Only recently, control over the waveform of single photons, in addition to frequency conversion, was considered. In Ref. [72, 73] the temporal shape of a single-photon is modulated and the pulse duration is reduced, through modulation of a broadband pump. In Chapter 6, we propose and demonstrate a quantum frequency conversion technique complementary to what has been done before, which aims at shrinking the spectral bandwidth of a single photon in a tunable way.

Chapter 2

Related background

This chapter addresses some concepts dealt with in the rest of the thesis.

2.1 Coupled equations for three-wave mixing

Nonlinear optical processes occur in media when the response to an incident electric field is not linear. This topic is covered in many textbooks [74, 55, 1]. The dependence of polarisation of a dielectric upon electric field $E(t)$ may be expressed as a Taylor series [55]

$$P = P_0 + \epsilon_0 \left[\chi^{(1)}E + \chi^{(2)}E^2 + \chi^{(3)}E^3 + \ldots\right], \tag{2.1}$$

where $\chi^{(i)}$ is the susceptibility, treated classically here. A quantum treatment of nonlinear optics can be found in Ref. [75]. $\chi^{(1)}$ belongs to the linear regime, while for the following treatments, we will be interested in the second order term, $\chi^{(2)}$. Note that in Eq. 2.1, we have ignored vectors and will also neglect the detailed expression of $\chi^{(2)}$, which is a tensor of rank 3.

A wave equation can be derived from Maxwell's equations

$$\nabla \times \nabla \times E = -\mu_0\epsilon_0 \frac{\partial^2}{\partial t^2}E - \mu_0 \frac{\partial^2}{\partial t^2}P \tag{2.2}$$

with P given by Eq. 2.1 ($P_0 = 0$), ϵ_0 the permittivity of free space and $\mu_0 = 1/(\epsilon_0 c^2)$. A vector identity and physically motivated assumptions leads to a simplified form of the wave equation. For a dielectric, isotropic and homogeneous medium, and also assuming plane waves traveling along z-direction, Eq. 2.2 becomes [55]

$$\frac{\partial^2}{\partial z^2}E = \frac{\epsilon^{(1)}}{c}\frac{\partial^2}{\partial t^2}E + \frac{1}{c^2}\frac{\partial^2}{\partial t^2}P^{NL}. \tag{2.3}$$

Here, $\epsilon^{(1)} = \epsilon_0(1+\chi^{(1)})$ and $P^{NL} = \chi^{(2)}E^2 + \chi^{(3)}E^3 + \ldots$.

The general case for three-wave mixing has three individual fields of frequency ω_1, ω_2 and ω_3 and for simplicity we assume they are continuous waves

$$E(z,t) = \sum_{n=1}^{3} E_n(z)e^{-i\omega_n t} + c.c. \tag{2.4}$$

$$P^{NL}(z,t) = \sum_{n=1}^{3} P_n^{NL}(z)e^{-i\omega_n t} + c.c. \tag{2.5}$$

Substituting the last two expressions into Eq. 2.3, taking the time derivative and equating terms with the same $e^{-i\omega_n t}$ dependence leads to

$$\frac{\partial^2}{\partial z^2}E_n(z) + \frac{\omega_n^2\epsilon^{(1)}}{c^2}E_n(z) = -\frac{\omega_n^2}{c^2}P_n^{NL}. \tag{2.6}$$

For plane waves, $E_n(z) = A_n e^{ik_n z} + c.c.$, with A_n a slowly varying function, which brings Eq. 2.5 to

$$E(z,t) = \sum_{n=1}^{3} A_n(z)e^{i(k_n z - \omega_n t)} + c.c. \tag{2.7}$$

Note that $k_i = \frac{\omega_i}{c}\sqrt{\epsilon^{(1)}}$.

We now derive the coupled wave equations for sum-frequency generation between three plane waves, with frequency ω_1, ω_2 and $\omega_3 = \omega_1 + \omega_2$. The resultant field in the medium is

$$E(z,t) = A_1 e^{i(k_1 z - \omega_1 t)} + A_2 e^{i(k_2 z - \omega_2 t)} + A_3 e^{i(k_3 z - \omega_3 t)}. \tag{2.8}$$

To find the first coupled equation for radiation at ω_3, we use $P^{NL}(\omega_3, t) = P_3(z)e^{-i\omega_3 t}$, where

$$P_3(z) = 2\chi^{(2)}(\omega_3, \omega_1, \omega_2)A_1(z)A_2(z)e^{i(k_1+k_2)z}. \tag{2.9}$$

We substitute the expressions for $E_3(z)$, $P_3(z)$ into Eq. 2.6 and invoke the slowly varying envelope approximation to find

$$\frac{\partial}{\partial z}A_3 = \frac{i\omega_3^2}{k_3c^2}\chi^{(2)}(\omega_3,\omega_1,\omega_2)A_1(z)A_2(z)e^{i\Delta kz} \tag{2.10}$$

$$= iC_3A_1A_2e^{i\Delta kz}. \tag{2.11}$$

For the last expression, we have defined the wave vector mismatch $\Delta k = k_1 + k_2 - k_3$ and $C_3 = \frac{\omega_3^2\chi^{(2)}}{k_3c^2}$ is a real constant if we restrict our calculations to frequencies for which the loss are negligible.

If we repeat the previous steps, we can also find two more equations for ω_1 & ω_2 and we finally have our set of three coupled wave equations:

$$\frac{\partial}{\partial z}A_1 = iC_1A_3A_2^*e^{-i\Delta kz} \tag{2.12}$$

$$\frac{\partial}{\partial z}A_2 = iC_2A_3A_1^*e^{-i\Delta kz} \tag{2.13}$$

$$\frac{\partial}{\partial z}A_3 = iC_3A_1A_2e^{i\Delta kz}. \tag{2.14}$$

2.1.1 Optical frequency conversion

[1] The coupled wave equation of the previous section can be used to study the frequency up-converter illustrated in Fig. 2.1. A wave of frequency ω_1 (signal) is converted into a wave of higher frequency $\omega_3 = \omega_1 + \omega_2$ by use of a large amplitude field at ω_2.

[1] A simple derivation can be found on page 912 of [1] but we will be using the more general approach of Ref. [55]

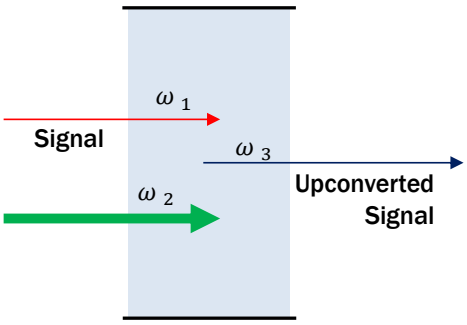

Figure 2.1: **Optical frequency conversion**.

We assume a strong input at ω_2 such that its amplitude does not change appreciably within the interaction. The fields at ω_1 and ω_3 are weak. We incorporate A_2 into constants $\kappa_1 = iC_1A_2^*$ and $\kappa_3 = iC_3A_2$. The three coupled equations become two:

$$\frac{\delta}{\delta z}A_1 = \kappa_1 A_3 e^{-i\Delta kz} \tag{2.15}$$

$$\frac{\delta}{\delta z}A_3 = \kappa_3 A_1 e^{i\Delta kz}. \tag{2.16}$$

The general solutions are derived in section 2.6 of Ref. [55] and correspond to

$$A_1(z) = \frac{A_1(0)e^{-i(\Delta kz/2)}}{g'}\left[i\frac{\Delta k}{2}\sin(g'z) + g'\cos(g'z)\right] \tag{2.17}$$

$$A_3(z) = \frac{\kappa_3 A_1(0)}{g'}e^{i\Delta kz/2}\sin(g'z) \tag{2.18}$$

for $g' = \sqrt{\left(\frac{\Delta k}{2}\right)^2 - \kappa_1\kappa_3}$. The intensity of the upconverted signal is

$$|A_3(z)|^2 = \frac{|A_1(0)|^2|\kappa_3|^2\sin^2(g'z)}{(g')^2} \tag{2.19}$$

$$= \frac{|A_1(0)|^2|\kappa_3|^2}{\left(\frac{\Delta k}{2}\right)^2 - \kappa_1\kappa_3}\sin^2\left(z\sqrt{\left(\frac{\Delta k}{2}\right)^2 - \kappa_1\kappa_3}\right) \tag{2.20}$$

and reaches its maximum at $\Delta k = 0$. The conversion efficiency corresponds to $|A_3(z)|^2/|A_1(0)|^2$.

Our expression in Eq. 2.20 predicts a decrease in the efficiency of the sum-frequency generation process as Δk increases. To satisfy the condition $\Delta k = 0$ is not possible in every material because of dispersion: the refractive index varies with frequency. This is easier to see with second-harmonic generation ($\omega_1 = \omega_2$), but let's assume that $\omega_1 < \omega_2 < \omega_3$ and $\omega_1 + \omega_2 = \omega_3$. $\Delta k = 0$ then implies

$$\begin{aligned} n(\omega_3)\omega_3 &= n(\omega_1)\omega_1 + n(\omega_2)\omega_2 \\ n(\omega_3)\omega_1 + n(\omega_3)\omega_2 &= n(\omega_1)\omega_1 + n(\omega_2)\omega_2 \\ \omega_1 \underbrace{[n(\omega_3) - n(\omega_1)]}_{>0} &= \omega_2 \underbrace{[n(\omega_2) - n(\omega_3)]}_{<0} \end{aligned} \tag{2.21}$$

Equation 2.21 cannot possess a solution, since the two sides have opposite signs.

2.1.2 Phase matching

Phase matching (achieving $\Delta k \cong 0$) can be attained by making use of a material displaying birefringence; a property of non-isotropic materials having an index of refraction dependent on the input field polarisation direction. Two types of phase matching processes are usually considered. In general, Type-I phase matching has the two lowest frequencies having the same polarisation and the higher frequency is orthogonal to them. For Type-II phase matching, the two lowest frequencies have orthogonal polarisation direction to each other while the highest frequency is parallel to one of them. Birefringent crystals are chosen and cut at different angles, depending on the required phase matching. Furthermore, the phase mismatch can be adjusted by angle-tuning or temperature control [55].

When laser pulses are used instead, there are more considerations to take into account, even for a perfect initial phase matching. In general, group velocity mismatch will cause the pulses to lag with respect to each other along the interaction and decreases the frequency-mixing efficiency. Spatial walk-off is also a problem in the case of short pulses or continuous waves, for which each ray propagates at an angle relative to the phase velocity (Ch 15, Ref. [76]).

2.2 Polarisation control and visualisation of photonic qubits

For each single photon traveling in some direction, there are two polarisation modes. For convenience in this thesis, our basis (two orthogonal modes) consists of the horizontally-polarized (**H**) and vertically-polarized modes (**V**). Any pure polarisation state $|\psi_i\rangle$ can thus be described as $\alpha|H\rangle + \beta|V\rangle$, with $|H\rangle$ being a single photon in polarisation mode **H**, and α and β are complex probability amplitudes satisfying $|\alpha|^2 + |\beta|^2 = 1$. Also, the probability that the photon is observed in the **H** (**V**) mode is $|\alpha|^2$ ($|\beta|^2$).

A projector corresponds to $P(|\psi_i\rangle) \equiv |\psi_i\rangle\langle\psi_i|$ and a generic photonic qubit state can also be specified by its density matrix: a convex combination $\rho \equiv \{p_i, P(|\psi_i\rangle)\}$ of projectors. A quantum state is said to be *pure* if $\mathrm{tr}\rho^2 = 1$ and also satisfies $\rho^2 = \rho$. When a state is not pure, i.e., $\mathrm{tr}\rho^2 < 1$, it is *mixed*.

A description of the polarisation in terms of a normalized Jones vector in the H/V basis is handy. We define the most common linear and circular polarisation states encountered in this thesis:

$$|H\rangle = \begin{pmatrix} 1 \\ 0 \end{pmatrix} \qquad |V\rangle = \begin{pmatrix} 0 \\ 1 \end{pmatrix} \tag{2.22}$$

$$|D\rangle = \frac{1}{\sqrt{2}}\begin{pmatrix} 1 \\ 1 \end{pmatrix} \quad |A\rangle = \frac{1}{\sqrt{2}}\begin{pmatrix} 1 \\ -1 \end{pmatrix} \tag{2.23}$$

$$|R\rangle = \frac{1}{\sqrt{2}}\begin{pmatrix} 1 \\ i \end{pmatrix} \quad |L\rangle = \frac{1}{\sqrt{2}}\begin{pmatrix} 1 \\ -i \end{pmatrix} \tag{2.24}$$

Note that 2.22, 2.23 and 2.24 are eigenstates of Pauli σ_z, σ_x and σ_y, respectively, defined as

$$\sigma_x \equiv \begin{pmatrix} 0 & 1 \\ 1 & 0 \end{pmatrix} \quad \sigma_y \equiv \begin{pmatrix} 0 & -i \\ i & 0 \end{pmatrix} \quad \sigma_z \equiv \begin{pmatrix} 1 & 0 \\ 0 & -1 \end{pmatrix}. \tag{2.25}$$

We also have that $\langle H|V\rangle = \langle D|A\rangle = \langle R|L\rangle = 0$.

2.2.1 Polarisation devices

After transmission through a transparent linear optical system, an output photonic qubit state, $|\psi_f\rangle$, is related to an input state $|\psi_i\rangle$ through a transformation (Jones) matrix, T:

$$|\psi_f\rangle = T|\psi_i\rangle. \tag{2.26}$$

Wave retarders (wave plates) are made from birefringent materials and transform the polarisation state of light. They are represented by the matrix

$$T = \begin{pmatrix} 1 & 0 \\ 0 & e^{-i\Gamma} \end{pmatrix} \tag{2.27}$$

with the fast axis along x-direction, illustrated in Fig. 2.2, and Γ is a real number. The velocities of the two polarisation modes differ so that transmission through the plate imparts a relative phase shift Γ to these modes. This phase shift depends on the wavelength, material and the thickness of the crystal (d):

$$\Gamma = 2\pi(n_e - n_o)d/\lambda_0. \tag{2.28}$$

For a specific material, quartz for example, varying the thickness of the wave plate leads to two special cases: $\Gamma = \pi/2$ for a quarter-wave plate (QWP) and $\Gamma = \pi$ for the half-wave plate (HWP).

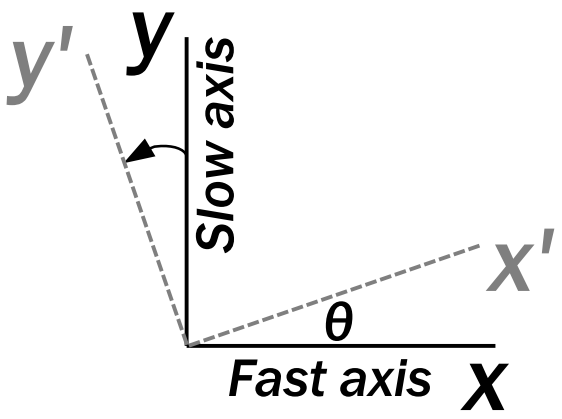

Figure 2.2: **Rotated frame of a retarder** The x-axis is initially along the horizontal-mode of the incident light. After rotation, the fast axis makes an angle θ with the horizontal.

Retarders are usually inserted at normal incidence in the photon path, with their fast axis along the horizontal-mode, and manually rotated as illustrated in Fig. 2.2. The general matrix representation of a rotated wave plate by an angle θ with respect to horizontal is given by

$$T' = \begin{pmatrix} \cos^2(\theta) + e^{-i\Gamma}\sin^2(\theta) & \left(1 - e^{-i\Gamma}\right)\cos(\theta)\sin(\theta) \\ \left(1 - e^{-i\Gamma}\right)\cos(\theta)\sin(\theta) & \sin^2(\theta) + e^{-i\Gamma}\cos^2(\theta) \end{pmatrix}. \tag{2.29}$$

For QWP and HWP, we find

$$QWP(\theta) = \begin{pmatrix} \cos^2(\theta) - i\sin^2(\theta) & (1+i)\cos(\theta)\sin(\theta) \\ (1+i)\cos(\theta)\sin(\theta) & \sin^2(\theta) - i\cos^2(\theta) \end{pmatrix} \tag{2.30}$$

$$HWP(\theta') = \begin{pmatrix} \cos^2(\theta') - \sin^2(\theta') & 2\cos(\theta')\sin(\theta') \\ 2\cos(\theta')\sin(\theta') & \sin^2(\theta') - \cos^2(\theta') \end{pmatrix} \tag{2.31}$$

As an exercise, we find that photonic qubit states in Eq. 2.22–2.24 can be generated from $|H\rangle$ with cascaded wave plates:

$$|k\rangle = HWP(\theta')QWP(\theta)|H\rangle. \tag{2.32}$$

Table 2.1: Wave plate angles to transform $|H\rangle$ to a specific output state.

Output $\|k\rangle$	θ'(HWP)	θ(QWP)
$\|H\rangle$	0	0
$\|V\rangle$	$\pi/4$	0
$\|D\rangle$	$\pi/8$	0
$\|A\rangle$	$-\pi/8$	0
$\|R\rangle$	$\pi/8$	$-\pi/4$
$\|L\rangle$	$-\pi/8$	$\pi/4$

Table 2.1 gives the set of angles of the QWP-HWP pair for given outputs.

Polarizing beam splitter (PBS) cubes are also important optical devices in this thesis. They are used for state preparation or projective measurements. They operate such that an input state of the form $\alpha|H\rangle + \beta|V\rangle$ is transmitted (reflected) through the PBS with probability $|\alpha|^2$ ($|\beta|^2$) with the output state corresponding to $|H\rangle$ ($|V\rangle$).

2.2.2 Bloch sphere

The Bloch sphere, illustrated in Fig. 2.3, is a visual representation of photonic qubits. This representation becomes natural when the general pure state is provided by

$$|\psi_i\rangle = \cos(\theta/2)|H\rangle + e^{i\phi}\sin(\theta/2)|V\rangle, \tag{2.33}$$

where $0 \leq \theta \leq \pi$ and $0 \leq \phi \leq 2\pi$. This parametrization respects the normalization constraint, $|\cos(\theta/2)|^2 + |e^{i\phi}\sin(\theta/2)|^2 = 1$. A general linear transformation of a state maps $(\theta, \phi) \mapsto (\theta - \alpha, \phi - \beta)$. Parameters θ and ϕ are spherical coordinates, and specify a point $\vec{s}(\sin\theta\cos\phi, \sin\theta\sin\phi, \cos\theta)$ on the unit sphere, along the respective axes $(\hat{x}, \hat{y}, \hat{z})$, and known as a Bloch vector. Note that our basis $|H\rangle/|V\rangle$ corresponds to the poles of the sphere. In fact, all orthogonal quantum states are antipodal in this representation. Pure qubit states lie on the periphery, while mixed states lie in the interior. The maximally mixed state, $\frac{1}{2}\mathcal{I}$ is found at the center of the sphere and corresponds to an evenly weighted linear combination of *any* two orthogonal pure states.

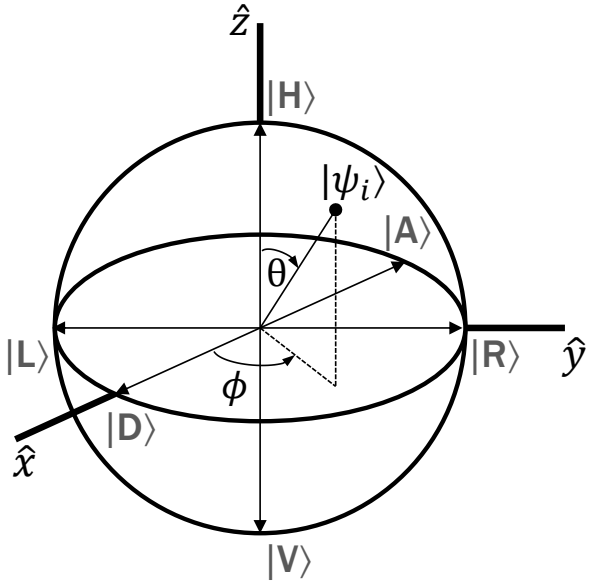

Figure 2.3: **Bloch sphere representation of photonic qubit states**. Any qubit state can be represented on a unit radius sphere, with major coordinate axes $\hat{x}$, $\hat{y}$ and $\hat{z}$. Pure states ($|\psi_i\rangle$) lie on the surface and mixed states in the interior. Orthogonal states are antipodal.

The density matrix of a qubit state can be represented generally as

$$\rho = \frac{1}{2}\left(\mathcal{I} + \sum_{\mu=1}^{3} s_\mu \sigma_\mu\right) \tag{2.34}$$

where $\{\sigma_1, \sigma_2, \sigma_3 : 1 = x, 2 = y, 3 = z\}$ are the Pauli operators and $\mathcal{I}$ is the identity matrix. $s_\mu (\mu = 1, 2, 3)$ is the component of the Bloch vector $\vec{s}$ and corresponds to the eigenvalue of Pauli operator σ_μ, for a given state ρ. For example, if $\rho = |\psi_i\rangle\langle\psi_i|$ with $|\psi_i\rangle$ given by Eq. 2.33, we find

$$s_x = \mathrm{tr}(\rho\sigma_x) = 2\cos(\theta/2)\sin(\theta/2)\cos\phi \tag{2.35}$$

$$s_y = \mathrm{tr}(\rho\sigma_y) = 2\cos(\theta/2)\sin(\theta/2)\sin\phi \tag{2.36}$$

$$s_z = \mathrm{tr}(\rho\sigma_z) = \cos^2(\theta/2) - \sin^2(\theta/2) \tag{2.37}$$

If the state is pure, $|\vec{s}|$=1, and if the state is mixed, $0 \leq |\vec{s}| < 1$.

2.3 On dispersion of wave packets

A pulse of light is a wave packet, a superposition of many monochromatic waves. While each wave travels at its own phase velocity, the peak of the packet travels with the group velocity. A dispersive medium is characterized by a wavelength-dependent refractive index $n = n(\lambda)$. The dependence of n on wavelength can be quantified with the Sellmeier equation, generally of the form

$$n^2 \cong 1 + \sum_i A_i \frac{\lambda^2}{\lambda^2 - B_i^2}. \tag{2.38}$$

Parameters A_i and B_i for common materials are usually provided in tables. Because the speed of light in the media is $c/n(\lambda)$, each frequency (wavelength) components of a short pulse of light experiences a different time delay, as illustrated in Fig. 2.4.

Figure 2.4: **A dispersive medium broadens a pulse of light**. When a pulse of light propagates through a dispersive medium, each frequency component travels at a different speed, causing the pulse to broaden in time. The shorter wavelengths (B) lag behind the longer wavelengths (R) in this example.

We model propagation through a transparent linear media in the frequency domain, because the pulse spectrum is left unchanged and only the phase factor is affected by the propagation. Let us define the pulse spectrum, with spectral amplitude $f(\nu)$ and centered at the average frequency ν_0

$$E(\nu) = f(\nu)e^{i\phi(\nu)}. \tag{2.39}$$

For propagation in the $+z$ direction, $\phi(\nu) = \beta(\nu)z$, where the wave number $\beta(\nu) = 2\pi n(\nu)\nu/c$. In terms of angular frequency ($\omega = 2\pi\nu = 2\pi c/\lambda$), $\beta(\omega) = n(\omega)\omega/c$. We may expand the phase function in Eq. 2.39 in a Taylor series centered at frequency ν_0. Retaining only the first three terms,

$$\beta(\nu)z \simeq \beta_0 + \beta_1(\nu - \nu_0) + \frac{1}{2!}\beta_2(\nu - \nu_0)^2, \tag{2.40}$$

where $\beta_0 = \phi(\nu_0)$, $\beta_1 = 2\pi z\frac{d\beta}{d\omega}|_{\omega_0}$ and $\beta_2 = (2\pi)^2 z\frac{d^2\beta}{d\omega^2}|_{\omega_0}$. In most practical cases of interest in this thesis, we can neglect the constant phase term β_0 and the second term β_1, for which $\beta_1 z$ represents the group delay that can be accounted for in a retarded frame of reference. The second derivative of $\beta(\omega)$, $\frac{d^2\beta(\omega)}{d\omega^2}$ is the group velocity dispersion (GVD) parameter and causes pulse distortion. For the materials considered here, this distortion is assumed to be well-behaved and the quadratic frequency dependence of the spectral phase will result in a chirp.

2.3.1 Single-mode optical fibers for positive dispersion

Distortion of wave packets in optical fibers is governed by several types of dispersion[2]. However, for wavelengths lower than 1.3 μm (in silica glass) material dispersion is the dominant source. If we consider short-length fiber and weak optical powers, we can neglect polarisation-mode dispersion and nonlinear effects, generally leading to additional pulse distortions. Here we look at how a single-mode fiber, made of fused-silica, introduces positive second order dispersion (chirp).

For fused-silica, the Sellmeier equation in Eq. 2.38 has parameters A_i and B_i given in Table 2.2. A pulse propagates through the fiber at the group velocity, given by $v_g = \left(\frac{d\beta(\omega)}{d\omega}\right)^{-1} = c/n_g$, with $n_g = \left(n(\lambda) - \lambda\frac{dn}{d\lambda}\right)$ the group index.

For a given fiber length, L, the second-order dispersion term β_2 in Eq. 2.40 is usually expressed in terms of wavelength

$$\beta_2 = (2\pi)^2\frac{d^2\beta(\omega)}{d\omega^2}L = \frac{2\pi\lambda}{c^2}\lambda^2\frac{d^2n}{d\lambda^2}L, \tag{2.41}$$

[2]See for example Ref. [1], Chapter 9.

Table 2.2: Sellmeier coefficient for fused-silica. From Table 5.5-1 in Ref. [1]

A1	0.696166	B1	0.068404
A2	0.407943	B2	0.116241
A3	0.897479	B3	9.896161

where we have used the chain rule $\frac{d^2}{d\omega^2} = \frac{\lambda^2}{(2\pi c)^2}\left(\lambda^2 \frac{d^2}{d\lambda^2} + 2\lambda \frac{d}{d\lambda}\right)$. β_2 is positive at wavelengths shorter than 1,276 nm and the medium is said to exhibit *normal dispersion*.

It is also common to define a dispersion coefficient D_λ,

$$D_\lambda = -\frac{\lambda}{c}\frac{d^2 n}{d\lambda^2}. \tag{2.42}$$

Using this coefficient, one has a good estimate of the temporal spread of the packet inside the fiber

$$\sigma_\tau = |D_\lambda| \sigma_\lambda L, \tag{2.43}$$

where σ_λ is the pulse spectral width and L the fiber length. For example, using coefficients in Table 2.2 for fused-silica, $D_\lambda = -101$ ps/(nm·km) at $\lambda = 811$ nm, and for a 4-nm spectral width and a 34-meter long fiber, the expected temporal spread is $\sigma_\tau \cong 13.75$ ps.

2.3.2 Diffraction gratings for negative dispersion

Diffraction gratings introduce angular dispersion to incident pulses [77], causing a group velocity dispersion similar to a transparent linear medium. Here we consider grating pairs [78] to introduce negative second order dispersion. The device is illustrated in Fig. 2.5, consisting of two parallel and identical diffraction gratings. The dispersion introduced by this pair of gratings is derived in section 2.5.6 of Ref [77].

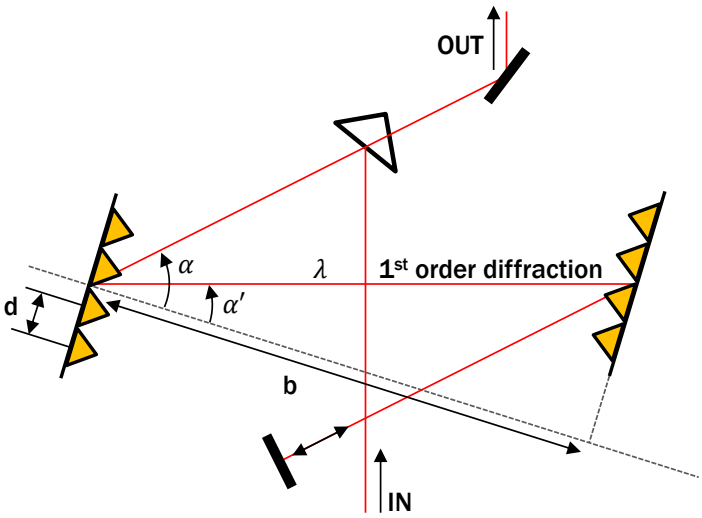

Figure 2.5: **Parallel gratings device for negative dispersion**. Two diffraction gratings with grating constant d have a normal separation b. Light coming in is reflected on a mirror prism and arrives on the first grating at angle α with the normal. First-order diffracted light makes an angle α' with the normal and reaches the second grating, bounces off a mirror slightly tilted such that the light diffracts on each grating once more, and leaves the setup on top of the prism. This arrangement does not introduce net angular dispersion.

The grating equation, for the first order diffraction in Fig. 2.5, is given by

$$\sin\alpha' = \frac{\lambda}{d} - \sin\alpha, \tag{2.44}$$

where d is the distance between the grooves, α is the angle of incidence on the first grating and α' is the diffraction angle of light at wavelength λ. Angles are measured relative to the normal, and here, the signs of α and α' are the same. The *littrow* angle is found at $\alpha' = \alpha$.

In terms of the central wavelength λ, the second-order dispersion applied by the pair of gratings is obtained [77] with

$$\beta_2 = (2\pi)^2 \frac{d^2\beta(\omega)}{d\omega^2} L = -(2\pi)^2 \frac{\lambda}{\pi c^2} \left(\frac{\lambda}{d}\right)^2 \frac{L}{\cos^2(\alpha')}. \tag{2.45}$$

In Eq. 2.45, the angle α' is found using the grating equation, and $L = b/\cos\alpha'$ is the distance between the gratings along the ray at λ. A pulse propagating twice between the gratings of Fig. 2.5 can therefore be considered as having traversed a linear medium of length L with a negative dispersion. The advantage of this device is that the dispersion can be tuned by changing the grating separation L.

2.4 Single-photon detection with silicon avalanche photodiodes

Single-photon detectors are very sensitive devices capable of registering energy of the order of 10^{-19} J in the visible. They play an important role in optical quantum information science, the major driver for their development. There are several emerging single-photon detector technologies [59], but most of them are currently at an early stage of development and require sophisticated cooling technology.

In this thesis we relied on more mature semiconductor-based detectors, such as the silicon single-photon avalanche photodiode (SAPD). This is an avalanche photodiode (APD) with a p-n or p-i-n junction [41] and biased such that the arrival of a single photon in the absorption region generates an avalanche gain in a multiplication region [41], creating a large current pulse that can be measured. The incident optical power converted to the output signal current is a function of the intrinsic response of the APD, the gain depending on the reverse voltage and the wavelength of incident radiation. The typical spectral range of SAPD is from 400 nm to 1060 nm, where the longer wavelength corresponds to the bandgap energy of the semiconductor ($\sim$ 1.12 eV).

Although those photon counting modules don't have the ability to resolve photon number, they are nevertheless widely used for quantum optics experiments. Their sensitivity over the visible spectral range has high efficiency, from 60-35% for 650-830 nm. They also have low dark counts ($\sim$500 counts/s), small jitter time ($\sim$400 ps), and low dead time of 50 ns and they are electronically cooled and temperature controlled in a single practical module.

Part I

Multi-photon entanglement

Chapter 3

Exploring genuine quantum nonlocality through Svetlichny's inequality

Most of the material in this Chapter is published[1] in the following:

Reference: J. Lavoie, R. Kaltenbaek and K. J. Resch, Experimental violation of Svetlichny's inequality, *New J. Phys.*, **11** 073051 (2009)

Contributions: K.J.R conceived the study and designed the experiment with R.K. I built the setup, performed the experiments and collected data. I analysed data with R.K. and wrote and edited the paper with my coauthors.

[1] No copyrights from the journal is required to include the article (all or part) in this thesis.

3.1 Introduction

Quantum mechanics cannot be described by local hidden-variable (LHV) theories. This is the conclusion of Bell's seminal work, in which he derived a strict limit to the strength of correlations achievable by all LHV models that is violated by quantum predictions [27]. Bell's original inequality did not allow for imperfections and thus it was not accessible to experimental tests. Clauser, Horne, Shimony and Holt (CHSH) addressed this issue and developed the CHSH inequality [28], which allowed for tests in actual experiments. Since then a growing number of experiments have been reported (for examples, see [79, 80, 81, 29, 82, 83, 84, 85, 30, 31, 33, 86, 87, 88, 32, 89]), and the overwhelming experimental evidence from these tests is in favour of quantum mechanics, ruling out LHV theories. It should be noted that, while no *loophole-free* Bell test has been performed, the most significant potential loopholes, relating to detection efficiency and space-like separation of the choices of measurements settings, have both separately been closed [29, 31, 33].

Both Bell's inequality and the CHSH inequality were formulated for testing the correlations between just two particles. For more than two particles, Greenberger, Horne and Zeilinger (GHZ) showed [90] that a contradiction between LHV theories and quantum mechanics can be seen directly in perfect correlations, as opposed to statistically in imperfect ones. Soon thereafter Bell-type inequalities for more than two particles were developed [34, 91, 92, 93, 94, 95, 96, 97, 98]. Quantum predictions can violate such inequalities by an amount increasing exponentially with the particle number [34, 91, 93, 94, 95, 97].

All of the aforementioned inequalities are based on the assumption that local realism applies to each individual particle. Two-particle inequalities have been developed which are in conflict with quantum mechanics although they allow restricted, but physically motivated, nonlocal correlations [99]. These inequalities have recently been violated experimentally [100].

Svetlichny showed that even if one allows unrestricted nonlocal correlations between any two of the constituent particles in a three-particle setting one can still find inequalities violated by quantum mechanical predictions [35]. The correlations allowed by Svetlichny's model are strong enough to maximally violate three-partite inequalities, such as Mermin's [101], which assume local realism for all particles involved. A violation of such inequalities

therefore can only rule out LHV theories, while a violation of Svetlichny's inequality directly rules out a whole class of nonlocal hidden-variable theories [102, 101, 103, 104, 105]. Svetlichny's work has since been generalized to the case of N particles [106, 107, 108].

Experimental tests have been performed confirming the violation of the Mermin inequality [109], the Mermin-Ardehali-Belinskii-Klyshko (MABK) inequality [110], and the cluster state inequality developed by Scarani et. al. [111]. For an even number of particles only, a sufficiently large violation of the MABK inequality also rules out partially nonlocal hidden-variable models [107]. The violation of the MABK inequality in [110] thus confirmed genuine four-particle entanglement and non-locality. The original Svetlichny inequality, however, remains untested.

In this chapter, we begin with a brief theoretical description of Svetlichny's inequality. We then describe how we experimentally produced high-fidelity three-photon GHZ states and characterized them via quantum state tomography (QST) [112]. Using these states, modulo standard loopholes [29, 31, 33], we demonstrate a convincing violation of Svetlichny's inequality.

3.2 Theory

The two assumptions resulting in Bell-type inequalities are locality and realism as they were introduced by Einstein, Podolsky and Rosen [24]. We first review a straightforward method to derive the CHSH inequality from these two assumptions following an argument described by Peres [113].

Pairs of particles are distributed to two distant parties, A and B as shown in Fig. 3.1. Party A (B) can choose between two measurement settings $\mathbf{a}$ and $\mathbf{a}'$ ($\mathbf{b}$ and $\mathbf{b}'$). For each measurement setting, two outcomes, $+1$ or -1, are possible. Realism assumes that the measurement outcomes are predetermined by some properties of the system investigated. These properties are known as hidden variables because they are not necessarily accessible to observation. The additional assumption of locality requires that the measurement outcomes on side A are independent of the measurement setting on side B, and vice versa.

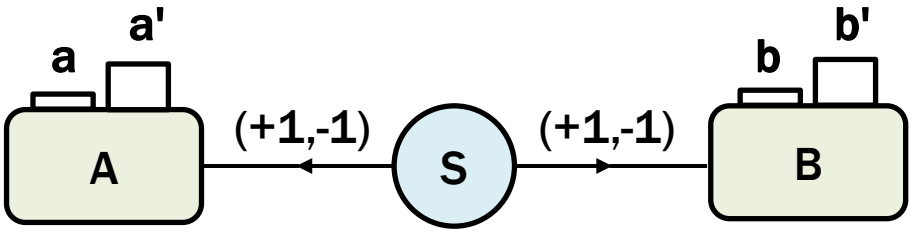

Figure 3.1: **Schematic illustration of a Bell experiment**. The source S emits two particles towards station A and B. Measurements parallel to $\mathbf{a}$ and $\mathbf{a}'$, ($\mathbf{b}$ and $\mathbf{b}'$) reveals the state of the particles, ± 1.

Thus for any given pair of particles the measurement outcomes have predetermined values $a = \pm 1$ and $a' = \pm 1$ on side A and $b = \pm 1$ and $b' = \pm 1$ on side B.

We can form the expressions

$$\begin{aligned} S_2 &\equiv ab + ab' + a'b - a'b' \\ S_2' &\equiv a'b' + a'b + ab' - ab. \end{aligned} \tag{3.1}$$

These expressions identically satisfy the relations:

$$\begin{aligned} S_2 &\equiv a(b + b') + a'(b - b') = \pm 2 \\ S_2' &\equiv a'(b' + b) + a(b' - b) = \pm 2 \end{aligned} \tag{3.2}$$

where this last form allows us to verify the equality; since b and b' must have either the same sign or opposite sign, only one term in each equation is non-vanishing and has a value ± 2. If, for example, S_2 is averaged over many trials, the absolute value must be smaller or equal to 2, which results in the CHSH inequality [28]:

$$|E(\mathbf{a}, \mathbf{b}) + E(\mathbf{a}, \mathbf{b}') + E(\mathbf{a}', \mathbf{b}) - E(\mathbf{a}', \mathbf{b}')| \leq 2, \tag{3.3}$$

where the correlation, $E(\mathbf{a}, \mathbf{b})$, is the ensemble average $\langle ab \rangle$ over the product of measurement outcomes a and b for measurement settings $\mathbf{a}$ and $\mathbf{b}$, respectively.

This argument can be extended to three particles [107]. We will denote the particles as well as the measurement outcomes as a, b and c, the measurement settings as $\mathbf{a}$, $\mathbf{b}$, $\mathbf{c}$. The outcome of each measurement can be $+1$ or -1. If we assume local realism for each of the three particles, then for a given set of three particles the measurement outcomes a, b and c as well as their primed counterparts will have predetermined values ± 1. Using (3.2) we find that the following identity must hold:

$$S_3 \equiv S_2(c+c') + S_2'(c-c') = 2\,(a'bc + ab'c + abc' - a'b'c') = \pm 4. \tag{3.4}$$

Dividing this expression by two, and averaging over many trials yields Mermin's inequality [34] for three particles:

$$|E(\mathbf{a}', \mathbf{b}, \mathbf{c}) + E(\mathbf{a}, \mathbf{b}', \mathbf{c}) + E(\mathbf{a}, \mathbf{b}, \mathbf{c}') - E(\mathbf{a}', \mathbf{b}', \mathbf{c}')| \leq 2, \tag{3.5}$$

where $E(\mathbf{a}, \mathbf{b}, \mathbf{c}) = \langle abc \rangle$.

Now assume that we allow arbitrary (nonlocal) correlations between just *two* of the particles, say a and b, while we still assume local realism with respect to the third particle, c. In this case we cannot factorize S_2 as we did in (3.2) because outcomes for particle a might nonlocally depend on the outcomes and/or measurement settings for particle b. However, we can still write

$$\begin{aligned} \tilde{S}_2 &= (ab) + (ab') + (a'b) - (a'b') \\ \tilde{S}_2' &= (a'b') + (a'b) + (ab') - (ab), \end{aligned} \tag{3.6}$$

where the parentheses are meant as a reminder that these quantities should be regarded as separate and independent quantities. Each of these quantities as well as c and c' must take predetermined values ± 1 because we assume local realism with respect to the third particle. This model is strong enough to violate, and reach the algebraic maximum of Mermin's inequality (since $\tilde{S}_2$ can be ± 4). Thus no experimental violation of Mermin's inequality can rule out this restricted nonlocal hidden-variable model.

With this in mind let us slightly modify our argument to derive Svetlichny's inequality. Because $\tilde{S}_2$ and $\tilde{S}_2'$ are functions of the same four quantities, they are not independent. For example, whenever one of the two quantities reaches its algebraic maximum ± 4, the other one will be 0. As a result the following identity holds:

$$\begin{aligned}\tilde{S}_2 c - \tilde{S}_2' c' &= (ab)\,c + (ab)\,c' + (ab')\,c - (ab')\,c' + (a'b)\,c - (a'b)\,c' - (a'b')\,c - (a'b')\,c' \\ &= \pm 4, \pm 2, 0. \end{aligned} \tag{3.7}$$

Averaging over many trials yields the Svetlichny inequality:

$$\begin{aligned}\mathcal{S}_v \equiv\ & |E(\mathbf{a},\mathbf{b},\mathbf{c}) + E(\mathbf{a},\mathbf{b},\mathbf{c}') + E(\mathbf{a},\mathbf{b}',\mathbf{c}) - E(\mathbf{a},\mathbf{b}',\mathbf{c}') + \\ & E(\mathbf{a}',\mathbf{b},\mathbf{c}) - E(\mathbf{a}',\mathbf{b},\mathbf{c}') - E(\mathbf{a}',\mathbf{b}',\mathbf{c}) - E(\mathbf{a}',\mathbf{b}',\mathbf{c}')| \leq 4, \end{aligned} \tag{3.8}$$

where we refer to $\mathcal{S}_v$ as the Svetlichny parameter. It is remarkable that, although we started out by allowing nonlocal correlations between particles a and b while c is local, one gets an expression identical to (3.8) if b and c are nonlocally correlated while a is local, or if a and c are nonlocally correlated while b is local. Every hidden-variable model that allows for nonlocal correlations between any two particles but not between all three can be seen as a probabilistic combination of models where the partition of the particles between nonlocal and local is made one or the other way. All of these models fulfill the Svetlichny inequality [103].

It was shown by Svetlichny that his inequality can be violated by quantum predictions, and that the maximum violation can be achieved with GHZ states. Assume we have a polarisation-entangled GHZ state $|\psi\rangle = \frac{1}{\sqrt{2}}(|HHV\rangle + |VVH\rangle)$, and let our measurement settings all be in the xy-plane of the Bloch sphere, i.e. we can write the corresponding states we project on as $\frac{1}{\sqrt{2}}\left(|H\rangle + \mathrm{e}^{\mathrm{i}\phi}|V\rangle\right)$. For example, the measurement settings $\mathbf{a}$ and $\mathbf{a}'$ for particle a correspond to projective measurements on the states $|A(\pm)\rangle = \frac{1}{\sqrt{2}}\left(|H\rangle \pm \mathrm{e}^{\mathrm{i}\phi_a}|V\rangle\right)$ and $|A'(\pm)\rangle = \frac{1}{\sqrt{2}}\left(|H\rangle \pm \mathrm{e}^{\mathrm{i}\phi_a'}|V\rangle\right)$, respectively. Here, the $\pm$ corresponds to the state the particle is projected on if the outcome of the measurement is ± 1. For particles b and c we choose an analogous notation. Then the quantum prediction for the left-hand side of (3.8) is

$$\begin{aligned}&|\cos(\phi_a + \phi_b - \phi_c) + \cos(\phi_a + \phi_b - \phi_c') + \cos(\phi_a + \phi_b' - \phi_c) - \\ &\cos(\phi_a + \phi_b' - \phi_c') + \cos(\phi_a' + \phi_b - \phi_c) - \cos(\phi_a' + \phi_b - \phi_c') - \\ &\cos(\phi_a' + \phi_b' - \phi_c) - \cos(\phi_a' + \phi_b' - \phi_c')|\,. \end{aligned} \tag{3.9}$$

With a suitable choice of angles, such as:

$$\phi_a = \frac{3\pi}{4}, \phi'_a = \frac{\pi}{4}, \phi_b = \frac{\pi}{2}, \phi'_b = 0, \phi_c = 0, \phi'_c = \frac{\pi}{2}, \tag{3.10}$$

this results in $\mathcal{S}_v = 4\sqrt{2} > 4$, which is the maximum violation of Svetlichny's inequality achievable with quantum mechanics [103].

Since any hidden-variable model describing a three-particle state where only two particles are nonlocally correlated has to fulfill the Svetlichny inequality, its violation explicitly rules out this type of nonlocal hidden-variable theory.

3.3 Experiment

Our experiment uses a pulsed Ti:Sapphire laser (repetition rate 80 MHz, 2.5 W avg. power, 790 nm center wavelength, 9 nm FWHM bandwidth). We frequency double the near-infrared beam, producing 700 mW average power near 395 nm with a FWHM bandwidth of 1.8 nm. This upconverted beam is focused on a pair of orthogonally-oriented β-Barium-Borate (BBO) nonlinear crystals [114] cut for type-I noncollinear degenerate spontaneous parametric down-conversion (SPDC) with an external half opening angle of 3°. The pump polarisation is set to diagonal, $|D\rangle = \frac{1}{\sqrt{2}}(|H\rangle + |V\rangle)$, such that each pump photon can produce a photon pair either in the first or the second BBO crystal. To compensate for temporal distinguishablity between the pairs created in the first and the second crystal the pump passes through a 1mm α-BBO crystal, a 2mm quartz crystal, and a 0.5mm quartz crystal, all cut for maximum birefringence. To compensate the 75 μm spatial walk-off between the horizontally and vertically polarized SPDC photons observed in one of the output modes, we insert a 0.75 mm thick Bismuth-Borate (BiBO) crystal cut at $\theta = 152.6°$ and $\phi = 0°$. For these cut angles the crystal compensates the transverse walk-off without introducing additional time walk-off. The photons are subsequently coupled into single-mode fibres. We label the two corresponding spatial output modes as 1 and 2, see Fig. 3.2a. Fiber polarisation controllers ensure that in mode 1 states in the H/V basis remain unchanged while in mode 2 we flip the polarisation, i.e., $|H\rangle \leftrightarrow |V\rangle$. With this configuration we achieve a two-photon coincidence rate of 43 kHz and single rates of about 240 kHz and

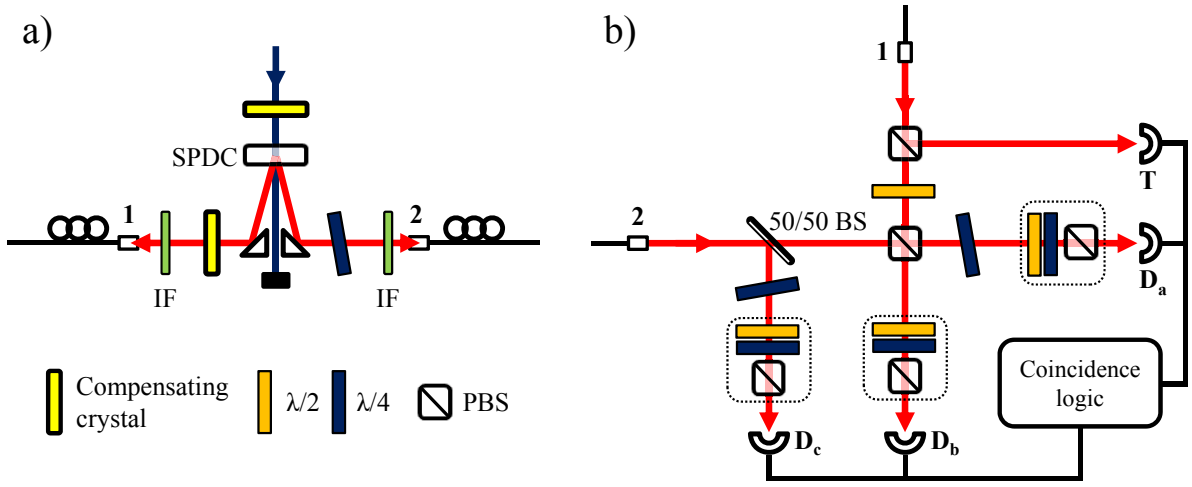

Figure 3.2: **Experimental setup**. **a**, Schematic of our type-I SPDC source. A 45° polarized, pulsed UV beam pumps a pair of orthogonally oriented BBO crystals cut for type-I phase matching. Temporal walk-off between the pairs created in the first and in the second crystal is compensated by α-BBO and quartz crystals before the SPDC crystals. Spatial walk-off, which occurred in mode 1, was compensated by a BiBO crystal. The phase between horizontal and vertical photons was adjusted by tilting a $\lambda/4$ plate in mode 2. All photons pass through 3 nm FWHM bandwidth filters around 790 nm and are coupled into single-mode fibres corresponding to the spatial modes 1 and 2. **b**, The interferometer used to project on a three-photon GHZ state. Using fibre polarisation controllers, the polarisation in mode 2 is rotated such that we map $|H\rangle \rightarrow |V\rangle$ and $|V\rangle \rightarrow |H\rangle$, while in mode 1, H and V are preserved. Inside the interferometer the four photons from a double-pair emission can be split up into four separate spatial modes and result in a four-fold coincidence event between the detectors T, D_a, D_b, and D_c. In this case the three photons in the modes a, b, and c will be projected on the three-photon GHZ state $\frac{1}{\sqrt{2}}\left(|H_a H_b V_c\rangle + |V_a V_b H_c\rangle\right)$ given that the photons detected by D_a and D_b are indistinguishable.

270 kHz for modes 1 and 2, respectively. The measured contrast of the pairs is 75 : 1 in the H/V basis and 61 : 1 in the D/A basis when the source is adjusted to produce $|\phi^+\rangle = \frac{1}{\sqrt{2}}(|HH\rangle + |VV\rangle)$ states.

Following the approach in [115] we use the double-pair emission of the SPDC source to produce 3-photon GHZ correlations in the interferometer shown in Fig. 3.2b. A four-fold coincidence detection in the four outputs of the interferometer indicates the successful generation of the GHZ state. To lowest significant order, a four-fold coincidence can only occur if two photons enter the interferometer via the spatial mode 1, and their two partner photons enter it via mode 2. The two photons in input mode 1 impinge on a polarizing beam splitter (PBS). In order for a four-fold coincidence event to occur one of them must be $|H\rangle$ and the other $|V\rangle$. The $|V\rangle$-photon is reflected at the PBS. Its detection by detector T serves as a trigger event. The $|H\rangle$-photon passes through the PBS in mode 1, and a $\lambda/2$ plate oriented at 22° rotates the polarisation from $|H\rangle$ to $|D\rangle$. The two photons in mode 2 are split at the beam splitter (BS) with probability 1/2. Only in this case a four-fold coincidence can occur. The transmitted photon and the $|D\rangle$ polarized photon in mode 1 are overlapped on a PBS. A coincidence detection event in the two output modes of the PBS can only occur if both photons are transmitted or both are reflected. If these two possibilities are indistinguishable, Hong-Ou-Mandel (HOM) interference will occur [116]. In the reflected mode of the BS we compensate for a phase shift due to birefringence in the BS by tilting a $\lambda/4$ plate.

A four-fold coincidence detection in the interferometer outputs can only occur if the trigger photon is $|V\rangle$, and if the other three photons in the modes a, b and c (see Fig. 3.2b are either $|H_aH_bV_c\rangle$ or $|V_aV_bH_c\rangle$. By tilting a $\lambda/4$ plate in output mode a we adjust the relative phase between these contributions such that a four-fold coincidence event signals a GHZ state of the form $\frac{1}{\sqrt{2}}(|H_aH_bV_c\rangle + |V_aV_bH_c\rangle)$.

Given this state, quantum mechanics predicts a maximum violation of Svetlichny's inequality if we choose measurements of the form $|H\rangle + e^{i\phi}|V\rangle$ with the angles given in (3.10). Particles a, b and c are identified with photons in the interferometer output modes a, b and c, respectively. To test Svetlichny's inequality each of the photons has to be measured in two measurement bases, and for each basis there are two possible outcomes, $+1$ and -1. For each outcome we have to set the polarisation analyzer in the respective

mode such that a photon detected after passing through the analyzer corresponds to that outcome.

The Svetlichny parameter, $\mathcal{S}_v$, of Eq. 3.8 consists of 8 correlations, each of which can be constructed from 8 three-photon polarisation measurements[2] for a total of 64 measurements. Each polarisation analyzer consists of a $\lambda/2$-plate followed by a $\lambda/4$-plate and then a PBS. The photons passing the PBSs are detected with single-mode fibre-coupled single-photon counting modules; the coincidence window is 10 ns.

We fully characterize the state produced by our setup with QST. Because all the measurement settings for the Svetlichny inequality lie in the xy-plane of the Bloch sphere these alone are not tomographically complete. Instead of performing an additional run apart from the measurements of the Svetlichny settings, we add two additional projective measurements ($|H\rangle$ and $|V\rangle$) for each of the particles, resulting in a total of 216 three-photon polarisation measurements. Our set of measurements is now actually tomographically overcomplete, which has been shown to produce better estimates of quantum states [117].

3.4 Results

In our setup the maximum four-fold coincidence rates of 7×10^{-2} Hz and 8×10^{-2} Hz were achieved for the correlations $|H_a H_b V_c\rangle$ and $|V_a V_b H_c\rangle$, respectively. To get statistically significant counts we integrated over 27 min per measurement. In order to reduce the negative effects of misalignment of the setup over time we realized this integration by counting for 60 s for each of the 216 measurements, then repeating the full cycle of measurements 27 times. The resulting counts are given in table 3.1.

We applied the maximum likelihood technique [118] to reconstruct the density matrix of our state. Its real and the imaginary part are shown in Fig. 3.3. The fidelity $F = \langle\psi|\rho|\psi\rangle$ of the density matrix with the GHZ state $\frac{1}{\sqrt{2}}(|HHV\rangle + |VVH\rangle)$ is 0.84 ± 0.01. The errors of quantities derived from the reconstructed density matrix were calculated via a Monte

[2] E.g., $E(\mathbf{a},\mathbf{b},\mathbf{c}) = \frac{(N_{+++}+N_{+--}+N_{-+-}+N_{--+})-(N_{---}+N_{-++}+N_{+-+}+N_{++-})}{\sum N}$, where N_{ijk} is the number of counts for settings $\mathbf{a}$, $\mathbf{b}$ and $\mathbf{c}$ with outcomes i,j and k, respectively. $\sum N$ is the sum of all counts in the numerator.

Settings for		Settings for a					
b	c	$\|A(+)\rangle$	$\|A(-)\rangle$	$\|A'(+)\rangle$	$\|A'(-)\rangle$	$\|H\rangle$	$\|V\rangle$
$\|B(+)\rangle$	$\|C(+)\rangle$	**12**	**56**	**20**	**69**	53	35
	$\|C(-)\rangle$	**52**	**19**	**47**	**18**	38	32
	$\|C'(+)\rangle$	**12**	**50**	**43**	**13**	31	35
	$\|C'(-)\rangle$	**48**	**16**	**14**	**56**	31	23
	$\|H\rangle$	34	39	32	44	4	71
	$\|V\rangle$	35	26	30	29	62	8
$\|B(-)\rangle$	$\|C(+)\rangle$	**70**	**16**	**76**	**12**	36	35
	$\|C(-)\rangle$	**12**	**53**	**12**	**46**	39	33
	$\|C'(+)\rangle$	**49**	**8**	**17**	**59**	37	44
	$\|C'(-)\rangle$	**22**	**40**	**75**	**19**	39	30
	$\|H\rangle$	47	37	28	33	4	75
	$\|V\rangle$	32	24	47	34	54	4
$\|B'(+)\rangle$	$\|C(+)\rangle$	**19**	**69**	**57**	**16**	40	31
	$\|C(-)\rangle$	**51**	**17**	**6**	**63**	25	40
	$\|C'(+)\rangle$	**48**	**13**	**47**	**12**	26	37
	$\|C'(-)\rangle$	**15**	**62**	**18**	**56**	34	28
	$\|H\rangle$	32	38	34	39	4	68
	$\|V\rangle$	44	34	36	40	53	4
$\|B'(-)\rangle$	$\|C(+)\rangle$	**68**	**18**	**17**	**62**	34	36
	$\|C(-)\rangle$	**19**	**54**	**45**	**11**	33	29
	$\|C'(+)\rangle$	**18**	**48**	**17**	**54**	42	33
	$\|C'(-)\rangle$	**55**	**13**	**62**	**29**	32	31
	$\|H\rangle$	26	25	39	42	1	51
	$\|V\rangle$	47	35	44	29	63	10
$\|H\rangle$	$\|C(+)\rangle$	42	40	39	52	77	6
	$\|C(-)\rangle$	31	22	31	32	52	4
	$\|C'(+)\rangle$	40	37	38	35	53	1
	$\|C'(-)\rangle$	41	30	36	38	65	5
	$\|H\rangle$	2	3	5	5	8	5
	$\|V\rangle$	79	66	72	67	119	5
$\|V\rangle$	$\|C(+)\rangle$	39	46	32	43	3	72
	$\|C(-)\rangle$	35	36	29	39	2	44
	$\|C'(+)\rangle$	25	42	33	43	7	59
	$\|C'(-)\rangle$	32	43	30	31	6	62
	$\|H\rangle$	62	68	54	69	3	131
	$\|V\rangle$	4	7	3	6	3	1

Table 3.1: **Experimentally-measured counts**. Four-fold coincidences for the 216 measurements performed for QST. A subset of 64 measured counts were used to test Svetlichny's inequality; these counts are shown in boldface type. We cycled through all of the measurements 27 times, counting for 60 s for each measurement. The four-fold coincidences given are the result of integrating over all of these cycles.

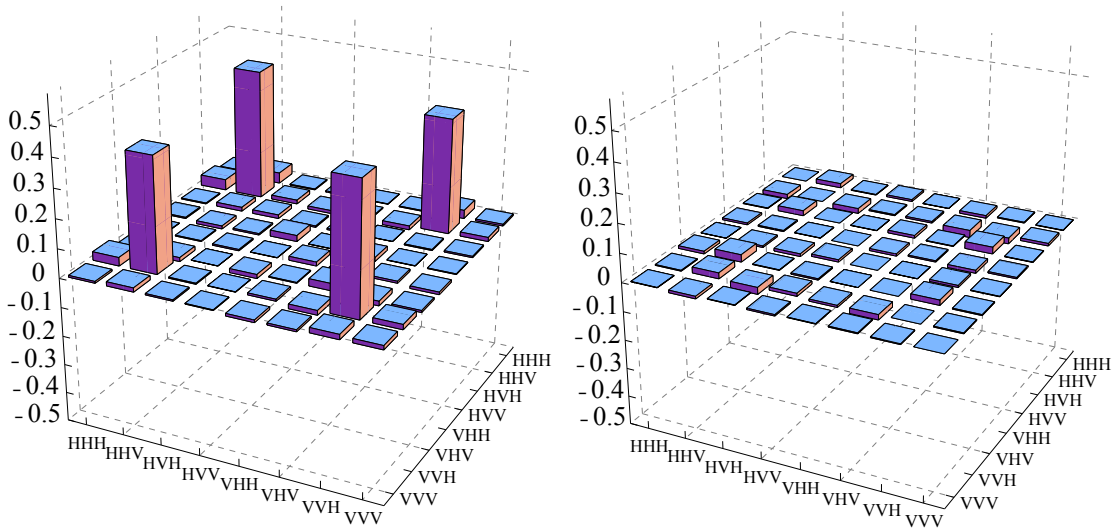

Figure 3.3: **Reconstructed three-photon density matrix**. Real part (left) and imaginary part (right) of the density matrix. The state was reconstructed from a tomographically overcomplete set of 216 measurements. For each measurement the four-fold coincidence counts were integrated over 27 min, see table 3.1. The fidelity of the reconstructed density matrix with the GHZ state $\frac{1}{\sqrt{2}}(|HHV\rangle + |VVH\rangle)$ is $(84 \pm 1)\%$.

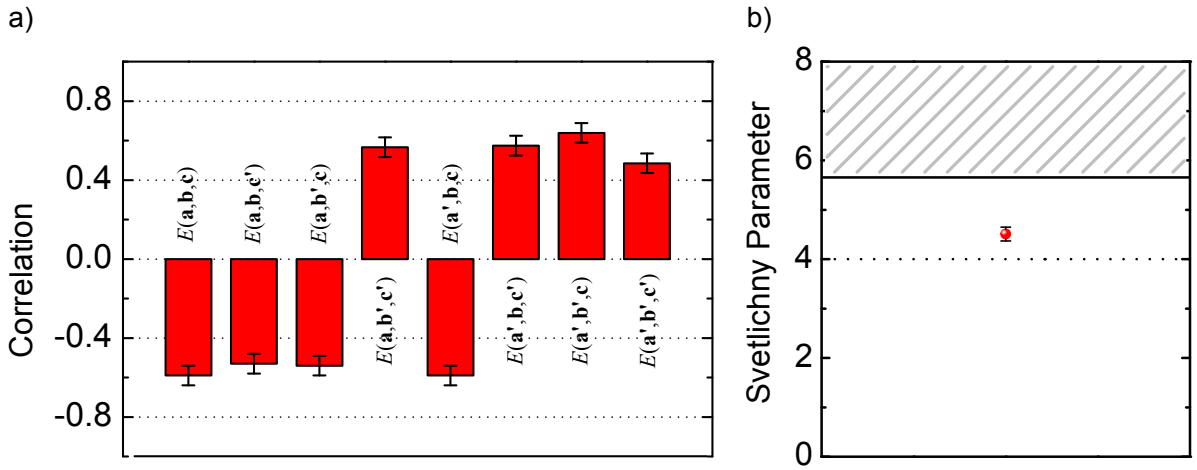

Figure 3.4: **Measured correlations and Svetlichny parameter**. **a**, Measured correlations for the eight combinations of measurement settings for the three particles. Each correlation is constructed from 8 four-fold coincidence measurements. The count rates for each of these measurements are given in table 3.1. **b**, These correlations yield a Svetlichny parameter of 4.51±0.14, which clearly violates the bound (dashed line) of 4 of the Svetlichny inequality. The quantum mechanical limit is $4\sqrt{2}$. Even higher values (pattern-filled region) can be reached by allowing arbitrarily strong nonlocal correlations.

Carlo simulation, where we used each of the measured counts as the mean of a Poissonian distribution. According to these distributions we generated random counts and ran the maximum likelihood algorithm. This procedure was repeated 400 times, and we report the standard deviation and mean for quantities derived from these reconstructed states.

The 64 measurements that quantum mechanics predicts to violate Svetlichny inequality are among the 216 measured. After integrating over all cycles we get a Svetlichny parameter of $\mathcal{S}_v = 4.51 \pm 0.14$; the eight measured correlations are shown in Fig. 3.4. This value violates the Svetlichny inequality by 3.6 standard deviations. It is in good agreement with the value, $\mathcal{S}_v^{QM} = 4.48 \pm 0.11$, predicted by quantum mechanics given the reconstructed density matrix.

3.5 Conclusion

We used the double-pair emission from a pulsed type-I SPDC source and projected the photons onto a GHZ state using a linear optical interferometer. We fully characterized the generated state and reconstructed the density matrix applying the maximum likelihood technique [118] using an overcomplete set of measurements. From the reconstructed density matrix, we found that our state matched the target GHZ state with a fidelity of $(84 \pm 1)\%$.

We experimentally demonstrated the violation of the original Svetlichny inequality for a three-particle GHZ state with a value of 4.51 ± 0.14, which is greater than 4 by 3.6 standard deviations. This value is in good agreement with that predicted by quantum mechanics from our reconstructed density matrix, 4.48 ± 0.11. By violating Svetlichny's long-standing inequality, we have shown that the correlations exhibited by three particles cannot be described by hidden-variable theories with at most two-particle nonlocality.

Important extensions could include space-like separation between detectors with randomly switched measurements, comparable to what was done by Weihs *et al.* [31]. Studying quantum correlations over large distance could also incorporate device-independent cryptography [36], a practical application of quantum nonlocality.

Chapter 4

Experimental bound entanglement

Most of the material in this Chapter is published[1] in the following:

Reference: J. Lavoie, R. Kaltenbaek, M. Piani, and K. J. Resch, Experimental Bound Entanglement in a Four-Photon State, *Phys. Rev. Lett.* **105**, 130501 (2010). "Copyright (2010) by the American Physical Society."

Contributions: M. P. proposed the experiment and provided theoretical support. R. K., K. J. R and I designed the experiment. I built the setup and collected data. R. K. and I analysed the final data. I wrote the first draft of the manuscript with M. P. All authors discussed the results and commented on the manuscript at all stages.

[1] No copyrights from the journal is required to include the article (all or part) in this thesis.

4.1 Introduction

Entanglement [119, 120] enables powerful new quantum technologies [121, 20, 18, 21, 122, 2], but in real-world implementations, entangled states are subject to decoherence and preparation errors. Entanglement distillation [123, 124] can often counteract these effects by converting imperfectly entangled states into a smaller number of maximally entangled states. States that are entangled but cannot be distilled are called *bound entangled* [125]. Any experimental realization of bound entangled states requires a convincing demonstration of their defining properties: entanglement and undistillability.

Bound entangled states are important for several reasons. First, they represent irreversibility in entanglement manipulation: they require the consumption of pure entanglement to be created via local operations and classical communication (LOCC), but no pure entanglement can be distilled from them via LOCC [125, 126, 127, 128]. Second, they constitute a challenge to develop better entanglement criteria, as there is no standard efficient way to detect their entanglement [129, 120]. Third, they are central to recent breakthroughs regarding quantum channel capacities [130]. Fourth, despite not being distillable, they still constitute a resource for quantum teleportation [131], quantum cryptography [132, 133], and channel discrimination [134]. Thus, bound entanglement is crucial for developing a more complete picture of the role of entanglement in quantum information.

A recent work reported the production of a pseudo-bound entangled state in liquid-state NMR [135]. They demonstrate sufficient control over their system to implement the transformations that lead to bound entanglement. Yet, they would need to start in a highly pure, rather than a highly mixed state, to generate bound, as opposed to pseudo-bound, entanglement. Optical systems on the other hand can produce highly pure states. In Ref [136], the authors claimed an optical demonstration of a Smolin bound-entangled state. Their data showed that their state was entangled. They reconstructed their state using quantum state tomography and applied the PPT test for distillability and argued that the eigenvalues are all positive or consistent with zero. However, their results show *five* negative eigenvalues over all three partial transpositions with a minimum of -0.02 ± 0.02 (see also the note added in [135]). Since the central point in the PPT test is that the minimum eigenvalue has to be *non-negative*, their claim of demonstrating bound

entanglement is not supported by their data.

In this chapter, we consider a family of four-qubit Smolin states [137], focusing on a regime where the bound entanglement is experimentally robust. We encode the state into the polarisation of four photons and show that our state exhibits both entanglement and undistillability. Then we demonstrate a key feature of Smolin states: the entanglement in our state, although bound, can be unlocked.

4.2 Theory

One of the most elegant and striking examples of bound entanglement is the four-party Smolin state [137],

$$\rho_S = \frac{1}{4}\sum_{\mu=0}^{3} |\Psi^\mu\rangle\langle\Psi^\mu|_{AB} \otimes |\Psi^\mu\rangle\langle\Psi^\mu|_{CD}, \tag{4.1}$$

where the subscripts label the parties, and $|\Psi^\mu\rangle$ are the two-qubit Bell states. One may understand the Smolin state in the following way: A and B share one of four possible Bell states, and C and D share the same state, but each Bell state is equally likely and unknown. The Smolin state is entangled in the sense that it does not admit a fully-separable decomposition of the form $\sum_k p_k \rho_A^k \otimes \eta_B^k \otimes \tau_C^k \otimes \xi_D^k$, with p_k probabilities and $\rho^k, \eta^k, \tau^k, \xi^k$ states. But it is evident from Eq. (4.1) that the Smolin state is separable (or unentangled) in the $(AB) : (CD)$ bipartite cut since it can be written in a biseparable form $\rho = \sum_k p_k \rho_{AB}^k \otimes \tau_{CD}^k$. Because the state is symmetric with respect to the exchange of any two parties [137, 138], it is separable with respect to all three two-two bipartite cuts $(AB) : (CD)$, $(AC) : (BD)$, and $(AD) : (BC)$. Following the arguments in [137], one concludes that no entanglement can be distilled between any two parties, and this excludes also the distillation of three- and four-partite entanglement. Thus, the Smolin state is, by definition, bound entangled. To prove that an experimentally prepared Smolin state is undistillable, it is sufficient to show that all eigenvalues remain positive under partial transposition (PPT) across all two-two bipartite cuts [125].

In any attempt to generate perfect Smolin states, the PPT property will be very sensitive to imperfections in the state preparation and counting statistics in the experimental

data. The main reason is that the partial transpose of the density matrix of a perfect Smolin state is not full-rank. Introducing a source of white noise leads to a full-rank matrix, whose PPT property is more robust and thus better suited for experimental demonstration. By varying the proportion of white noise one generates the family of noisy Smolin states

$$\rho_S(p) = (1-p)\rho_S + p\frac{\mathcal{I}}{16}, \tag{4.2}$$

where $0 \leq p \leq 1$ parameterizes the amount of noise, and $\mathcal{I}$ is the identity matrix. These states are bound entangled for $0 \leq p < 2/3$, and fully separable for $2/3 \leq p \leq 1$ [138]. Entanglement can be ascertained by the use of an entanglement witness, an observable $\mathcal{W}$ such that $\mathrm{tr}(\mathcal{W}\tau) < 0$ for some entangled state τ, while $\mathrm{tr}(\mathcal{W}\rho) \geq 0$ for all separable states ρ. A suitable witness for these states is $\mathcal{W} = \mathcal{I} - \sum_{i=1}^{3} \sigma_i^{\otimes 4}$ like in [136], where σ_1, σ_2 and σ_3 are the three Pauli matrices X, Y, Z.

4.2.1 An entanglement witness for the Smolin state

We consider an entanglement witness $\mathcal{W}$ such that a negative expectation value $\langle \mathcal{W} \rangle = \mathrm{tr}(\rho\mathcal{W}) < 0$ is sufficient to exclude that the prepared state ρ is in the set $\mathcal{S}$ of mixed states that are a convex combination of pure states with one party disentangled from the others, e.g. $|\alpha\rangle_A \otimes |\phi\rangle_{BCD}$. In such a convex combination, the disentangled party may differ from pure state to pure state. Of course, $\mathcal{S}$ is a superset of the set of completely separable states.

The witness reads $\mathcal{W} = \mathcal{I} - \sum_{i=1}^{3} \sigma_i^{\otimes 4}$. There are a number of ways to single out $\mathcal{W}$ as an appropriate witness; e.g., in [136] the derivation was based on the stabilizer formalism [139] and numerical optimization. Here we present a derivation that is completely analytical and uses the geometric approach of [140].

It will be sufficient to prove that the state $\rho_S(2/3)$, which is fully separable [138], is the closest to ρ_S in the set $\mathcal{S}$. Here, closeness is defined with respect to the Hilbert-Schmidt norm $\|X\|_{\mathrm{HS}} = \sqrt{\mathrm{tr}(X^\dagger X)}$. To this aim, using Proposition 5.1 in [140], one derives that it

is sufficient to check that $\max_{\tau\in\mathcal{S}} \mathrm{tr}(\rho_S\tau) \leq 1/8$. We have

$$\begin{aligned}
\max_{\tau\in\mathcal{S}} \mathrm{tr}(\rho_S\tau) &= \max_{|\alpha\rangle_A|\phi\rangle_{BCD}} \mathrm{tr}(\rho_S|\alpha\rangle\langle\alpha|_A \otimes |\phi\rangle\langle\phi|_{BCD}) \\
&= \max_{|\alpha\rangle_A|\phi\rangle_{BCD}} \mathrm{tr}(\rho_S^{\Gamma_A}(|\alpha\rangle\langle\alpha|)_A^T \otimes |\phi\rangle\langle\phi|_{BCD}) \\
&= \frac{1}{8}\left[1 - 4\min_{|\alpha\rangle_A|\phi\rangle_{BCD}} \mathrm{tr}(\rho_S|\alpha\rangle\langle\alpha|_A \otimes |\phi\rangle\langle\phi|_{BCD})\right] \\
&= \frac{1}{8}, \qquad (4.3)
\end{aligned}$$

where $\rho_S^{\Gamma_A}$ denotes the partial transpose of ρ_S with respect to A. The first equality comes from the symmetry of ρ_S and the convexity of $\mathcal{S}$, so that it is sufficient to consider pure states $|\alpha\rangle_A|\phi\rangle_{BCD}$ in the maximization; the second equality from the identity $\mathrm{tr}(XY) = \mathrm{tr}(X^{\Gamma_A}Y^{\Gamma_A})$; the third equality from $\rho^{\Gamma_A} = \frac{1}{8}(\sigma_2 \otimes \sigma_0^{\otimes 3})\frac{1}{8}(\mathcal{I} - 4\rho_S)(\sigma_2 \otimes \sigma_0^{\otimes 3})$ and the fact that $\sigma_2(|\alpha\rangle\langle\alpha|)_A^T\sigma_2$ is also a pure state. Finally, the minimum in the third line is easily seen to vanish.

Having established that $\rho_S(2/3)$ is the nearest state to ρ_S in $\mathcal{S}$, according to Theorem 6.1 in [140] one can construct a witness for ρ_S as $\tilde{\mathcal{W}} = c_0\mathcal{I} + \rho_S(2/3) - \rho_S$, with $c_0 = \mathrm{tr}(\rho_S(2/3)(\rho_S - \rho_S(2/3)) = 1/24$, so that $\tilde{\mathcal{W}} \propto \mathcal{I} - \sum_{i=1}^3 \sigma_i^{\otimes 4} = \mathcal{W}$. As $\rho_S(2/3)$ has full rank, Theorem 6.1 in [140] also assures that $\mathcal{W}$ is optimal, i.e., there is no witness $\mathcal{W}'$ that detects all the states detected by $\mathcal{W}$ and some more.

4.3 Experiment

Smolin states can be prepared in the following way. Two sources of entangled pairs produce a state of the form $|\phi^+\rangle_{AB} \otimes |\phi^+\rangle_{CD}$, where $|\phi^\pm\rangle = \frac{1}{\sqrt{2}}(|00\rangle \pm |11\rangle)$. One then applies randomly, but with equal weight, one of the rotations σ^μ, $\mu = 0, \ldots, 3$, with σ^0 the identity, simultaneously to both entangled pairs, i.e., $\sigma_A^\mu|\phi^+\rangle_{AB} \otimes \sigma_C^\mu|\phi^+\rangle_{CD}$. Different levels of white noise can be created by choosing a probability, p, where the rotations are applied in an uncorrelated fashion.

In our experiment, we take this approach to generate a four-photon Smolin state of the form in Eq. (4.2). As shown in Fig. 4.1a, we use two SPDC sources, each producing

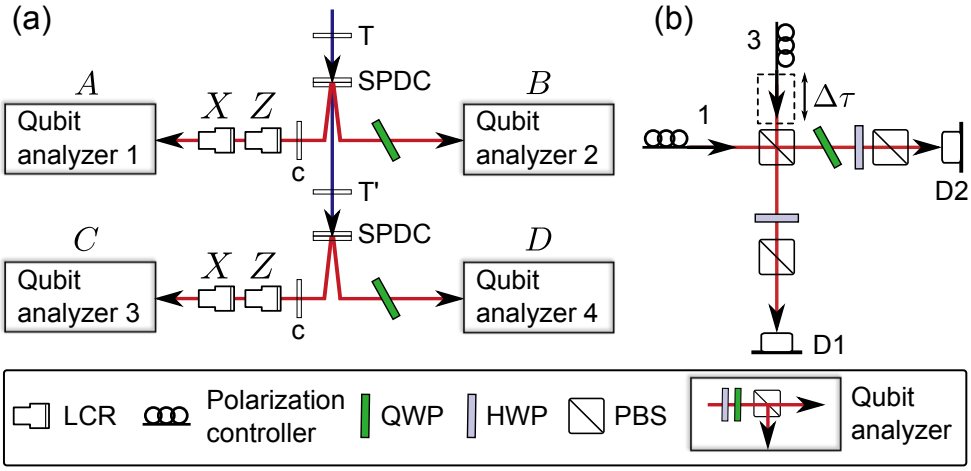

Figure 4.1: **Experimental setup to generate four-photon Smolin states.** **a**, We generate a family of Smolin states by randomly applying unitaries, using two pairs of liquid-crystal variable phase retarders (LCRs), to the initial $|\phi^+\rangle_{AB} \otimes |\phi^+\rangle_{CD}$ state produced by two SPDC sources. For each party A, B, C and D, the polarisation is analyzed with the usual HWP-QWP-PBS. Birefringent crystals (T, T', and c) are used to compensate temporal and transverse walk-off in the sources. **b**, A two-photon interferometer is used to project onto $|\phi^-\rangle_{AC}$ for entanglement unlocking between parties B and D. The delay $\Delta\tau$ is adjusted for optimum two-photon interference [141] and the QWP is used to set the phase.

polarisation entangled photon pairs in the Bell state $|\phi^+\rangle = \frac{1}{\sqrt{2}}(|HH\rangle + |VV\rangle)$. Both sources are pumped by the second harmonic (average power 830 mW, centre wavelength 395 nm) of a femtosecond Ti:Sapphire laser. Each SPDC source consists of a pair of type-I phase-matched, orthogonally oriented, 1 mm-thick BBO crystals [142, 143]. For the temporal and spatial walk-off compensations, see Section 5.3. The photons are coupled into single-mode fibers after passing through a 3 nm bandwidth filter centered at 790 nm. The phase of the entangled states can be set using QWPs in modes 2 and 4. The average singles rate produced is 250 kHz with an average coincidence rate of 36 kHz, when each analyzer is set to $|H\rangle$.

We implement the unitaries, σ^μ, via a pair of liquid-crystal variable phase retarders (LCRs) [144] in each of the two sources. In each pair, one LCR can be set to the identity or X and the other to the identity or Z, their combination allowing to apply any Pauli operation. The state of the LCRs is set by a computer using a pseudo-random number generator operating at a rate of 10 Hz.

The polarisation of each qubit is analyzed, as shown in Fig. 4.1, by monitoring both output modes of the PBS. For QST we use the over-complete set of $6^4 = 1296$ settings of the analyzers, and we record 16 four-fold coincidence counts simultaneously for 5 s. During the run, each projective measurement occurs 16 times; we sum the counts measured for these occurrences together, averaging out effects of different coupling and detector efficiencies. We repeat this run 10 times, randomizing the order of the measurement settings in each loop and summing the resulting counts. From these counts we can reconstruct our density matrix using an iterative maximum-likelihood algorithm [145].

4.4 Results

In order to test whether our prepared state is bound entangled, we directly measure the entanglement witness and determine if the reconstructed density matrix is PPT. Fig. 4.2 shows the measured witness values and minimum partial-transpose (PT) eigenvalue as a function of the amount of white noise, p. The minimum PT eigenvalue denotes the minimum of all eigenvalues of the partially transposed density matrix with respect to all

two-two bipartite cuts. When no white noise (i.e., $p = 0$) is added to our Smolin state, only one of these conditions is fulfilled: the state is entangled with a witness value of -1.269 ± 0.006 but the minimum PT eigenvalue is negative with a value -0.0273 ± 0.0006. The minimum PT eigenvalue is calculated from the maximum likelihood density matrix, and the error bars are estimated from Monte-Carlo simulations with 500 iterations each. For each iteration, we randomly vary the counts measured according to a Poisson distribution centred on the measured number of counts and use it for tomography. The magnitude of the negative eigenvalue for $p = 0$ is similar to that presented in [136]. As we increase the noise probability, the witness expectation value and the minimum PT eigenvalue also increase. Our state is bound entangled in the region where the witness is negative while the minimum PT eigenvalue is non-negative, approximately from $p = 0.42$ to $p = 0.56$.

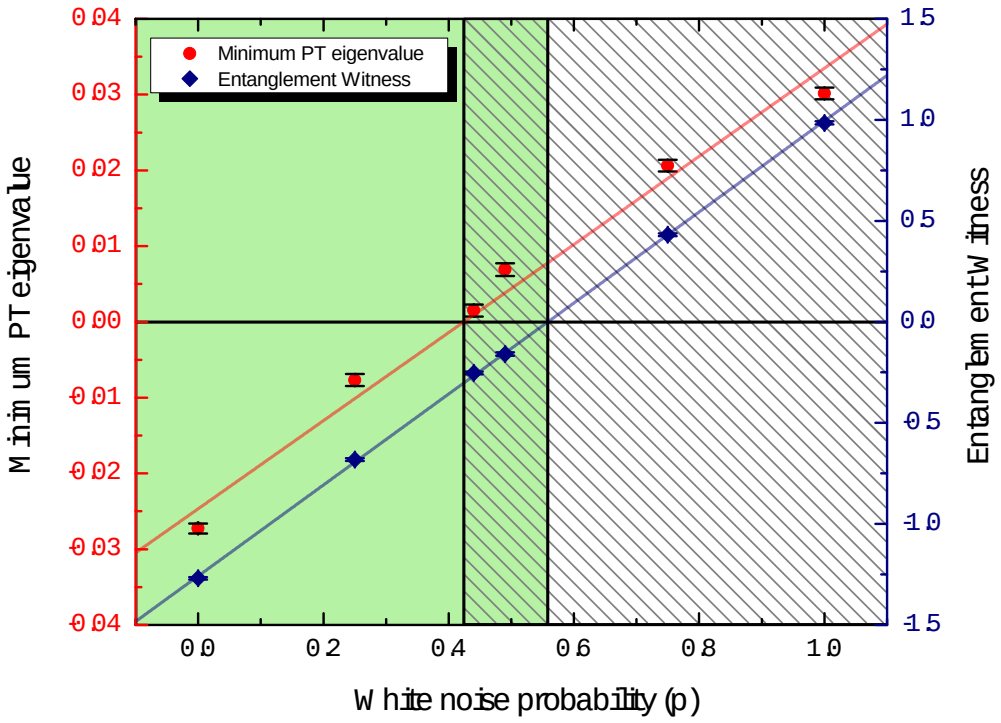

Figure 4.2: **Experimental tests for bound entanglement.** We measured the expectation value for the entanglement witness (blue diamonds, right axis) and the minimum PT eigenvalue (red circles, left axis) for various levels of white noise. The lines are best fits to the data and the error bars correspond to one standard deviation as determined by Monte-Carlo simulation. Each eigenvalue shown is the smallest among all those calculated from the set of bipartite cuts $(AB) : (CD)$, $(AC) : (BD)$, and $(AD) : (BC)$. Using our experimental data, we find that our family of generated Smolin states is entangled within the shaded region and PPT in the hatched region. In the overlapping region, the states are both entangled and PPT, i.e. bound entangled. Our state without additional noise is entangled but definitely not PPT, with a negative minimum PT eigenvalue similar to Ref. [136]. Our experimental results show that a substantial amount of noise is required to turn this value firmly positive and reach bound entanglement.

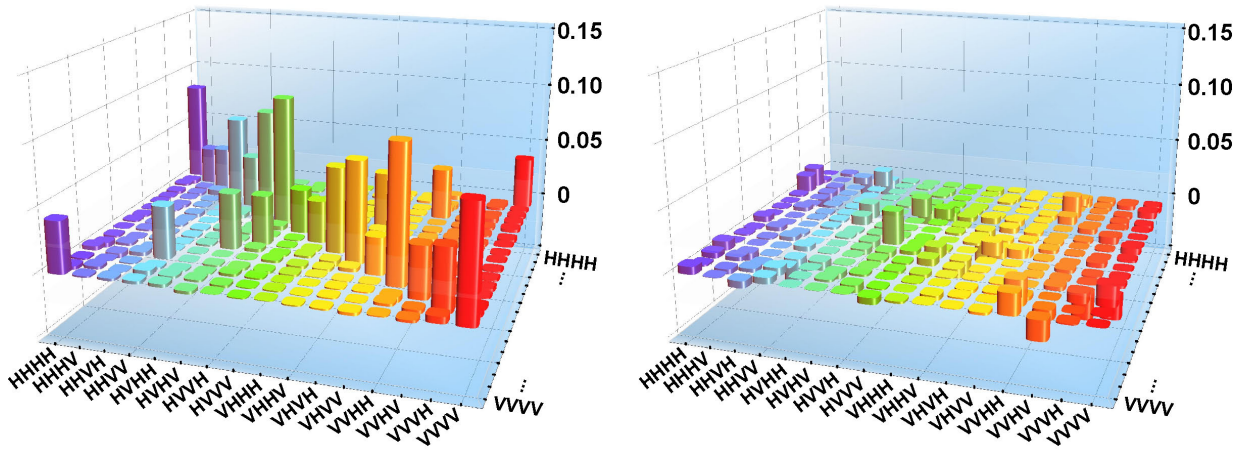

Figure 4.3: **Experimentally measured density matrix of a noisy Smolin state.** The reconstructed density matrix (real part on the left, imaginary part on the right) for a noise level of $p = 0.49$. The fidelity with the target state is $(96.83 \pm 0.05)\%$, and the measured witness and smallest PT eigenvalue are -0.159 ± 0.008 and 0.0069 ± 0.0008, respectively. From these values we see that this state is both entangled *and* PPT, i.e. bound entangled.

In particular, for $p = 0.49$ the measured value for the witness is -0.159 ± 0.008 and the minimum PT eigenvalue is 0.0069 ± 0.0008. These values satisfy *both* conditions required for bound entanglement by a wide margin. In Fig. 4.3, we show the real and imaginary part of the reconstructed density matrix for $p = 0.49$. The fidelity [146] with the target state $\rho_S(p)$ is $(96.83 \pm 0.05)\%$. We provide the directly measured tomographic counts for $p = 0.49$ in Appendix A.

Although the entanglement of a Smolin state (Eq. (4.1)) is undistillable using only LOCC, this is not the case when joint operations between any two parties are allowed [137]. In particular, by performing a Bell-state measurement, two parties, e.g. A and B, can find out which Bell pair they share. They can communicate that information to C and D, who will share the same Bell state. This is referred to as *entanglement unlocking*. In the case of the family of Smolin states described in Eq. (4.2) a Bell measurement on any two parties will lead to the preparation of a Werner state [147] in the other two: $(1-p)|\Psi^\mu\rangle\langle\Psi^\mu|_{CD} + p\frac{\mathcal{I}}{4}$.

The resulting Werner state will be entangled for $p < \frac{2}{3}$, i.e. as long as the Smolin state is entangled.

To demonstrate entanglement unlocking, we keep the noise level at $p = 0.49$, immediately after obtaining the results above, and we feed the photons of parties A and C, i.e., one from each source, through single-mode fibres into the Bell-state measurement depicted in Fig. 4.1b. After passing through the first PBS in the interferometer, both photons are projected on the state $|+\rangle$ using HWPs and PBSs. The time delay $\Delta\tau$ is set such that two-photon interference occurs [141]. A coincidence detection event between detectors D1 and D2 performs a projective measurement of modes A and C onto the Bell state $|\phi^-\rangle$. An over-complete set of two-qubit tomography measurements is performed on the qubits of parties B and D, yielding the counts reported in Table 4.2 of Appendix A. For each tomography run we record all 4 four-fold coincidences for 60 s per setting; we perform 20 loops with a randomized setting order for each loop. The reconstructed density matrix (see Fig. 4.4) has a fidelity of $(99.45 \pm 0.05)\%$ with the one expected from the experimental bound entangled state, assuming a perfect Bell-state measurement. Its tangle is positive, 0.00105 ± 0.00046, and the minimum eigenvalue of the partially transposed state is negative, -0.0160 ± 0.0035; this confirms that we have successfully unlocked entanglement between parties B and D.

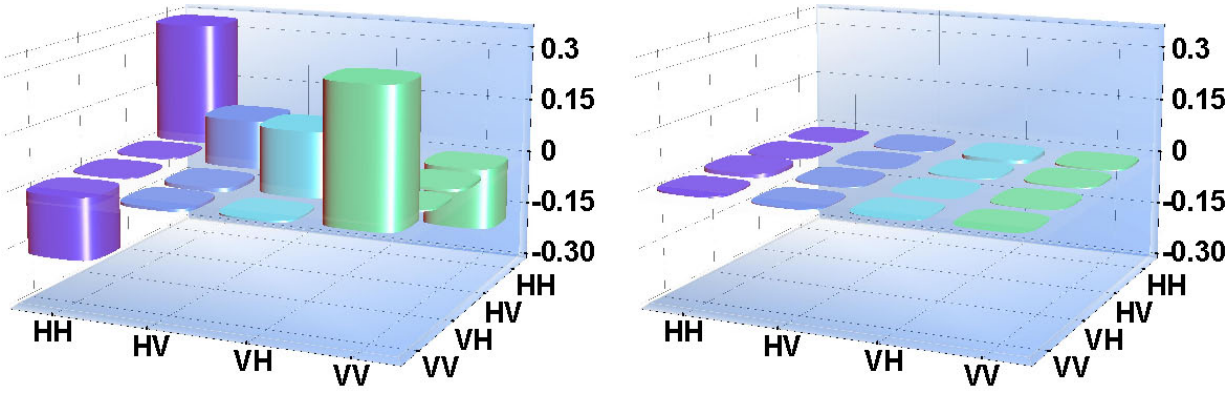

Figure 4.4: **Unlocking of entanglement from a bound entangled state.** By performing a joint measurement on the qubits of parties A and C, specifically by projecting them on the state $|\phi^-\rangle_{AC}$ using the Bell-state measurement shown in Fig. 4.1b, entanglement is unlocked between parties B and D. Here, we use our bound-entangled Smolin state with noise level $p = 0.49$. We reconstruct the density matrix of B and D (real part on the left, imaginary part on the right), given a successful Bell-state measurement on A and C. This state is entangled with a negative minimum PT eigenvalue of -0.0160 ± 0.0035 and a tangle of 0.00105 ± 0.00046, experimentally demonstrating entanglement unlocking. We achieve a fidelity of $(99.45 \pm 0.05)\%$ with the state expected, given the reconstructed four-qubit density matrix of Fig.4.3.

4.5 Conclusion

We demonstrated experimental bound entanglement, for the first time convincingly satisfying its two defining criteria: entanglement and undistillability. To achieve the latter property, we added sufficient white noise to clearly fulfill the PPT criterion while still maintaining non-separability. Without additional noise, our Smolin state is non-PPT by an amount that is relatively small, but statistically significant, and we must add a *substantial* amount of noise—almost 50%—to turn it PPT. Clearly, it is difficult to achieve the critical PPT condition without completely losing entanglement in experimentally produced Smolin states. Once we achieved the preparation of bound entanglement, we demonstrated en-

tanglement unlocking, realizing all of the conceptually important characteristics of Smolin states. Our results open the door to applications of bound entanglement in experimental quantum information science.

Appendix A

Measured Counts for Entanglement Witness

states	counts	states	counts	states	counts
$\|H,H,H,H\rangle$	3834	$\|+,+,+,+\rangle$	3687	$\|R,R,R,R\rangle$	3810
$\|H,H,H,V\rangle$	1983	$\|+,+,+,-\rangle$	1751	$\|R,R,R,L\rangle$	1833
$\|H,H,V,H\rangle$	1760	$\|+,+,-,+\rangle$	1801	$\|R,R,L,R\rangle$	1813
$\|H,H,V,V\rangle$	4344	$\|+,+,-,-\rangle$	3863	$\|R,R,L,L\rangle$	3825
$\|H,V,H,H\rangle$	1531	$\|+,-,+,+\rangle$	1658	$\|R,L,R,R\rangle$	1801
$\|H,V,H,V\rangle$	4050	$\|+,-,+,-\rangle$	4125	$\|R,L,R,L\rangle$	4021
$\|H,V,V,H\rangle$	3627	$\|+,-,-,+\rangle$	4276	$\|R,L,L,R\rangle$	4029
$\|H,V,V,V\rangle$	1641	$\|+,-,-,-\rangle$	1738	$\|R,L,L,L\rangle$	1742
$\|V,H,H,H\rangle$	1500	$\|-,+,+,+\rangle$	1524	$\|L,R,R,R\rangle$	1711
$\|V,H,H,V\rangle$	4174	$\|-,+,+,-\rangle$	3891	$\|L,R,R,L\rangle$	3745
$\|V,H,V,H\rangle$	3608	$\|-,+,-,+\rangle$	4023	$\|L,R,L,R\rangle$	3954
$\|V,H,V,V\rangle$	1617	$\|-,+,-,-\rangle$	1608	$\|L,R,L,L\rangle$	1842
$\|V,V,H,H\rangle$	3737	$\|-,-,+,+\rangle$	4094	$\|L,L,R,R\rangle$	3845
$\|V,V,H,V\rangle$	1909	$\|-,-,+,-\rangle$	1754	$\|L,L,R,L\rangle$	1905
$\|V,V,V,H\rangle$	1709	$\|-,-,-,+\rangle$	1843	$\|L,L,L,R\rangle$	1963
$\|V,V,V,V\rangle$	4217	$\|-,-,-,-\rangle$	3990	$\|L,L,L,L\rangle$	3970
exp. values	$\langle\sigma_z^{\otimes 4}\rangle = 0.3966 \pm 0.0075$		$\langle\sigma_x^{\otimes 4}\rangle = 0.4005 \pm 0.0043$		$\langle\sigma_y^{\otimes 4}\rangle = 0.3621 \pm 0.0043$

Table 4.1: **Counts for the measurement of the entanglement witness.** The counts are four-fold coincidences measured to determine the expectation value of the entanglement witness, $\langle\mathcal{W}\rangle = 1 - \sum_{i=1}^{3} \langle\sigma_i^{\otimes 4}\rangle$, for a noise level of $p = 0.49$. We integrated over 60 s (6 s in each of the ten loops) per measurement setting. Because we use all PBS outputs, the effective measurement time is 16×60 s $= 960$ s per setting.

		Photon D					
		$\|H\rangle$	$\|V\rangle$	$\|+\rangle$	$\|-\rangle$	$\|R\rangle$	$\|L\rangle$
Photon B	$\|H\rangle$	4547	1736	3195	3053	3142	3026
	$\|V\rangle$	2274	4626	3463	3544	3539	3464
	$\|+\rangle$	3244	3039	1935	4188	3208	3117
	$\|-\rangle$	3261	3185	4277	2098	3385	3325
	$\|R\rangle$	3560	3207	3282	3183	4310	2283
	$\|L\rangle$	3266	3308	3062	3176	2204	4230

Table 4.2: **QST counts for unlocked entanglement.** We project the qubits of parties A and C on $|\phi^-\rangle$ and perform an over-complete set of tomography measurements on the qubits of parties B and D. Each row corresponds to a fixed setting for B, and each column to a fixed setting of D. All counts are four-fold coincidence events. We repeated the set of 36 measurements 20 times, and for each measurement setting we integrated over 60 s. Taking into account the additional factor of 4 due to our use of all PBS outcomes, this results in an overall measurement time of $4 \times 20 \times 60$ s $= 4800$ s per setting.

Chapter 5

Quantum computing with a simulated valence-bond solid

Most of the material in this Chapter is published[1] in the following:

Reference: R. Kaltenbaek*, J. Lavoie*, B. Zeng, S. D. Bartlett and K. J. Resch, Optical one-way quantum computing with a simulated valence-bond solid, *Nature Physics* **6**, 850-854 (2010) (* contributed equally)

Contributions: B.Z. and S.D.B. proposed the experiment and provided theoretical support. R. K., K. J. R and I designed the experiment. I built the setup with R. K and I carried out the experiment including preliminary data analysis. R. K. analysed the final data. I wrote and edited the paper with my coauthors.

[1] No copyrights from the journal is required to include the article (all or part) in this thesis.

5.1 Introduction

In the standard circuit model of quantum computation [148], information is carried by qubits. The computation proceeds dynamically via unitary single-qubit logic gates and multiple-qubit entangling gates. Apart from these entangling gates the qubits are fully isolated from each other. Computations in the one-way model, on the other hand, are performed via single-qubit measurements on a strongly-correlated, i.e., entangled, resource state [51]. The one-way model has led to some of the highest estimated error thresholds for fault-tolerant quantum computation [149, 150], and to a series of experimental demonstrations of quantum logic gates [53, 54, 151, 152, 153, 154], wherein the technical requirements can be much simpler than for the circuit model. This is particularly true of optical implementations, where the resource requirements for one-way quantum computing are significantly lower [155], and the predicted error thresholds significantly higher [156], than for any other approach to quantum computation.

Because qubits in the one-way model are not isolated but rather interact strongly with each other, this approach lends itself more naturally for implementations in condensed-matter systems. But, out of the vast variety of strongly-coupled quantum many-body systems, can we find one that has a ground state we can use as a resource for quantum computing? That seems unlikely if this ground state is to be the cluster state, because the cluster state is *not* the ground state of a strongly-coupled many-body system with a Hamiltonian consisting of two-body interactions [157, 158]. As a result, the search for alternative resource states has attracted a lot of interest recently. Although up to now little is known about the requirements potential resource states for the one-way model have to meet, and although most states are in fact useless for this task [159], a handful of alternative states have been identified [160, 161, 162, 163, 164]. All of these states can be described in the framework of matrix product states or projected entangled pair states [160, 161, 162, 165].

A promising candidate is the ground state of a spin model studied by Affleck, Kennedy, Lieb, and Tasaki (AKLT) [166]. This valence-bond-solid state (see Figure 5.1a) appears as the unique gapped ground state of a rotationally-invariant nearest-neighbour two-body Hamiltonian on a spin-1 chain. The AKLT state possesses diverging localisable entangle-

ment length [167] and, remarkably, can serve as a resource for one-way quantum computation [160, 162, 163, 168]. Because the Hamiltonian is frustration free, i.e. the ground state minimises the energy of each local term of the Hamiltonian, measurements in the course of the computation leave the remaining particles in their ground state. Operations leaving the computational subspace are penalised by the energy gap protecting the AKLT state. Universal quantum computation can be achieved via dynamical coupling of several AKLT states, where each can be regarded as 'quantum computational wires' [160, 162, 163, 168]. These properties render the AKLT state an attractive alternative to cluster states as a more natural resource for quantum computing in condensed-matter systems.

In this chapter we show how to prepare an AKLT state, a resource for measurement-based quantum computing, using linear optics. We also demonstrate its use to implement single-qubit quantum logic gates.

5.2 Theory

A detailed discussion of theoretical aspects of simulating AKLT states with quantum optics and their use in one-way quantum computation is given in Ref. [169]. Here we will focus on a simple AKLT state for a qubit-qutrit-qubit system given by

$$|\psi_{AKLT}\rangle = \frac{1}{\sqrt{6}}|H,1,V\rangle + \frac{1}{\sqrt{6}}|V,1,H\rangle - \frac{1}{\sqrt{3}}|H,2,H\rangle - \frac{1}{\sqrt{3}}|V,0,V\rangle. \tag{5.1}$$

In our case, the qutrit states $|0\rangle$, $|1\rangle$, $|2\rangle$ correspond to the biphoton states $\frac{1}{\sqrt{2}}a_H^\dagger a_H^\dagger|\text{vac}\rangle$, $a_H^\dagger a_V^\dagger|\text{vac}\rangle$, $\frac{1}{\sqrt{2}}a_V^\dagger a_V^\dagger|\text{vac}\rangle$, respectively. Here, $|\text{vac}\rangle$ is the vacuum state, and $a_H^\dagger$ and $a_V^\dagger$ are photon creation operators.

Quantum computation with AKLT states is different from computing with cluster states in a number of ways. The elementary physical units are spin-1 systems (qutrits) instead of spin-$\frac{1}{2}$ systems (qubits), although it is still qubits that are encoded as 'logical' information. Adaptive measurements allow the performance of non-Pauli operations, including Clifford gates. Single-qubit rotations can be performed around any Cartesian axis. These operations are probabilistic, rather than deterministic, and succeed with probability $\frac{2}{3}$. When

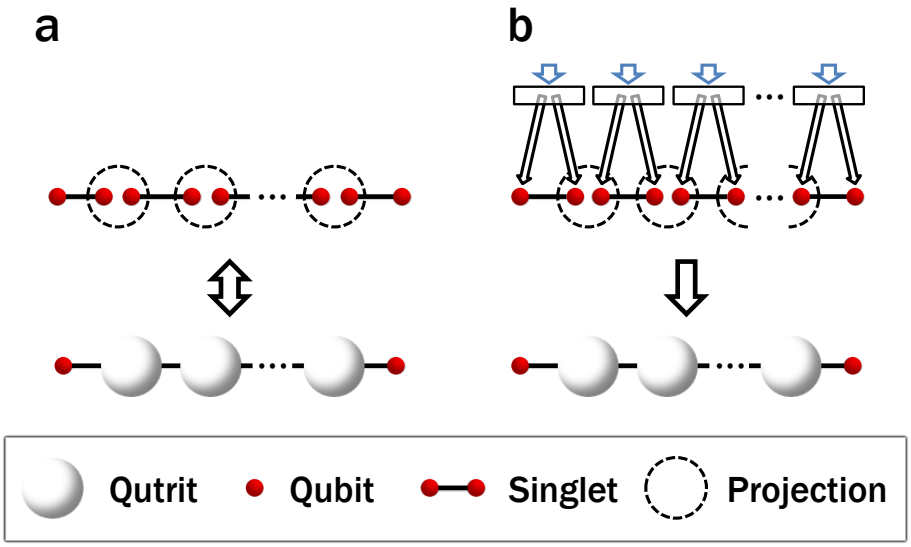

Figure 5.1: **AKLT states.** **a**, The AKLT state [166] is a valence-bond solid and can be represented by a chain of spin-$\frac{1}{2}$ singlet states where adjoining qubits of neighbouring pairs are projected on the triplet subspace, i.e. the subspace symmetric with respect to swapping of the two qubits. At either end of the chain a boundary qubit remains, ensuring that the ground state is non-degenerate. **b**, One can simulate an AKLT state with a chain of sources producing singlet states and projecting pairs of particles on the triplet subspace.

an operation fails, it performs a heralded logical-identity operation, i.e. a teleportation of the logical information along the chain. The operation can then be reattempted on the next qutrit until it succeeds. Combinations of such rotations allow the implementation of arbitrary single-qubit quantum logic gates.

Although a number of one-dimensional spin chains are well-described by the AKLT Hamiltonian, most prominently $Ni(C_2H_8N_2)_2NO_2(ClO_4)$ (NENP) [170], up to now experimental techniques do not allow the single-spin measurements necessary for one-way quantum computation. Yet, one of the fundamental and most appealing motivations for quantum computing, is the possibility to simulate aspects of quantum systems that cannot directly be studied [171]. Because the AKLT state is a valence-bond solid state (see

Figure 5.1a), we can simulate it via a chain of spin-$\frac{1}{2}$ singlet states, for example polarisation-entangled photon pairs, where adjoining particles of neighbouring pairs are projected on the symmetric triplet subspace; see Figure 5.1b. While this approach does not allow to analyse the dynamics of the corresponding solid-state system, it allows the direct production of the AKLT state, and to use it for one-way quantum computation.

5.3 Experiment

Source

The light source is a Ti:Sapphire femtosecond laser, centred at 790 nm with 10 nm FWHM bandwidth, 2.9 W average output power and 80 MHz repetition rate. Second-harmonic generation in a 2 mm thick BiBO crystal yields a beam of 780 mW power, centred around 395 nm, with 1.5 nm FWHM bandwidth. The entangled photon pairs are generated using two separate type-I SPDC sources [142], also described in Section 3.3. Each source consists of a pair of 1 mm thick BBO crystals, their optical axes oriented perpendicular to each other. Longitudinal walk off in the SPDC crystals is compensated using 2.5 mm of quartz and 1 mm of α-BBO crystal before the first SPDC source, and a 2 mm α-BBO and a 1 mm quartz crystal before the second[2]. Additional transverse walk-off is compensated by placing 1 mm thick BiBO crystals cut at $\theta = 152.6°$ and $\phi = 0°$ in modes 2 and 3 (see Figure 5.2a). All photons pass through 3-nm bandwidth filters. The phases in the setup and the polarisation rotation in the single-mode fibres are set such that the sources produce singlet states in modes 1 & 2 and 3 & 4. In modes 1 & 2 we measure a fidelity of $(96.9 \pm 0.5)\%$ with the ideal singlet state $|\psi^-\rangle \equiv \frac{1}{\sqrt{2}}(|HV\rangle - |VH\rangle)$. For the second source the fidelity is $(96.9 \pm 0.6)\%$.

We had single count rates around 200 kHz in the qubit analyzers 1 and 2 (see Figure 5.2a), and single count rates of 80 kHz in the detectors D_5 and D_6 in the qutrit

[2]In principle, no compensation would be necessary between the two sandwiched crystals. We had the second source oriented at 90 degrees relative to the first to minimize transverse walk-off, and therefore, we had to double the longitudinal compensation.

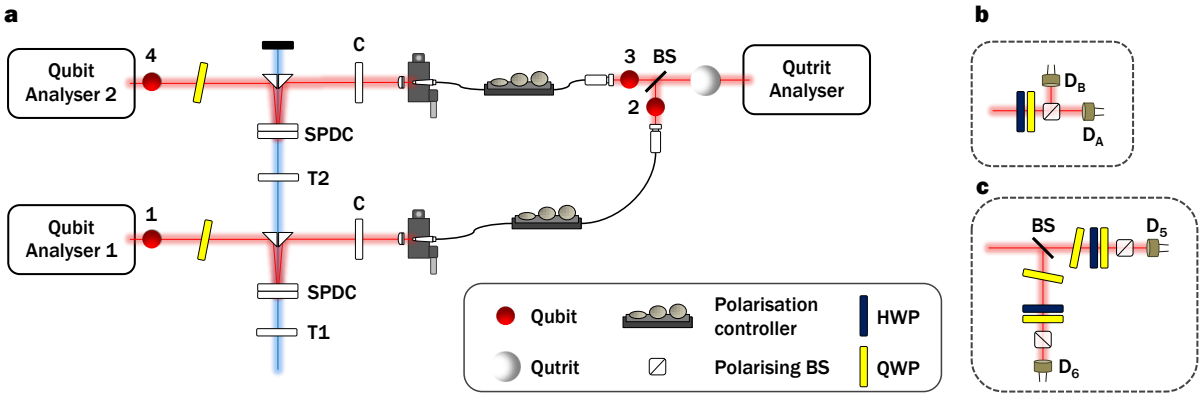

Figure 5.2: **Experimental Setup.** **a**, Two type-I SPDC sources are used to generate polarisation-entangled pairs. Longitudinal and transverse walk-off are compensated with birefringent crystals T1, T2 and C. All photons are coupled into single-mode fibers. Polarisation rotation in the fibres is compensated with polarisation controllers, and the phase is adjusted by tilting QWP's. Photons in modes 2 and 3 are fed into a 50:50 BS. Detecting two photons in one of the BS outputs projects these photons on the symmetric qutrit subspace and can be treated as a qutrit. **b**, Each qubit analyzer consists of a HWP, QWP, PBS and two detectors, monitoring both outputs of the polarising BS. **c**, In the qutrit analyzer the biphoton forming the qutrit is probabilistically split up using a BS. Phases introduced at the BS are compensated by tilted QWPs. A combination of QWPs and HWPs allows to project the qutrit onto a state of our choice. A successful projection corresponds to a coincidence event between detectors D_5 and D_6.

analyzer (see Figure 5.2c). The two-fold coincidence count rate for the first source was 7.4 kHz between qubit analyzer 1 and D_5 in the qutrit analyzer. For the second source the two-fold coincidence count rate was 5.9 kHz between qubit analyzer 2 and D_5 in the qutrit analyzer.

Interferometer and Qutrit Projection

One photon of each pair is measured directly at the source, using polarisation analyzers. The modes for both measurement outcomes are coupled into single-mode fibres and monitored via single-photon detectors (Perkin-Elmer, SPCM-4Q4C). The two remaining photons are coupled into single-mode fibres and sent to a quantum interferometer and analyzer setup. The input modes of the interferometer are overlapped at a 50:50 BS. If the input photons are set to have the same polarisation, HOM interference [141] occurs. Postselecting on four-fold events with one photon in mode 1, one in mode 4 and two photons in the output mode of the BS indicated in Fig. 5.2a, we observe constructive HOM interference with a visibility of $95.7 \pm 3.7\%$.

It will depend on the biphoton state in modes 2 and 3 whether the two photons leave through the same or different BS outputs [18]. In particular, coincidence detection events between two different BS outputs only occur for the two-photon singlet state. By postselecting on a biphoton excitation in one output mode of the BS, the biphoton is retroactively projected onto a symmetric subspace and can be described as a qutrit [172]. This is identical to the symmetrisation needed to generate an AKLT state [166] (see Fig. 5.1). We measure this qutrit using the analyzer outlined in Fig. 5.2c.

The analyzer works by probabilistically splitting up the biphoton at a BS, and by performing a qubit projective measurement on each of the output modes of the BS. We project on a given qutrit state by projecting the two photons on corresponding qubit states. In particular, the photon in mode $m = 5, 6$ of the qutrit analyzer is projected on state $|\psi_m\rangle = \cos\alpha_m|H\rangle + e^{i\chi_m}\sin\alpha_m|V\rangle$. A successful projective measurement of a qutrit corresponds to a coincidence event between detectors D_5 and D_6. To calculate which qutrit state such a coincidence event signals we can propagate our two-qubit state $|\psi_5\rangle \otimes |\psi_6\rangle$

back through the BS, neglecting the unused port. The (unnormalised) two-photon state then becomes:

$$\frac{1}{2}\left[\cos\alpha_5\cos\alpha_6 a_H^\dagger a_H^\dagger + \left(e^{i\chi_5}\cos\alpha_6\sin\alpha_5 + e^{i\chi_6}\cos\alpha_5\sin\alpha_6\right) a_H^\dagger a_V^\dagger + e^{i(\chi_5+\chi_6)}\sin\alpha_5\sin\alpha_6 a_V^\dagger a_V^\dagger\right]|\text{vac}\rangle. \tag{5.2}$$

In our qutrit basis we can write this as:

$$\frac{1}{\sqrt{2}}\cos\alpha_5\cos\alpha_6|0\rangle + \frac{1}{2}\left(e^{i\chi_5}\cos\alpha_6\sin\alpha_5 + e^{i\chi_6}\cos\alpha_5\sin\alpha_6\right)|1\rangle + \frac{1}{\sqrt{2}}e^{i(\chi_5+\chi_6)}\sin\alpha_5\sin\alpha_6|2\rangle. \tag{5.3}$$

In general, the success probability of this projective qutrit measurement depends on the qutrit state. For example, to project onto the biphoton state $a_H^\dagger a_H^\dagger|\text{vac}\rangle$, we set both analyzers to $|H\rangle$. Given that the biphoton is in the correct state, a coincidence will occur with probability $\frac{1}{2}$ because of the probabilistic splitting of the photons at the BS. As a second example, a projection on the biphoton state $a_H^\dagger a_V^\dagger|\text{vac}\rangle$, we choose $|\psi_5\rangle = |H\rangle$ and $|\psi_6\rangle = |V\rangle$. If the biphoton is in the right state, the success probability will only be $\frac{1}{4}$ because the photons can be split in four possible ways, and only one leads to a coincidence event.

We perform QST on our qubit-qutrit-qubit state using a maximum likelihood technique [173, 174]. The set of measurements for the two qubits was $|H\rangle$, $|V\rangle$, $|+\rangle$, $|-\rangle$, $|R\rangle$, and $|L\rangle$. In Table 5.1 we list the set of qutrit measurements as well as the corresponding parameters α_m and χ_m for the settings of the qubit measurements in the qutrit analyzer. The table also shows the probability with which each of the projections succeeds given that the biphoton is in the corresponding qutrit state.

To demonstrate the use of AKLT states for quantum computation, we realise single-qubit rotations around the $\hat{x}$, $\hat{y}$ and $\hat{z}$ axis of the Bloch sphere. We begin the computation by projecting the first boundary qubit (in mode 1) onto some qubit state $|\psi_1\rangle$. By doing so, we effectively prepare the logical state $|\psi_2^\perp\rangle$, where $\langle\psi|\psi^\perp\rangle = 0$. Rotations $R_x(\theta)$, $R_y(\theta)$ or $R_z(\theta)$ of the logical state by an angle θ around the respective coordinate axis, require a projection of the qutrit onto one of the corresponding states given in Table 5.2. For more details, Table 5.3 also lists the parameters α_m and χ_m of Eq. 5.3. We denote the three outcomes of each qutrit basis as 'plus', 'minus' and 'id'. Each is expected to occur

	$\|\mathbf{0}\rangle$	$\|\mathbf{1}\rangle$	$\|\mathbf{2}\rangle$	$\frac{\|\mathbf{0}\rangle+\|\mathbf{1}\rangle}{\sqrt{2}}$	$\frac{\|\mathbf{0}\rangle-\|\mathbf{1}\rangle}{\sqrt{2}}$	$\frac{\|\mathbf{1}\rangle+\|\mathbf{2}\rangle}{\sqrt{2}}$	$\frac{\|\mathbf{1}\rangle-\|\mathbf{2}\rangle}{\sqrt{2}}$	$\frac{\|\mathbf{2}\rangle+\|\mathbf{0}\rangle}{\sqrt{2}}$	$\frac{\|\mathbf{2}\rangle-\|\mathbf{0}\rangle}{\sqrt{2}}$	$\frac{\|\mathbf{0}\rangle+i\|\mathbf{1}\rangle}{\sqrt{2}}$	$\frac{\|\mathbf{0}\rangle-i\|\mathbf{1}\rangle}{\sqrt{2}}$	$\frac{\|\mathbf{1}\rangle+i\|\mathbf{2}\rangle}{\sqrt{2}}$	$\frac{\|\mathbf{1}\rangle-i\|\mathbf{2}\rangle}{\sqrt{2}}$	$\frac{\|\mathbf{2}\rangle+i\|\mathbf{0}\rangle}{\sqrt{2}}$	$\frac{\|\mathbf{2}\rangle-i\|\mathbf{0}\rangle}{\sqrt{2}}$
α_5	0	0	$\frac{\pi}{2}$	0	0	$\frac{\pi}{2}$	$\frac{\pi}{2}$	$-\frac{\pi}{4}$	π	0	0	$\frac{\pi}{2}$	$\frac{\pi}{2}$	$-\frac{\pi}{4}$	$-\frac{\pi}{4}$
χ_5	0	0	0	0	0	0	0	$\frac{\pi}{2}$	$-\frac{\pi}{4}$	0	0	0	0	$\frac{\pi}{4}$	$-\frac{\pi}{4}$
α_6	0	$\frac{\pi}{2}$	$\frac{\pi}{2}$	ξ	ξ	η	η	$\frac{\pi}{4}$	0	ξ	ξ	η	η	$\frac{\pi}{4}$	$\frac{\pi}{4}$
χ_6	0	0	0	0	π	0	π	$\frac{\pi}{2}$	$\frac{\pi}{4}$	$\frac{\pi}{2}$	$-\frac{\pi}{2}$	$\frac{\pi}{2}$	$-\frac{\pi}{2}$	$\frac{\pi}{4}$	$-\frac{\pi}{4}$
p	$\frac{1}{2}$	$\frac{1}{4}$	$\frac{1}{2}$	$\frac{1}{3}$	$\frac{1}{3}$	$\frac{1}{3}$	$\frac{1}{3}$	$\frac{1}{4}$	$\frac{1}{4}$	$\frac{1}{3}$	$\frac{1}{3}$	$\frac{1}{3}$	$\frac{1}{3}$	$\frac{1}{4}$	$\frac{1}{4}$

Table 5.1: **Analyzer parameters for qutrit measurements used for QST**. Each qutrit measurement is implemented by splitting the biphoton probabilistically at a beam splitter and projecting the two photons ($m = 5, 6$) on $|\psi_m\rangle = \cos\alpha_m|H\rangle + e^{i\chi_m}\sin\alpha_m|V\rangle$. For brevity, we use the definitions $\xi = \arccos(\frac{1}{\sqrt{3}})$ and $\eta = \arccos(\sqrt{\frac{2}{3}})$, and p denotes the success probability for a given qutrit projection. These success probabilities are taken into account by our QST algorithm.

with probability 1/3. Up to a known Pauli error [51, 162, 163], which can be corrected as indicated in Table 5.2, the outcomes 'plus' and 'minus' signal a successful rotation, and the outcome 'id' signals the logical identity, i.e., a rotation by 0°. As a result, a successful rotation is achieved with probability 2/3. For $\theta = 0$, every outcome heralds the logical identity [169]. This can be used to teleport logical information along the wire, for example to a position where the wire is coupled to another, or to the read-out position.

Rot.	plus		minus		id	
	state	corr.	state	corr.	state	corr.
$R_x(\theta)$	$\cos\frac{\theta}{2}\|y\rangle + i\sin\frac{\theta}{2}\|z\rangle$	XZ	$i\sin\frac{\theta}{2}\|y\rangle + \cos\frac{\theta}{2}\|z\rangle$	Z	$\|x\rangle$	X
$R_y(\theta)$	$\cos\frac{\theta}{2}\|z\rangle + \sin\frac{\theta}{2}\|x\rangle$	Z	$-\sin\frac{\theta}{2}\|z\rangle + \cos\frac{\theta}{2}\|x\rangle$	X	$\|y\rangle$	XZ
$R_z(\theta)$	$\cos\frac{\theta}{2}\|x\rangle + i\sin\frac{\theta}{2}\|y\rangle$	X	$i\sin\frac{\theta}{2}\|x\rangle + \cos\frac{\theta}{2}\|y\rangle$	XZ	$\|z\rangle$	Z

Table 5.2: **Qutrit measurement bases and Pauli corrections.** Single-qubit rotations are realised by a projective measurement in a corresponding qutrit basis that has three possible outcomes: 'plus', 'minus' and 'id'. The qutrit states $|x\rangle$, $|y\rangle$, and $|z\rangle$ are defined as $\frac{1}{2}\left(a_H^\dagger a_H^\dagger - a_V^\dagger a_V^\dagger\right)|\text{vac}\rangle$, $\frac{1}{2}\left(a_H^\dagger a_H^\dagger + a_V^\dagger a_V^\dagger\right)|\text{vac}\rangle$, and $a_H^\dagger a_V^\dagger|\text{vac}\rangle$, respectively, and X, $XZ = iY$, and Z indicate the Pauli correction that has to be applied to the read-out qubit depending on measurement outcome and measurement basis.

To prepare our logical input state, we project the first qubit on one of a set of states: $|H\rangle$, $|V\rangle$, $|\pm\rangle$, $|\mathfrak{h}^\pm\rangle$, $|\mathfrak{m}^\pm\rangle$. Here, $|\pm\rangle \equiv (|H\rangle \pm |V\rangle)/\sqrt{2}$, $|\mathfrak{h}^\pm\rangle$ are the eigenstates of the Hadamard operator, and $|\mathfrak{m}^+\rangle \equiv \cos(\frac{\xi}{2})|H\rangle + \mathrm{e}^{i\frac{\pi}{4}}\sin(\frac{\xi}{2})|V\rangle$, $|\mathfrak{m}^-\rangle \equiv \sin(\frac{\xi}{2})|H\rangle - \mathrm{e}^{i\frac{\pi}{4}}\cos(\frac{\xi}{2})|V\rangle$ are the 'magic states' [150] with $\xi = \arccos(\frac{1}{\sqrt{3}})$ and $\langle\mathfrak{m}^-|\mathfrak{m}^+\rangle = 0$. For each axis of rotation we choose 10 angles $\theta = \left\{0, \frac{\pi}{8}, \frac{\pi}{4}, \frac{3\pi}{8}, \frac{\pi}{2}, \frac{3\pi}{4}, \pi, \frac{5\pi}{4}, \frac{3\pi}{2}, \frac{7\pi}{4}\right\}$ and project the qutrit on the corresponding state (see Table 5.2) for the 'plus' and 'minus' outcomes. We project on the 'id' outcome once for every input state and rotation axis. Finally, while monitoring four-fold events, we reconstruct the density matrix of the computational outcome by performing QST on the last qubit.

5.4 Results

Here, we experimentally demonstrate the generation of photonic AKLT states and their application for one-way quantum computation. We produced two singlet states, $|\psi^-\rangle = (|HV\rangle - |VH\rangle)/\sqrt{2}$, in four distinct spatial modes and from these two singlets we created an AKLT state consisting of two boundary spin-1/2 systems and one spin-1 system. To

Rot.	plus				minus				id			
	α_5	χ_5	α_6	χ_6	α_5	χ_5	α_6	χ_6	α_5	χ_5	α_6	χ_6
$R_x(\theta)$	$\frac{\theta-\pi}{4}$	$\frac{\pi}{2}$	$\frac{3\pi-\theta}{4}$	$-\frac{\pi}{2}$	$\frac{\theta}{4}$	$\frac{\pi}{2}$	$\frac{\pi}{2}-\frac{\theta}{4}$	$-\frac{\pi}{2}$	$\frac{\pi}{4}$	π	$\frac{3\pi}{4}$	$-\pi$
$R_y(\theta)$	$\frac{\theta}{4}$	π	$\frac{\pi}{2}+\frac{\theta}{4}$	$-\pi$	$\frac{\pi-\theta}{4}$	0	$\frac{3\pi-\theta}{4}$	0	$\frac{\pi}{4}$	$\frac{\pi}{2}$	$\frac{\pi}{4}$	$-\frac{\pi}{2}$
$R_z(\theta)$	$\frac{-\pi}{4}$	$-\frac{\theta}{2}$	$\frac{\pi}{4}$	$-\frac{\theta}{2}$	$\frac{-\pi}{4}$	$\frac{\pi-\theta}{2}$	$\frac{\pi}{4}$	$\frac{\pi-\theta}{2}$	0	$\frac{\pi}{2}$	$\frac{\pi}{2}$	$-\frac{\pi}{2}$

Table 5.3: **Analyzer parameters for qutrit measurements used for rotation gates**. In the qutrit analyzer, one photon is projected on $|\psi_5\rangle$, the second one on $|\psi_6\rangle$. Each qutrit measurement has three possible outcomes, 'plus', 'minus' and 'id' corresponding to three different sets of parameters for the qutrit analyzer. We provide the settings for rotations around each of the Cartesian axes.

verify the faithful production of the AKLT state in our experiment, we perform QST on the qubit-qutrit-qubit system (as described in Section 5.3) and reconstruct the density matrix shown in Figure 5.3. The fidelity[3] with the ideal AKLT state is $(87.1 \pm 0.4)\%$, calculated with a Monte-Carlo simulation with 420 iterations on the observed counts.

[3] $F(\rho,\sigma) = \left(\mathrm{Tr}\sqrt{\sqrt{\sigma}\rho\sqrt{\sigma}}\right)^2$ for the fidelity between two quantum states [146].

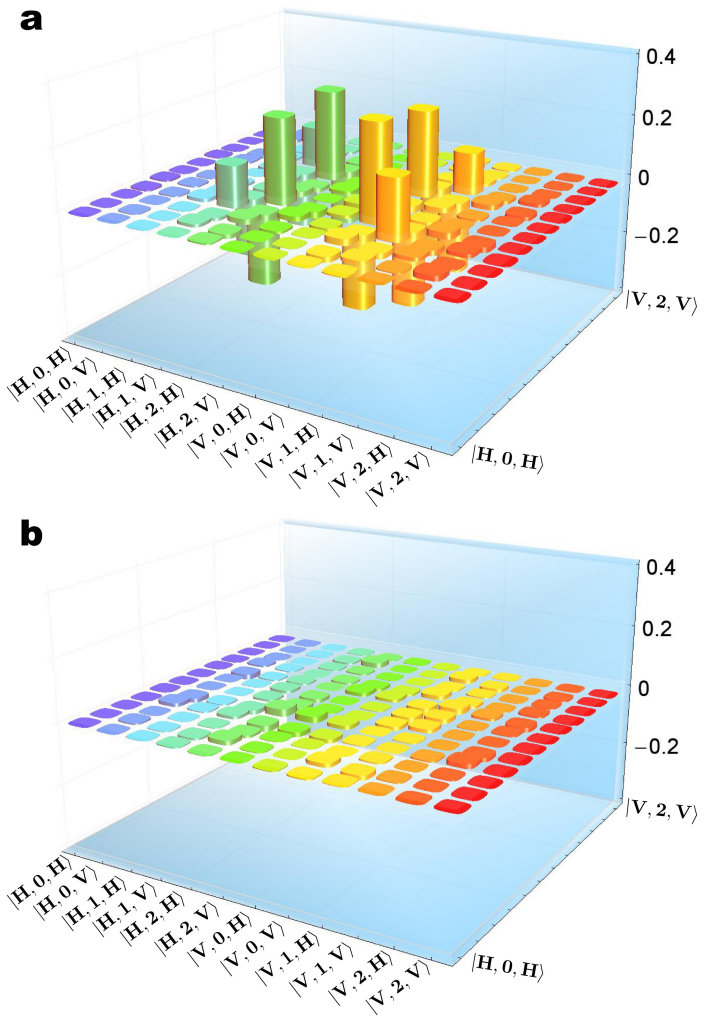

Figure 5.3: **Tomographic reconstruction of our photonic AKLT state. a**, real and **b**, imaginary part of the reconstructed density matrix. The fidelity with the ideal AKLT state is $(87.1 \pm 0.4)\%$.

Figure 5.4 shows measurement results for single-qubit rotations of the logical input state $|H\rangle$ (i.e. projecting the first qubit on $|V\rangle$) around the three rotation axes. The plots in Figure 5.4(a-c) show the coordinates of the rotated Bloch vectors as compared with

the theoretical expectation. In Table 5.4 we list the fidelities for rotations of $|H\rangle$ as well as the averaged fidelities for all logical input states prepared. The probabilities for the three qutrit measurements, averaged over all input states, rotations and rotation angles, are measured to be 0.34 ± 0.03, 0.30 ± 0.05, and 0.36 ± 0.04 for the 'plus', the 'minus', and the 'id' outcome, respectively. This is in good agreement with the expected value of $\frac{1}{3}$ for each outcome. An average of the output fidelities achieved over all input states and all rotations performed yields a value of $(92 \pm 4)\%$, demonstrating the high quality of our single-qubit quantum logic gates using a photonic AKLT state. A detailed list of all results can be found in the Supplementary Information of our published work [175].

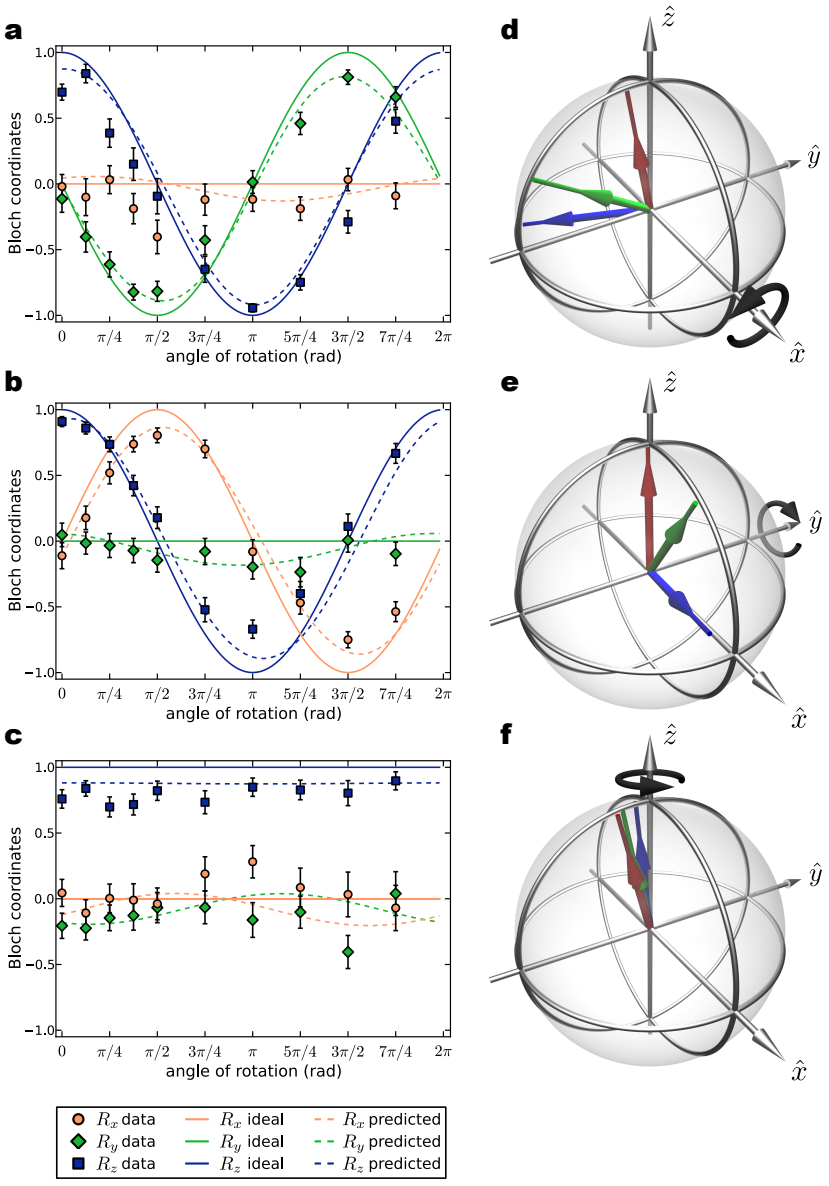

Figure 5.4: **Measurement results for single-qubit rotations.**. (a)-(c) show the coordinates of the Bloch vectors of the reconstructed output density matrices for rotations of a logical input state $|H\rangle$ around the $\hat{x}$, $\hat{y}$ and $\hat{z}$ axes, respectively. Note that the results shown are for the 'plus' outcome of the qutrit measurement, and that we have applied the necessary Pauli corrections to the reconstructed density matrices for all plots shown in the figure. Error bars are standard deviations calculated from Monte-Carlo simulations. Solid and dashed lines indicate the theoretical expectations given the ideal AKLT state and the tomographically-reconstruced AKLT state (see Figure 5.3), respectively. For the rotation angles 0, $\frac{\pi}{4}$, and $\frac{\pi}{2}$, panels (d)-(f) show the Bloch vectors of the measured (and Pauli corrected) density matrices corresponding to the Bloch coordinates shown in (a)-(c).

gate fidelities for logical input $\|H\rangle$						
outcomes	R_x		R_y		R_z	
	ρ_{th}	ρ_{exp}	ρ_{th}	ρ_{exp}	ρ_{th}	ρ_{exp}
plus	0.91 ± 0.04	0.96 ± 0.02	0.90 ± 0.05	0.98 ± 0.02	0.90 ± 0.03	0.96 ± 0.02
minus	0.93 ± 0.03	0.95 ± 0.03	0.91 ± 0.03	0.98 ± 0.01	0.92 ± 0.04	0.96 ± 0.02
id	0.90 ± 0.03	0.97 ± 0.02	0.93 ± 0.02	0.993 ± 0.006	0.97 ± 0.02	0.98 ± 0.02
gate fidelities averaged over all input states						
outcomes	R_x		R_y		R_z	
	ρ_{th}	ρ_{exp}	ρ_{th}	ρ_{exp}	ρ_{th}	ρ_{exp}
all	0.92 ± 0.04	0.96 ± 0.02	0.91 ± 0.04	0.97 ± 0.01	0.92 ± 0.04	0.96 ± 0.02

Table 5.4: **Single-qubit logic gate fidelities.** We compare the experimentally determined output density matrices with the ones expected, on the one hand, given an ideal AKLT state, ρ_{th}, and, on the other hand, given the AKLT state measured in our setup, ρ_{exp}. The upper part of the table shows the fidelities for a logical input state $|H\rangle$. For the 'plus' and 'minus' outcomes the fidelities are averaged over all rotation angles, for the 'id' outcome we performed one measurement per rotation axis. The lower part shows the corresponding fidelities averaged over all logical input states prepared (see text) and over all three qutrit measurement outcomes.

5.5 Conclusion

We have experimentally demonstrated a one-way quantum-computation scheme harnessing a novel resource, the AKLT state, and used it to implement a circuit realising single-qubit rotations around any coordinate axis. Quantum computation using AKLT instead of cluster states promises to combine the inherent advantages of the one-way model with resources that occur naturally in physical systems. Our scheme for creating AKLT states uses entangled states and linear optics similar in requirements to optical implementations using cluster states [155]. In contrast to some other optical implementations of quantum

logic gates for one-way quantum computation [53, 54], our scheme does not require phase stability and achieves significantly higher experimental fidelities. Our implementation of a valence-bond-solid state is a realisation of a projected entangled pair state [165]. Such states offer a promising framework for understanding the properties of entangled states that make them useful computational resources [160, 161, 162, 164]. Generalisations of the presented approach might allow to simulate other classes of alternative resource states with linear optics and to study their potential for quantum computing. Future challenges will be to find efficient methods of coupling quantum wires, to study solid-state compounds with ground states that can be used as computational resources, and to implement techniques to address such systems on a single-particle level. Ideally, this and related research will lead to implementations in solid-state architectures, allowing to tap the power of one-way quantum computation while taking full advantage of the appealing characteristics of novel resource states like AKLT.

Appendix B

QST of AKLT states

All measured counts correspond to four-fold coincidence detection events between one detector in each of the two qubit analyzers and the two detectors D_1 and D_2 in the qutrit analyzer (see Fig. 5.2). Table 5.5 lists the four-fold coincidence counts measured for all tomographical settings. For each setting of the analyzer waveplates we integrated over 60 s. Because we monitored both outputs in each of the two qubit analyzers and averaged over any unbalance between the two analyzer outputs, we have to measure 4 combinations of settings per projective measurement. This results in 240 s overall measurement time per projective measurement. In order to reduce the effect of slow drifts in the setup, we performed the full set of measurements twice, in each case randomly ordering the settings, resulting in a measurement time of 480 s per setting in Table 5.5.

		$\|\mathbf{0}\rangle$	$\|\mathbf{1}\rangle$	$\|\mathbf{2}\rangle$	$\frac{\|\mathbf{0}\rangle+\|\mathbf{1}\rangle}{\sqrt{2}}$	$\frac{\|\mathbf{0}\rangle-\|\mathbf{1}\rangle}{\sqrt{2}}$	$\frac{\|\mathbf{1}\rangle+\|\mathbf{2}\rangle}{\sqrt{2}}$	$\frac{\|\mathbf{1}\rangle-\|\mathbf{2}\rangle}{\sqrt{2}}$	$\frac{\|\mathbf{2}\rangle+\|\mathbf{0}\rangle}{\sqrt{2}}$	$\frac{\|\mathbf{2}\rangle-\|\mathbf{0}\rangle}{\sqrt{2}}$	$\frac{\|\mathbf{0}\rangle+i\|\mathbf{1}\rangle}{\sqrt{2}}$	$\frac{\|\mathbf{0}\rangle-i\|\mathbf{1}\rangle}{\sqrt{2}}$	$\frac{\|\mathbf{1}\rangle+i\|\mathbf{2}\rangle}{\sqrt{2}}$	$\frac{\|\mathbf{1}\rangle-i\|\mathbf{2}\rangle}{\sqrt{2}}$	$\frac{\|\mathbf{2}\rangle+i\|\mathbf{0}\rangle}{\sqrt{2}}$	$\frac{\|\mathbf{2}\rangle-i\|\mathbf{0}\rangle}{\sqrt{2}}$
$\|H\rangle$	$\|H\rangle$	3	8	595	7	7	239	191	158	128	7	10	181	198	154	153
	$\|V\rangle$	27	195	27	132	107	110	151	26	22	141	113	147	110	18	22
	$\|+\rangle$	8	80	327	63	68	26	296	90	86	75	57	171	176	100	93
	$\|-\rangle$	9	120	321	82	74	384	24	88	67	101	78	212	160	81	86
	$\|R\rangle$	12	90	251	78	61	171	158	95	69	80	61	17	306	109	71
	$\|L\rangle$	10	111	297	72	62	165	170	62	110	84	74	366	22	88	101
$\|V\rangle$	$\|H\rangle$	17	127	17	86	78	77	126	14	12	65	98	71	80	12	11
	$\|V\rangle$	539	3	0	141	202	5	4	153	145	177	154	3	4	128	141
	$\|+\rangle$	256	79	8	9	277	43	53	83	77	146	150	54	44	60	76
	$\|-\rangle$	317	68	4	204	22	45	52	102	66	166	152	34	53	93	46
	$\|R\rangle$	329	61	5	140	129	34	57	62	87	23	218	46	48	90	89
	$\|L\rangle$	299	71	8	113	122	45	52	82	61	239	19	62	41	84	59
$\|+\rangle$	$\|H\rangle$	5	68	328	46	40	30	238	58	85	31	58	113	160	58	85
	$\|V\rangle$	283	108	11	13	319	55	96	80	43	156	160	70	67	70	61
	$\|+\rangle$	127	173	193	18	231	5	292	117	21	138	162	144	155	69	120
	$\|-\rangle$	141	34	168	34	85	84	42	6	140	79	52	52	56	71	83
	$\|R\rangle$	126	85	139	23	171	51	156	74	84	52	184	21	192	14	151
	$\|L\rangle$	122	88	205	27	180	41	162	75	84	160	49	166	35	149	20
$\|-\rangle$	$\|H\rangle$	8	64	320	80	54	282	23	67	66	52	68	149	151	66	79
	$\|V\rangle$	315	87	15	303	16	67	43	61	99	198	147	77	57	80	101
	$\|+\rangle$	154	18	173	67	50	54	56	14	136	67	49	68	58	66	95
	$\|-\rangle$	166	174	169	273	8	286	15	167	14	181	159	139	130	75	89
	$\|R\rangle$	189	87	148	166	23	171	26	80	93	56	159	30	164	157	11
	$\|L\rangle$	154	89	167	152	26	179	32	79	92	196	39	204	45	20	125
$\|R\rangle$	$\|H\rangle$	10	58	270	41	42	167	139	77	84	39	45	34	300	96	80
	$\|V\rangle$	298	85	5	161	119	59	71	98	68	19	239	76	65	73	60
	$\|+\rangle$	116	68	169	32	140	26	181	67	99	12	153	52	201	9	127
	$\|-\rangle$	159	93	140	161	57	182	34	94	71	24	192	55	168	182	8
	$\|R\rangle$	135	126	183	172	128	156	149	12	137	8	255	15	296	87	89
	$\|L\rangle$	116	22	192	57	46	93	68	162	18	35	66	96	62	57	113
$\|L\rangle$	$\|H\rangle$	9	63	229	60	37	142	134	97	66	56	53	267	24	47	71
	$\|V\rangle$	340	73	6	165	183	58	67	84	86	329	20	86	45	99	63
	$\|+\rangle$	144	85	167	36	194	36	214	100	72	182	46	191	37	143	13
	$\|-\rangle$	195	101	128	167	49	139	30	97	80	221	23	172	37	20	148
	$\|R\rangle$	180	13	142	61	75	57	71	166	8	100	43	45	62	68	93
	$\|L\rangle$	133	152	172	149	124	150	163	10	131	271	14	306	15	82	82

Table 5.5: **Table of tomography results.** We performed a tomographically-overcomplete set of measurements on our qubit-qutrit-qubit state. The states in the first column indicate the measurement settings for the first qubit, the state in the second column indicate the settings for the other qubit, and the states in the top row denote the qutrit measurement settings. All counts given are raw four-fold coincidence events integrated over 480s.

Part II

Single-Photon Waveform Manipulation

Chapter 6

Spectral compression of single photons with chirped-pulse upconversion

Most of the material in this Chapter is published[1] in the following:

Reference: J. Lavoie, J. M. Donohue, L. G. Wright, A. Fedrizzi and K. J. Resch, Spectral compression of single photons, *Nature Photonics* **7**, 363-366 (2013)

Contributions: A.F. and K.J.R. conceived the idea for the study. K.J.R., A.F. and I designed the experiment. I performed the experiments, analysed the data and wrote the first draft of the paper. J.M.D. and L.G.W. contributed to building the experimental setup and in taking data. All authors contributed to writing the manuscript.

[1] No copyrights from the journal is required to include the article (all or part) in this thesis.

6.1 Introduction

Coherent photonic interfaces are paramount for future quantum technologies. In quantum networks [176] for example, photon pairs at 1550 nm—optimum for low-loss transmission—distribute entanglement between network nodes consisting of quantum memories. SPDC sources are widespread for producing entangled photon pairs [41], and typically yield spectral bandwidths of 300 GHz. The most efficient quantum memories [177] however typically operate in the near visible wavelength regime near 800 nm with narrower bandwidths on the order of 10 MHz. This dilemma has partly been addressed through centre-frequency conversion [178] of single photons using nonlinear optical processes in crystals [179, 180, 181, 182, 72], photonic crystal fibres [183] and Rubidium vapor [184]. This conversion process can be highly efficient [181, 185] and can conserve quantum coherence [178, 180, 184, 182, 72, 183]. Some quantum memory schemes [186] offer very limited control over the spectrum of reemitted photons through varying parameters of the control laser [187].

Nonlinear optics has much more potential for manipulating and controlling the spectrum of single photons. Sum-frequency generation (SFG) is a nonlinear optical process in which a pair of optical fields of frequencies ν_1 and ν_2 create a third field with frequency $\nu_3 = \nu_1 + \nu_2$ [55]. When the driving fields are transform-limited laser pulses and the acceptance bandwidth of the material is sufficiently large, the bandwidth of the SFG is larger than that of the input fields. Repeating this process with shaped, rather than transform-limited pulses, can drastically alter the spectrum of the SFG signal. Specifically, oppositely-chirped laser pulses in SFG and equally-chirped laser pulses in difference-frequency generation lead to narrow output spectra [188, 189, 190]. It was recently proposed theoretically to employ SFG between a chirped classical pulse and a single photon to enable compression of the photon pulse in *time* [73]; interaction of a short laser pulse with the emission from a quantum dot achieves [72] similar results through temporal gating.

In this chapter, we exploit pulse chirping of a classical laser and a single photon to compress the bandwidth of the single photon, from 1740 GHz to 43 GHz, which is nearing the bandwidth regime of some quantum memories [191, 192]. We also demonstrate tunability over a range 70 times that bandwidth. When combined with shaped pulses, nonlinear

optics in the quantum regime promises a new level of control over single photons [73, 193].

6.2 Theory

Our scheme, depicted in Fig. 6.1a, uses SFG between a chirped single photon and an oppositely chirped intense laser pulse. The photon is chirped such that its frequency, centered at $\nu_{0,P}$, increases in time, while the strong pulse centred at $\nu_{0,L}$ is *anti*-chirped such that its frequency decreases linearly in time. When the photon and pulse arrive at the crystal simultaneously, a red-shifted frequency component $(\nu_{0,P} - \delta)$ will meet a blue-shifted component $(\nu_{0,L} + \delta)$ with the same detuning δ and as a consequence, all frequency components will sum to a narrow frequency centered on $\nu_{0,SFG} = \nu_{0,P} + \nu_{0,L}$.

A light pulse can be described by the frequency-dependent electric field, $E(\nu) = U(\nu)e^{i\phi(\nu)}$, where $U(\nu)$ and $\phi(\nu)$ define the amplitude and phase, respectively. A linear chirp results when a transform-limited pulse is subject to a quadratic phase, $\phi(\nu) \sim \frac{1}{2}\beta_2(\nu - \nu_0)^2$, with ν_0 the central frequency and β_2 is the second order dispersion term. A chirp increases the pulse duration and causes its instantaneous frequency to vary linearly in time $\nu(t) = \frac{d\phi(t)}{dt} = \nu_0 \pm \frac{2\pi}{\beta_2}t$. When the chirped single photon (P) and anti-chirped strong laser pulse (L) have a relative time delay at the nonlinear crystal, τ, the expected upconverted frequency is

$$\nu_{0,SFG}(\tau) = \nu_{0,P} + \nu_{0,L} + \frac{2\pi}{|\beta_2|}\tau, \tag{6.1}$$

where we assume the pulses have equal and opposite chirp, $\pm|\beta_2|$. We consider the large chirp limit, where each pulse is stretched many times its transform-limited duration, i.e., $|\beta_2|^2\Delta\nu^4 \gg 1$, where $\Delta\nu$ is the width (FWHM) of the spectral intensity distribution. We show in Appendix C (from Eq. 6.20) that the expected intensity bandwidth (FWHM) of the upconverted single photon is

$$\Delta\nu_{SFG}^{TH} \approx \frac{4\ln 2}{|\beta_2|}\sqrt{\frac{1}{\Delta\nu_P^2} + \frac{1}{\Delta\nu_L^2}}, \tag{6.2}$$

with $\Delta\nu_L$ and $\Delta\nu_P$ the bandwidths of the strong laser pulse and single photon, respectively. Our technique thus compresses the spectral bandwidth of the photon by a factor inversely

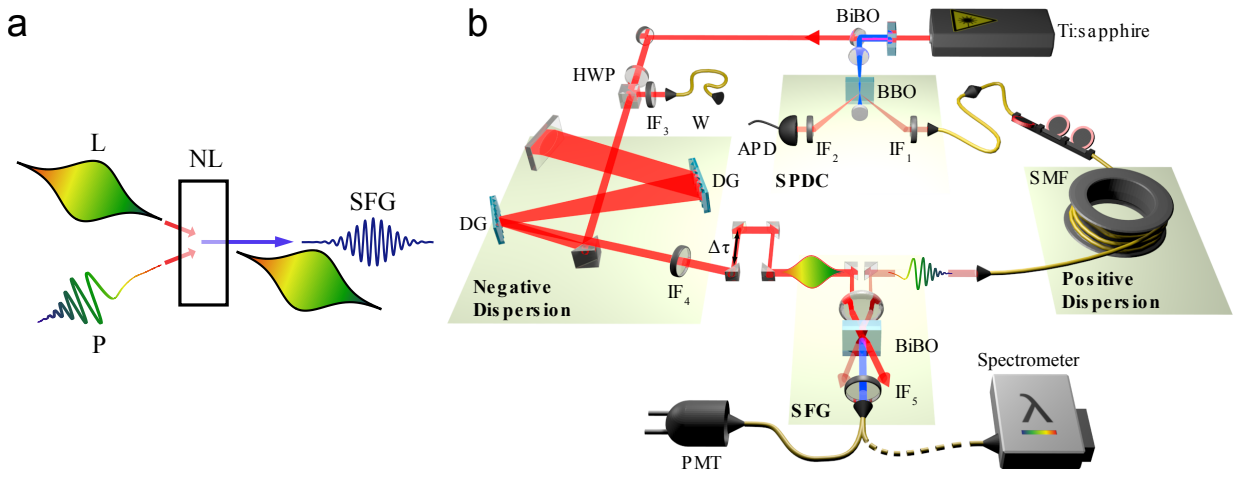

Figure 6.1: **Single-photon bandwidth compression scheme. a**, A broad-bandwidth single photon (P) with a linear frequency chirp is converted into a narrow-band photon of a higher frequency via sum-frequency generation (SFG) with a strong laser pulse (L) of opposite chirp, in a nonlinear crystal (NL). **b**, Experimental setup. Photon P is generated via SPDC in a BBO crystal (Type-I, 1 mm) and sent through 34 m of optical fiber (SMF) to introduce a linear chirp via group velocity dispersion [77]. The strong laser pulse is anti-chirped after a double-pass between two diffraction gratings (DG, 1200 lines/mm) [77]. The spectrally narrowed photon is generated in a 1 mm thick BiBO crystal and detected with a photomultiplier tube (PMT) or sent to a spectrometer. For alignment purposes, the single photons can be substituted by a weak coherent state (W), split off from the laser beam using a half-wave plate and a polarizing beam-splitter.

proportional to the chirp parameter $|\beta_2|$. By adjusting the delay between the pulses, the central frequency $\nu_{0,SFG}(\tau)$ of the upconverted photons can be tuned over some frequency range, approximately $\sqrt{\Delta\nu_P^2 + \Delta\nu_L^2}$ (see Section D1, Appendix C), limited by the spectra of the initial single photon and laser pulse[2].

6.3 Experiment

The experimental setup is shown in Fig. 6.1b. Our laser (Spectra Physics Tsunami HP) has a 790 nm central wavelength, 10.5 nm spectral bandwidth (FWHM), 80 MHz repetition rate, and 2.5 W average power. The laser repetition rate is stabilized by a feedback system (Lok-to-clock) which is important for the present experiment (see Appendix C, Section C3). Second-harmonic generation in a 2 mm thick BiBO crystal yields a beam of 830 mW, centred at 394.2 nm with 1.3 nm bandwidth, which generates the broadband and non-collinear photon pairs. In the signal-photon path, the interference filter IF_1 shown in Fig 6.1b, with a nominal bandwidth of 5 nm (FWHM) centered around 811 nm, is inserted to keep its central frequency separated from that of the laser beam at 790 nm, to separate the spectrum of the second-harmonic background from our signal. Due to the energy conservation of SPDC, an interference filter, IF_2, centered around 770 nm and nominal bandwidth of 3 nm is inserted in the path of the idler-photon.

We first optimize the setup with a weak coherent state (W), split off from the strong laser pulse using a HWP and PBS. An interference filter (IF_3) is inserted in its path and the transmitted spectrum has a measured bandwidth of 3.85 ± 0.03 nm ($\Delta\nu_W = 1760 \pm 10$ GHz) centered at 810.49 ± 0.01 nm, closely matched to IF_1.

The strong laser pulse was re-collimated with a set of lenses before being "anti-chirped" in a grating-based setup [78], with normal separation of 38 cm between the gratings, carefully adjusted to minimize the spectral width of the upconverted light. The bandpass filter IF_4 highly attenuates any power in the tail of the laser spectrum above 800 nm to further suppress second-harmonic background. After the filter, the pulse has a measured bandwidth of 9.86 ± 0.05 nm ($\Delta\nu_L = 4770 \pm 20$ GHz) centered at 787.62 ± 0.02 nm. We

[2]Here we neglected phase mismatch that will further reduce the range if not compensated.

used an achromatic doublet with a 75 mm focal length in the upconversion setup, and the conversion efficiency was optimized by fine tuning the relative delay between the two inputs, the spatial overlap at the crystal, and the phase matching by angle tuning. A 14.5 nm bandpass filter IF_5 with central wavelength at 405 nm is placed in the SFG beam to reduce background.

The weak beam is finally replaced by the single photons, with the same optical path length. We used a spectrometer (Acton SP-2750A) with a 1200 lines/mm diffraction gratings blazed for 400 nm and entrance opening of 20 μm with a resolution of 60 GHz. We use the spectrograph, free-running mode with a back-illuminated CCD camera (PIXIS: 2048B).

6.4 Results

We first measure the spectrum of the signal photons at the source, after the interference filter IF_1, using a fiber-coupled spectrometer and find a width $\Delta\nu_P = 1740 \pm 50$ GHz (FWHM) centered around 811.11 ± 0.01 nm, see Fig. 6.2. The photons are then sent through an optical fiber with positive dispersion and superposed with the anti-chirped strong laser pulse at the nonlinear crystal for SFG.

The upconverted light is coupled into a single-mode fiber and sent to the spectrometer. As shown in Fig. 6.2, we observe significant spectral compression. The measured bandwidth is $\Delta\nu_M = 74 \pm 4$ GHz centered at 399.7 nm. Taking the resolution of our spectrometer into account, $\Delta\nu_R = 60 \pm 4$ GHz, the actual width of the upconverted photon after deconvolution is $\Delta\nu_{SFG}^{EXP} = \sqrt{\Delta\nu_M^2 - \Delta\nu_R^2} = 43 \pm 9$ GHz (see Appendix C, Section D2, for more details). This agrees closely with theory, $\Delta\nu_{SFG}^{TH} = 32.9 \pm 0.9$ GHz from equation (6.2), using the expected chirp parameter $|\beta_2| = (51.6 \pm 0.6) \times 10^6$ fs^2 given by the geometry of our grating-based stretcher. We have therefore achieved a compression ratio of 40:1 in the single photon frequency bandwidth. Similar measurements were made after replacing the single photons by a weak coherent state (W), shown in Fig. 6.1b. The corresponding measured spectral width of the upconverted light was 67 ± 4 GHz, or 30 ± 12 GHz after deconvolution, showing similar performance with a classical chirped pulse with the same characteristics

as the signal photons.

Figure 6.2 also shows the spectrum predicted by theory which would result from upconversion of the signal photon using the same pump laser *without* any chirp. The conversion in this case actually *broadens* the spectral bandwidth of the original photon by a factor of 3, increasing the bandwidth gap between flying broadband photons and narrowband quantum memories, which further highlights the importance of our scheme.

The central wavelength of the narrowband upconverted photons can be tuned by controlling the relative delay, τ, between the photon and the laser pulse, see Eq. 6.1. The SFG spectrum was measured as a function of the delay of the single photon, with fitted central wavelengths shown in Fig. 6.3. The data shows that the wavelength depends linearly on the delay as expected. The linear fit gives a slope of -0.0640 ± 0.0005 nm/ps in good agreement with -0.0648 ± 0.0008 predicted from Eq. 6.1 and $|\beta_2| = (51.6 \pm 0.6) \times 10^6$ fs^2. If the weak coherent state is used instead of single photons, we observe the same behaviour in the spectrum of the upconverted light, and the data are also shown in Fig. 6.3. The lower SFG signal for single photons required longer integration times than for the coherent states; to reduce the effects of drift in experimental parameters all of the data in Fig. 6.3 was taken within a day. For the single photons, we focused on those delays demonstrating the widest possible tuning range. From the slope, we can extract the chirp parameter of $|\beta_2| = (52.4 \pm 0.4) \times 10^6$ fs^2, in agreement with expectations based on the parameters of the stretcher.

Photons from SPDC are created in pairs and are strongly correlated in time; we expect these correlations are preserved through spectral compression. We first measured coincidence counts between single photon detectors placed in the source as a function of a time delay between the counts. Figure 6.4a shows the coincidence counts versus delay, without background substraction. The peak around zero delay corresponds to a rate of 160,000 s^{-1}, within a 3 ns coincidence window. The histogram also contains side peaks from accidental coincidences with a separation of 12.5 ns matching the laser repetition rate. After propagating through the single-mode fibre, the signal photons are upconverted and detected with a single-photon counting photomultiplier (PMT). Figure 6.4b clearly shows that the coincidence rate observed at zero-delay between the upconverted and idler photons exceed the accidentals, preserving the strong timing correlation associated with

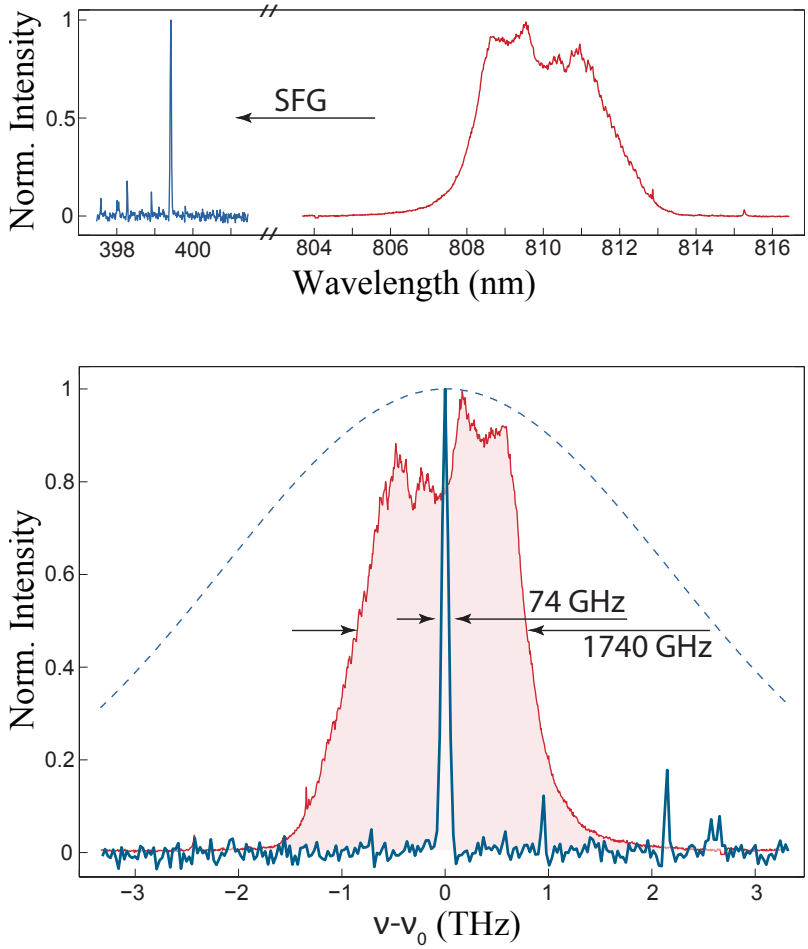

Figure 6.2: **Single-photon spectra in wavelength (top) and relative frequency (bottom)**. The signal photons at the source (shown in red) have an initial bandwidth of 1740 GHz centred at 811 nm after transmission through an interference filter. Once the quadratic phase is applied and the photons are upconverted, the photon bandwidth reduces to 74 ± 4 GHz centred at 399.70 nm (blue curve). The spectra are shown as normalised spectral intensities and for the upconverted signal case, correspond to the average of six consecutive scans of 20 minutes acquisition time. We subtracted background counts determined by a supplementary scan with the signal photon path blocked. The blue dashed curve shows the theoretical spectrum of photons upconverted without our chirping technique but otherwise identical conditions. The spectrometer resolution is 60 ± 4 GHz.

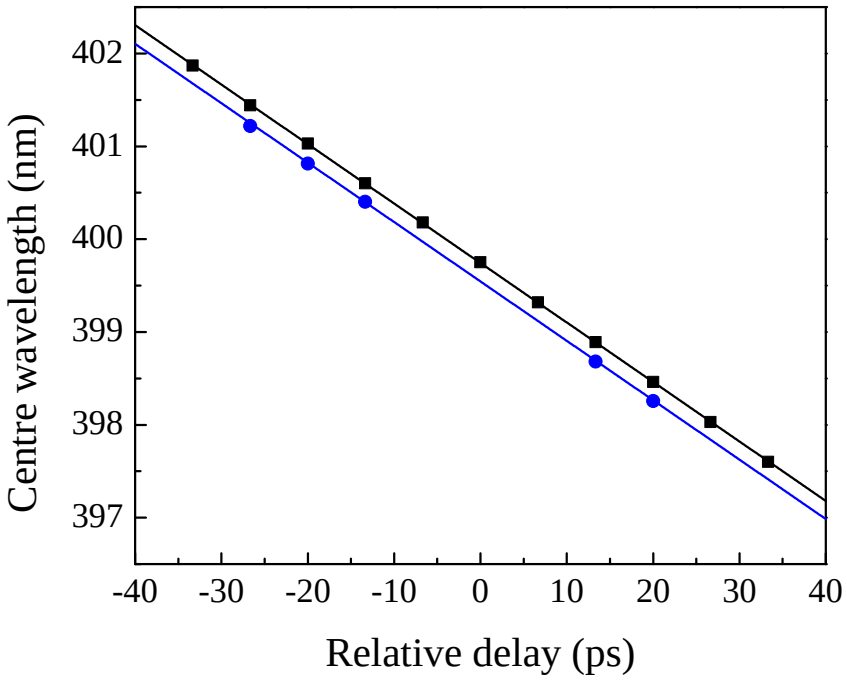

Figure 6.3: **Wavelength tunability**. The centre wavelength of the upconverted light can be tuned by controling the relative delay between the input pulses at the nonlinear crystal. The blue circles represent the centre wavelength of the upconverted single photon, covering a range of 3 nm. The upconverted light from the weak coherent state behaves the same way and is plotted with the black squares. The lines are linear fits yielding slopes of -0.0640 ± 0.0005 nm/ps and -0.0641 ± 0.0001 nm/ps for the single photons and the weak pulses, respectively. The vertical offset between the two curves (~ 0.2 nm) comes from a slight difference in the delay between the weak coherent state and the single photons at the crystal and a difference in their central wavelength. The error bars are smaller than the data points.

individual photon pairs. If we instead upconvert the weak coherent state, which shares the spectral and temporal properties of the signal photon, all observed peaks in Fig. 6.4c have the same height, as expected for a pulsed, but temporally uncorrelated source.

6.5 Conclusion

The efficiency of the upconversion process in our experiment is 0.06% with 300 mW of average power for the strong beam. Higher efficiencies could be achieved with the use of periodically poled crystals and higher pump powers [181, 185]. One doesn't require 100% conversion efficiency to achieve a net gain. Ignoring the shift in centre frequency, one has an advantage over a narrow bandwidth filter once the efficiency is greater than about $100\%/R$, where R is the ratio of the initial to final bandwidth, which in our case is 40, for an efficiency of just 2.5%. The amount of negative dispersion achievable limits the maximum compression; with realistic parameters [194] and our spectra, one could reach compression down to $\sim$1 GHz.

Future work will explore the case when the single photon is entangled with another. It is expected that polarisation entanglement could be preserved by employing polarisation-insensitive upconversion [182]. Our technique could serve as a coherent interface between time-bin and frequency encodings of quantum information due to the delay-dependent central frequency, allowing the conversion of time-bin entanglement to colour entanglement [195]. It also enables ultrafast timing measurements with slow detectors [41] by converting different pulse arrival times to different frequencies which could more easily be distinguished. With our experimental parameters, one could distinguish time bins with separation as short as 0.6 ps over a 40 ps range. Future work will investigate nonlinear interactions with more complex shaped pulses for manipulating single photons; for example, coherent superpositions of chirped pulses with different delays would allow ultrafast single-photon time-bin measurements. The application of shaped pulse nonlinear optics is a promising and unexplored regime at the quantum level.

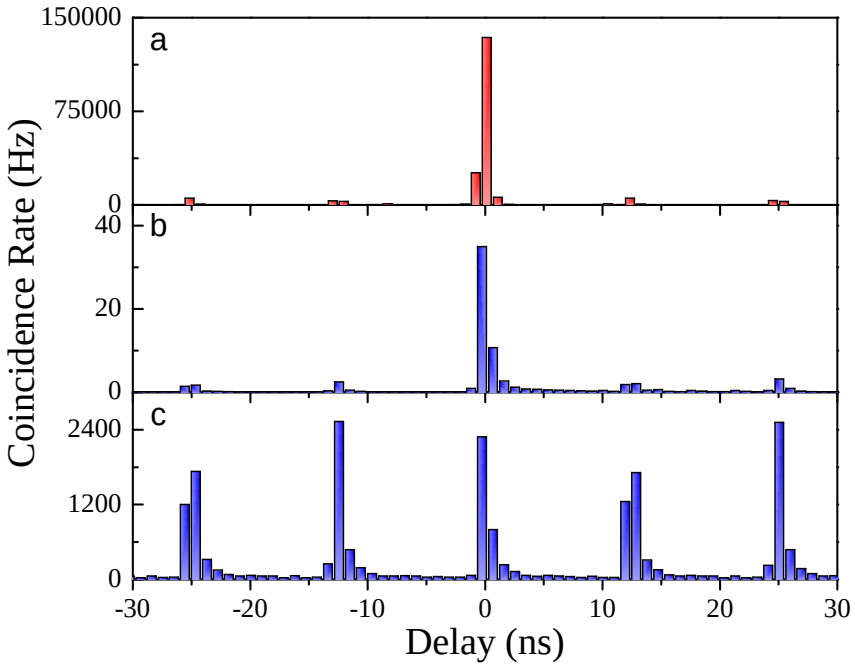

Figure 6.4: **Temporal correlations with the idler photon**. **a**, The signal and idler from SPDC are produced in pairs, strongly correlated in time with a total measured coincidence rate of $160,000$ s^{-1} around zero delay. **b**, The upconverted single photon maintains the strong timing correlation expected from individual photon pairs, and a coincidence rate of 50 s^{-1} is detected. **c**, If the weak coherent state is upconverted instead, the histogram shows equal height peaks as expected for pulsed, but uncorrelated events. For each histogram, the optical path length difference with the idler is accounted for in post-processing and the abscissa is a variable electronic delay. An additional electronic delay box, with an observed asymmetric temporal jitter, was used on the idler side only, causing the asymmetry in b) and c). Error bars, 1 s.d. too small at this scale.

Appendix C

C1. Theory

We model the creation of upconverted single photons through the interaction Hamiltonian, H, of a three-wave $\chi^{(2)}$ non-linear process. We assume that frequency bandwidths are narrow and perfect phasematching ($\vec{k}_P + \vec{k}_L - \vec{k}_{SFG} = 0$) is achieved ($P$= single photon, L= Laser). Ignoring constants, our Hamiltonian is given by

$$H \propto \iiint \mathrm{d}\nu_1 \mathrm{d}\nu_2 \mathrm{d}\nu_3 \hat{a}^{(P)}_{\nu_1} \hat{a}^{(L)}_{\nu_2} \hat{a}^{\dagger(SFG)}_{\nu_3} \delta(\nu_1 + \nu_2 - \nu_3) + h.c. \tag{6.3}$$

and describes the process in which two photons at frequencies ν_1 and ν_2 are absorbed by a dielectric medium and give rise to a new photon at the sum-frequency $\nu_3 = \nu_1 + \nu_2$.

Our initial three-mode state $|\psi_0\rangle$ contains a single photon

$$|1\rangle_P = \int d\nu_1 f_P(\nu_1) e^{i\phi_P(\nu_1)} |1_{\nu_1}\rangle, \tag{6.4}$$

a large amplitude coherent state

$$|\alpha\rangle_L = \int d\nu_2 f_L(\nu_2) e^{i\phi_L(\nu_2)} |\alpha_{\nu_2}\rangle \tag{6.5}$$

and an output signal, initially vacuum $|0\rangle_{SFG}$. The amplitudes $f(\nu_i)$ and phases $\phi(\nu_i)$ will be defined shortly.

We assumed no frequency correlations between the single photon P and an idler, a lossless and non dispersive medium, and an interaction length much longer than the optical wavelengths. The first nontrivial term in the initial state evolution is found to be

$$|\psi^{(2)}_f\rangle \propto \iint d\nu_3 d\nu_1 f_P(\nu_1) f_L(\nu_3 - \nu_1) e^{i(\phi_P(\nu_1) + \phi_L(\nu_3 - \nu_1))} |1_{\nu_3}\rangle. \tag{6.6}$$

From this expression, the electric field amplitude $E(\nu_3)$ is thus proportional to

$$E(\nu_3) \propto \int d\nu_1 f_P(\nu_1) f_L(\nu_3 - \nu_1) e^{i(\phi_P(\nu_1) + \phi_L(\nu_3 - \nu_1))}. \tag{6.7}$$

Notice that Eq. 6.7 represents the convolution of two input pulses, in frequency domain. This is analogous to the classical derivation of sum-frequency generation, for which the product of the fields in time leads to the convolution in frequency domain [55]. Thus, the same spectral properties are expected if both inputs are coherent states.

To analyse the field intensity $|E(\nu_3)|^2$ of the upconverted photons, we now specify the phases and amplitudes. For both the coherent state and single-photon, the frequency distribution of the field amplitude is assumed to be Gaussian,

$$f(\nu_i) \propto \exp\left[-\frac{(\nu_i - \nu_{0,i})^2}{2\sigma_i^2}\right], \tag{6.8}$$

with central frequency $\nu_{0,i}$ and spectral variance σ_i^2. The phase terms, $\phi(\nu_i)$, are given by

$$\phi(\nu_i) = \beta_0 + \beta_1(\nu_i - \nu_0) + \frac{\beta_2}{2!}(\nu_i - \nu_0)^2 + \dots. \tag{6.9}$$

We choose this form to take into account the propagation of the initial Gaussian pulse in a uniform dispersive medium and neglect the higher order terms in the Taylor expansion. This medium corresponds to an optical fiber for the photons, and a grating-based stretcher for the coherent states. β_0 is a constant phase shift, β_1 describes a time delay and the most important term, β_2, is the second-order dispersion that broadens the pulses temporally, and causes a linear chirp of the frequencies.

Inserting Eq. 6.8 and 6.9 into Eq. 6.7 and after integration, we find the SFG field intensity

$$|E(\nu_3)|^2 \propto \exp\left[-\frac{\nu_3^2\sigma_1^2 + \left(\nu_3^2 + \left(\left(\beta_{1,P} - \beta_{1,L}\right) + \beta_{2,P}\ \nu_3\right)^2 \sigma_1^4\right)\sigma_2^2 + \left(-\left(\beta_{1,P} - \beta_{1,L}\right) + \beta_{2,L}\ \nu_3\right)^2 \sigma_1^2\sigma_2^4}{2\sigma_1^2\sigma_2^2 + \sigma_2^4 + \sigma_1^4\left(1 + \left(\beta_{2,L} + \beta_{2,P}\right)^2 \sigma_2^4\right)}\right]. \tag{6.10}$$

To simplify this expression, we have set $\nu_{0,i} \to 0$; we are mainly interested in the spectral *width* and the relative frequency *shift* of the SFG around $\nu_{0,P} + \nu_{0,L}$ and keep the expression normalised.

We make two more simplifications. i) Define a relative time delay between the input pulses by replacing $(\beta_{1,P} - \beta_{1,L}) \to 2\pi\tau$. ii) It is physically motivated to set $\beta_{2,L} \to |\beta_2|$ and $\beta_{2,P} \to -|\beta_2|$ since we made sure the opposite second order dispersions were well balanced during the experiment. Equation 6.10 simplifies to

$$|E(\nu_3)|^2 \propto \exp\left[-\frac{\nu_3^2 + \sigma_1^2\sigma_2^2\left(|\beta_2|\nu_3 + 2\pi\tau\right)^2}{\sigma_1^2 + \sigma_2^2}\right]. \tag{6.11}$$

The exponent is a quadratic expression of the form $ax^2 + bx + c$ and can be transformed into $a(x+d)^2 + e$, with $d = \frac{b}{2a}$ and $e = c - \frac{b^2}{4a}$. This allow us to express the spectral intensity as

$$|E(\nu_3)|^2 \propto e^{-\frac{(\nu_3 - \delta\nu(\tau))^2}{\sigma_3^2}} e^{-\frac{\tau^2}{\xi^2}} \tag{6.12}$$

with a delay dependent frequency shift given by

$$\delta\nu(\tau) = \frac{4\pi|\beta_2|\sigma_1^2\sigma_2^2}{2(1 + |\beta_2|^2\sigma_1^2\sigma_2^2)}\tau, \tag{6.13}$$

a spectral variance

$$\sigma_3^2 = \frac{(\sigma_1^2 + \sigma_2^2)}{1 + |\beta_2|^2\sigma_1^2\sigma_2^2}, \tag{6.14}$$

and a correlation range (or delay range)

$$\xi^2 = \frac{(\sigma_1^2 + \sigma_2^2)(1 + |\beta_2|^2\sigma_1^2\sigma_2^2)}{4\pi^2\sigma_1^2\sigma_2^2} \tag{6.15}$$

which bounds the tunable SFG range as the delay τ varies. We want to compare the cases i) without and ii) with dispersion $|\beta_2|$.

i) No dispersion [ND], $|\beta_2| \to 0$

If we neglect the second order dispersion, i.e., no chirp is applied to the pulses, Eqs. (6.13–6.15) become

$$\delta\nu(\tau)[\text{ND}] \;\to\; 0 \tag{6.16}$$

$$\sigma_3^2[\text{ND}] \;\to\; \sigma_1^2 + \sigma_2^2 \tag{6.17}$$

$$\xi^2[\text{ND}] \;\to\; \frac{1}{(2\pi)^2}\left(\frac{1}{\sigma_1^2} + \frac{1}{\sigma_2^2}\right). \tag{6.18}$$

We retrieve familiar expressions of the autocorrelation signal.

ii) With dispersion, and $|\beta_2|^2\sigma_1^2\sigma_2^2 \gg 1$

In this case and with the "large chirp" approximation, $|\beta_2|^2\sigma_1^2\sigma_2^2 \gg 1$, the parameters in Eq. 6.12 are

$$\delta\nu(\tau) \rightarrow \frac{2\pi}{|\beta_2|}\tau \tag{6.19}$$

$$\sigma_3^2 \rightarrow \frac{1}{|\beta_2|^2}\left(\frac{1}{\sigma_1^2}+\frac{1}{\sigma_2^2}\right) \tag{6.20}$$

$$\xi^2 \rightarrow \left(\frac{|\beta_2|}{2\pi}\right)^2(\sigma_1^2+\sigma_2^2). \tag{6.21}$$

From Eq. 6.20, we see that for fixed spectral widths, the SFG width σ_3 is inversely proportional to the dispersion (chirp) amplitude $|\beta_2|$. Equation 6.19 gives us the rate of frequency shift versus delay, $\frac{\Delta\delta\nu}{\Delta\tau} = \frac{2\pi}{|\beta_2|}$ and we also find that $(\Delta\tau)^2 \equiv \xi^2 = \left(\frac{|\beta_2|}{2\pi}\right)^2 \Delta\delta\nu$. Inserting the latter into Eq. 6.21 gives $\left(\frac{|\beta_2|}{2\pi}\right)^2 \Delta\delta\nu = \left(\frac{|\beta_2|}{2\pi}\right)^2(\sigma_1^2+\sigma_2^2)$. The frequency is thus restricted to a range equal to the variance $\sigma_3^2(\mathrm{ND})$, Eq. 6.14, when no dispersions are involved.

Figure 6.5 summarizes the results of this section; FWHM (Δx) and variance (σ^2) of a variable x are related by a constant, such that $\Delta x(\mathrm{FWHM}) = 2\sqrt{\ln 2}\sqrt{\sigma^2}$.

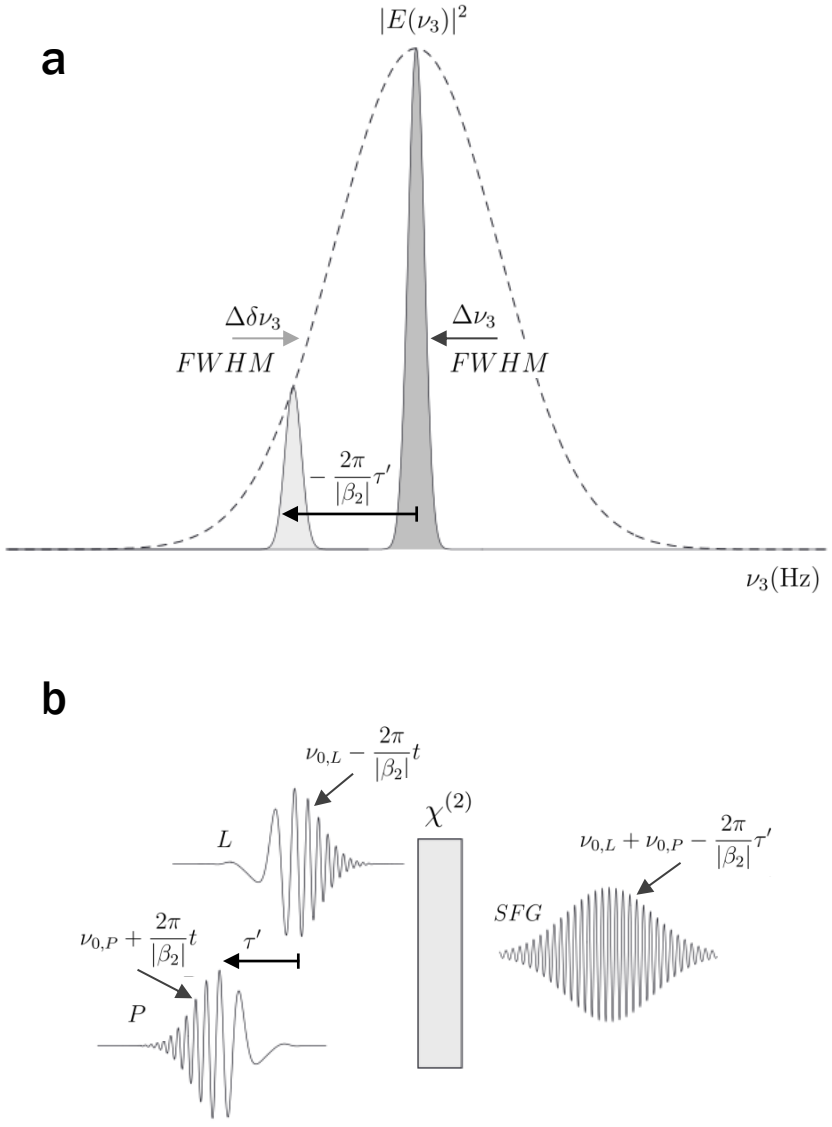

Figure 6.5: **Predicted bandwidth compression and tunability of a single photon.** **a**, SFG spectral intensity $|E(\nu_3)|^2$ is plotted in function of its frequency ν_3. The initial center frequency is around $\nu_{0,L} + \nu_{0,P}$ with a FWHM $\Delta\nu_3 = 2\sqrt{\ln 2}\sqrt{\sigma_3^2}$. A delay τ' between the input pulses, shown in **b**, leads to a frequency shift of $-\frac{2\pi}{|\beta_2|}\tau'$. Because of the limited physical overlap of the pulses, this shift is bounded and has a FWHM of $\Delta\delta\nu_3 = 2\sqrt{\ln 2}\sqrt{\sigma_3^2(\mathrm{ND})}$ around the center frequency.

C2. Error estimation for the spectral widths

We estimated the uncertainties in the bandwidth of the SFG for the single photon and weak coherent state in the following way. We characterized the resolution of our spectrometer using a narrow-band diode laser (Toptica Bluemode) with 5 MHz of spectral width centered at a wavelength 404 nm. Using a fit to a Gaussian function, we measure the spectrometer resolution to be (0.033 ± 0.002) nm at the diode laser wavelength, where the uncertainty is the estimated error on the fit. We measured the bandwidth for several input intensities and found that the measured bandwidth had some intensity dependence at low power; this is the dominant source of error in the bandwidth. Using the expression $\Delta\nu = \frac{c}{\lambda^2}\Delta\lambda$ we determine the resolution to be $\Delta\nu_R = (60 \pm 4)$ GHz.

We measured the spectrum of the upconverted single photons 6 times, fit each to a Gaussian function, and found the width, 74 ± 1 GHz (see Fig. 6.2), where the uncertainty is the standard deviation in the widths from the fits. To include the spectrometer resolution we add ± 4 GHz in quadrature to obtain the reported result, $\Delta\nu_M = 74 \pm 4$ GHz. To deconvolve the spectrometer resolution from this result for comparison with theory, we assume Gaussian spectra and use the relation, $\Delta\nu_{Real} = \sqrt{\Delta\nu_M^2 - \Delta\nu_R^2} = 43$ GHz and Gaussian error propagation gives an uncertainty of 9 GHz.

We apply the same method for the weak coherent state. The measured width was fitted using one spectrum only, with a value of 67.2 ± 0.4 GHz. Including the spectrometer resolution gives $\Delta\nu_M^{WCS} = 67 \pm 4$ GHz, and deconvolution yields $\Delta\nu_{Real}^{WCS} = 30 \pm 12$ GHz.

C3. Laser repetition rate stabilization

Our experiment requires that two short pulses of light, one from the single photon and the other from the strong laser, overlap in space and time at the nonlinear up-conversion crystal. Temporal jitter between the pulses will lead to broadening of the second harmonic spectrum since the central frequency of the light is dependent on their relative delay. In many scenarios, perfectly time-synchronized pulses are created by splitting a single laser pulse on a beamsplitter. This is common to many types of interferometry or pump-probe techniques. In these cases, the signal is insensitive to changes in the repetition rate of the

laser and one need only consider small changes in the relative path lengths. However, this is not the case here, as the single photon (or weak coherent state) and strong classical laser beam originate from different laser pulses.

Our experimental setup is shown in Fig. 6.6. The optical delay for the down-conversion path is t_1 measured from the beamsplitter (BS_1) through the down-conversion to the end of the 2 m fiber. This delay was carefully matched to that experienced by the weak coherent state which we also label as t_1. The additional delay t_1' corresponds to the one taken by either the single photon or the weak coherent state through the 32 m of single mode fiber, up to the nonlinear crystal. The optical delay for the strong classical pulse is t_2 measured from the same beamsplitter, through the grating-based stretcher and to the nonlinear crystal. The time delay between subsequent pulses is $1/R$, where R is the repetition rate of the laser, in our case 80 MHz. To this second path, we add the extra delay n/R to account for the fact that the light arriving at the nonlinear crystal from path 2 originated n pulses later than that from path 1. Thus, the timing difference, Δt is

$$\Delta t = t_2 + n/R - t_1 - t_1'. \tag{6.22}$$

Thus the relative time delay between either the single photon and the strong classical pulse or the weak coherent state and the strong classical pulse depends on both the repetition rate and the number of pulses separating them.

Experiment 1

We measured the spectral line of the sum-frequency generated from the weak coherent state and the strong laser pulse, as the repetition rate was manually detuned from 80 MHz. The results from our experiment are shown in Fig. 6.7. The data is well fit by a straight line with slope 0.1188 ± 0.0004 nm/kHz.

To find the expected frequency change for a given variation in the repetition rate, we start by finding the expected change in the time delay with respect to the repetition rate

$$\frac{d(\Delta t)}{dR} = -\frac{n}{R^2}. \tag{6.23}$$

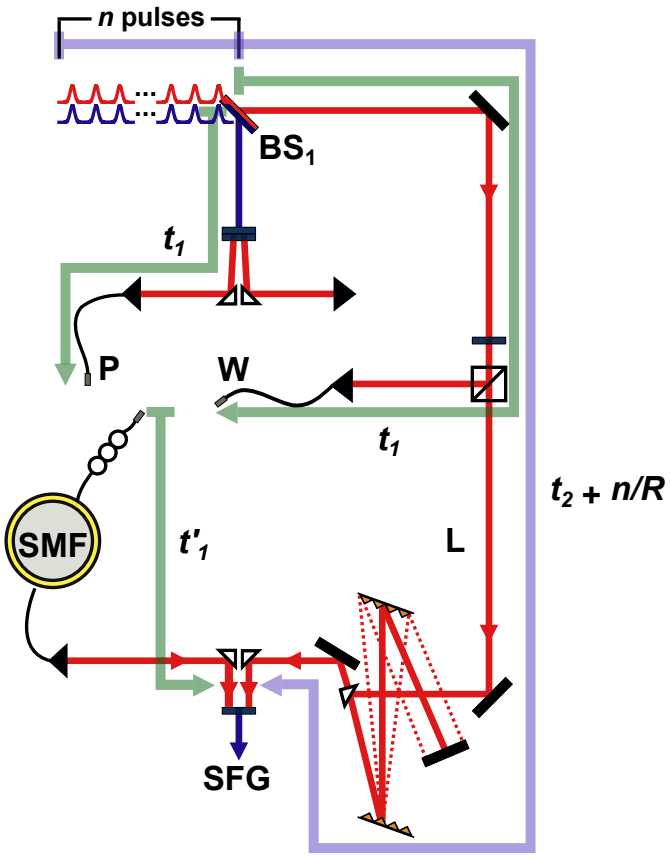

Figure 6.6: **Simplified version of the experimental setup.** The path length from the first pulse to the nonlinear crystal (SFG) has an optical delay of $t_1 + t_1'$: t_1 is the path length of the single photons including the path length of the first pulse from the beamsplitter (BS_1) to the SPDC crystal and t_1' includes the optical path length inside the long fiber and the free-space path to the upconversion crystal. This delay is equal to that experienced by the weak coherent state to the nonlinear crystal. The delay for the optical path from the beamsplitter to the upconversion crystal through the grating-based setup is t_2, but since the relevant pulse originates later than that which creates the down-converted photon, we have to add an additional contribution n/R where n is the number of pulses later and R is the repetition rate of the laser.

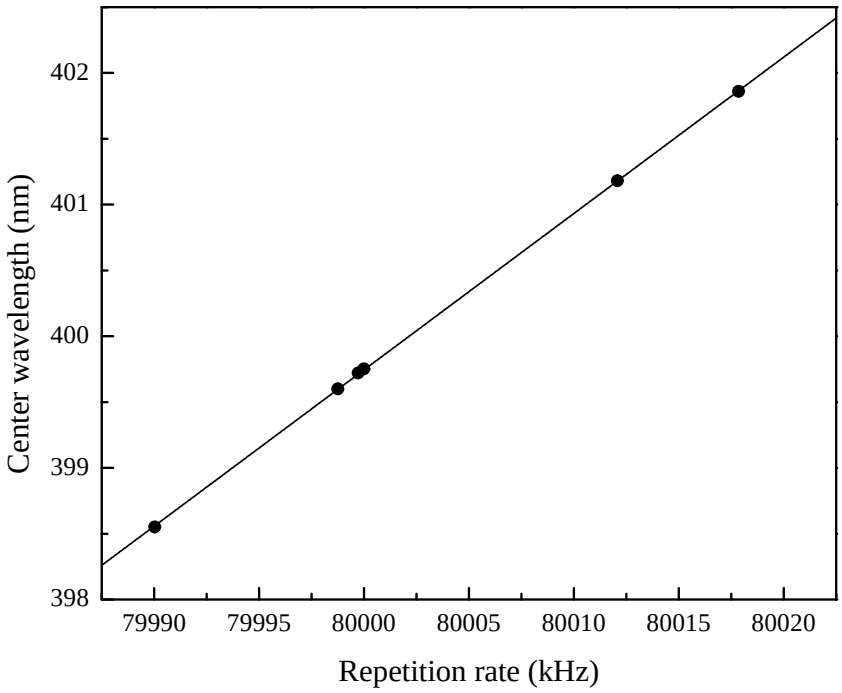

Figure 6.7: **Centre wavelength of the SFG as a function of the laser repetition rate.** The single photon was replaced by the weak coherent state to perform this experiment. The error bars are smaller than the data points.

Recall that the chirped pulses are created by applying a quadratic frequency dependent phase, $\phi(\nu) = \frac{1}{2}|\beta_2|(\nu - \nu_0)^2$. The chirp rate, the rate of change of the instantaneous frequency with time, is $2\pi/|\beta_2|$. Thus we expect that a change in time of Δt will cause a change in the frequency $d\nu = \frac{2\pi}{|\beta_2|} d\Delta t$. We can then convert Eq. 6.23 to

$$\frac{d\nu}{dR} = -\frac{2\pi n}{|\beta_2| R^2} \tag{6.24}$$

$$\frac{d\lambda}{dR} = \left(\frac{\lambda^2}{c}\right) \frac{2\pi n}{|\beta_2| R^2}. \tag{6.25}$$

Substituting $\lambda = 400$ nm, $|\beta_2| = 52.4 \times 10^6$ fs^2, $R = 80$ MHz gives

$$\frac{d\lambda}{dR} \sim 0.01 n \frac{nm}{kHz}. \tag{6.26}$$

We expect this to become significant in our experiment when the change in wavelength approaches that of the linewidth of our single photon, 0.04 nm. For $n = 12$, this occurs when $\Delta R = 300$ Hz. With the repetition rate stabilization feature on our Spectra Physics Tsunami (*Lok-to-Clock*), this is limited to $\Delta R < 10$Hz and does not constitute a significant source of spectral broadening.

To estimate n in our experiment, we use the slope of the center wavelength versus the relative delay, and the one of the center wavelength in function of the repetition rate. From Fig. 6.3, we have $\frac{d\lambda}{dt_1'} = (-0.0641 \pm 0.0001)$ nm/ps $= \frac{d\lambda}{dt_3}$, where $t_3 = t_2 + n/R$. Additionally, we have that $\frac{d\lambda}{dR} = (0.1188 \pm 0.0004)$ nm/kHz from the slope of Fig. 6.7. Using the chain rule for $\frac{d}{dR} = \frac{dt_3}{dR}\frac{d}{dt_3}$, we find $\frac{d\lambda}{dR} = -\frac{d\lambda}{dt_3}\frac{n}{R^2}$ and hence

$$n = \left(\frac{d\lambda}{dt_3}\right)^{-1} \left(\frac{d\lambda}{dR}\right) R^2 = 11.9 \pm 0.1. \tag{6.27}$$

As expected from the lengths in our experiment, the strong laser pulse arriving at the nonlinear crystal from path 2 originates 12 pulses later than the single photon from path one.

Experiment 2

Throughout the experiments described in this chapter, we employed the repetition rate locking feature on our Ti:Sapphire laser to maintain a constant repetition rate. We took

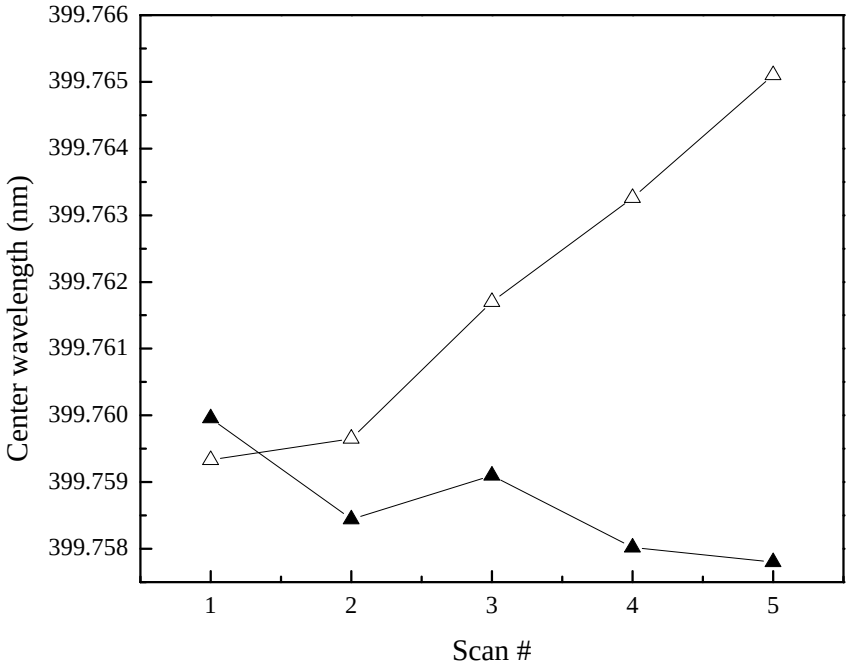

Figure 6.8: **Lok-to-Clock feature off.** The filled triangles correspond to the case when the locking feature is on, and the empty triangles when the feature is not activated. Each scan is 10 minutes long. The shift in the central position in the case without the Lok-to-Clock is caused by a 50 Hz detuning. The error bars are smaller than the data points.

two sets of data, one with stabilization on, the other with it off. The results are shown in Fig. 6.8. For each set, we measured the peak position of the upconverted weak coherent state, with a 10 min. acquisition time and repeated five times. The data show that the center wavelength drifts significantly without stabilization.

Chapter 7

Conclusion and Outlook

This dissertation was divided in two parts. In the first one, I described the use of a multi-partite source of photonic qubits for the study of quantum nonlocality, bound entanglement and one-way quantum computing. The second part focused on a novel interface for quantum frequency conversion and waveform manipulation of single photons using chirped-pulse upconversion.

Photonic qubits are versatile resources for quantum information processing, but designing and aligning efficient SPDC sources is challenging. Important figures of merit are the fidelity with a target state, and rates at which such states are produced. Throughout this dissertation, SPDC sources have been put together in different arrangements and with a constant aim at improving alignments and collection efficiencies. Figure 7.1 summarizes different architectures that we have used with similar pump power ($\sim$800 mW). Each panel shows the two-fold rates, with qubits in their required polarisation states, and the detected four-fold rates of the final target quantum states, with indicated fidelity. Photons were spectrally filtered directly at the source, within 3 nm of bandwidth. Although the nonlinear crystals remained the same (1 mm BBO, Type-I phase matching), coincidence rates kept increasing. Improvement of rates between GHZ-1, GHZ-2 and GHZ-3 is a result of refined collection efficiencies, careful transverse walk-off compensations and optimized layout.

Our first use of the multi-partite source of photonic qubits, described in Chapter 3, was

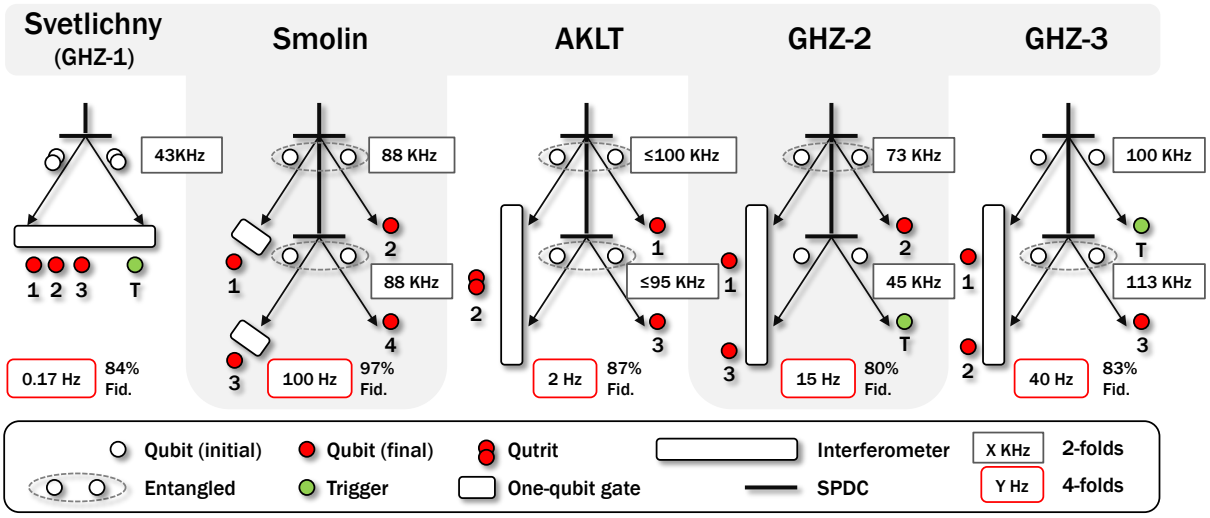

Figure 7.1: **Metamorphosis of our multi-partite photonic qubits source.** Parametric downconversion in bulk crystals is a reliable source of photonic qubits, as demonstrated in this thesis. Entangled states of different nature are generated using pairs of BBO crystals (SPDC). For the violation of Svetlichny's inequality in Chapter 3, GHZ states (GHZ-1) were produced from double pair emissions and an interferometer. Smolin bound entangled states were created from two separated Bell states, and local unitaries. AKLT states also started with Bell states, but an interferometer projected qubits onto a qutrit subspace. GHZ states were produced at much higher rates (15 Hz for GHZ-2 and 40 Hz for GHZ-3) using two separated sources. For each configuration, two-fold rates are given without polarisation analyzers, and with the pump in its final polarisation state. Four-folds are final and represent the rate at which the target state is detected.

in producing three-partite GHZ states of the form $\frac{1}{\sqrt{2}}(|HHV\rangle + |VVH\rangle)$. Double pair emissions from one sandwich-BBO were sent to an interferometer to produce the state. We estimated the density matrix through QST and found $(84 \pm 1)\%$ overlap with the target state. By analyzing a set of correlations between measurement outcomes, we experimentally demonstrated violation of the original Svetlichny's inequality by 3.6 standard deviations, with a value of 4.51 ± 0.14. Violation of the inequality rules out a description in terms of hidden variable theories with at most two-particle nonlocality and confirms genuine nonlocality and true entanglement.

Our next subject covered in Chapter 4 involved generating Smolin bound entangled states. Another pair of BBO crystals was included to generate photonic states in four distinct spatial modes. We started with a state of the form $|\phi^+\rangle_{AB} \otimes |\phi^+\rangle_{CD}$ and applied a set of unitaries to A and B in a random fashion to generate the bound entanglement and demonstrate entanglement unlocking. The challenge was to satisfy both conditions that define bound entangled states: entanglement and nondistillability. We used an entanglement witness to certify entanglement and a separability test under bi-partite cuts for the latter. A level of white noise was adjusted to browse an entire family of Smolin states. Without additional noise, our state was entangled but contained negative PT eigenvalues, also encountered in the first attempts to generate experimental bound entanglement [136, 196]. We turned all PT eigenvalues firmly positive by adding a substantial amount of noise ($\sim 50\%$), while preserving entanglement in Smolin states. We have therefore experimentally verified the existence of bound entangled states with photonic qubits. In parallel and shortly after our experiment, bound entangled states were prepared using trapped ions [197] and continuous variables [198]. All of the above demonstrations elevate bound entanglement beyond being just a mathematical curiosity. Bound entangled states are a resource for private key sharing [199] that has yet to be demonstrated experimentally [40].

Chapter 5 covered our experimental simulation of AKLT states and their viability for measurement-based quantum computation. Photonic qubits with high purity were essential to generate qutrits via quantum interference on a beam-splitter and led to successful Qubit-Qutrit-Qubit photonic states with fidelity of 87%. To implement single-qubit quantum logic gates, we prepared several input states and operated around the main axes of the Bloch sphere with high $(92 \pm 4)\%$ average fidelity. Previous to our work, no resource states other

than cluster states had been implemented experimentally, to demonstrate measurement-based quantum computation. Shortly after, quantum computing was also demonstrated in four- and six-qubit entangled states, not in the cluster-state category [200].

While information processing in solid-state AKLT states is not yet achievable, one could explore added complexity to the computational AKLT chain by adding qutrits to our photonic states. For universal computation, however, it would also require additional wires and means to efficiently couple them. For example, one could "attach" independent wires with entangling gates, such as optical C-NOT gates [201]. On the other hand, expanding AKLT chains with inclusion of entangling gates reduces the success probability by a fair amount. Although such a scheme is possible, it would be extremely inefficient to work with, for practical reasons. A different approach was recently proposed to extend the 1D AKLT chain to two dimensions [202, 203, 204]. 2D AKLT state on an honeycomb lattice is composed of spin-3/2 particles and was shown to a be universal resource state for measurement-based quantum computing [205]. Its simplest valence-bond construction is depicted in Fig. 7.2, and would constitute an important experimental achievement if realised with photonic qubits. The projection (P: shown as a circle) onto a four-dimensional symmetric subspace is given by [205]

$$P = |\mathbf{0}\rangle\langle 000| + |\mathbf{1}\rangle\langle 111| + |\mathbf{2}\rangle\langle W| + |\mathbf{3}\rangle\langle W'|, \tag{7.1}$$

where $|W\rangle = \frac{1}{\sqrt{3}}(|001\rangle + |010\rangle + |100\rangle)$ and $|W'\rangle = \frac{1}{\sqrt{3}}(|110\rangle + |101\rangle + |011\rangle)$. In addition to a successful projection onto the four-dimensional subspace, a set of measurements would have to be implemented for information processing.

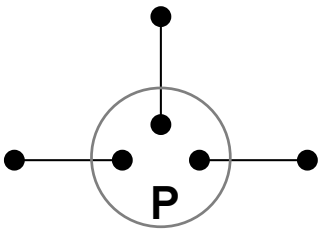

Figure 7.2: **2D AKLT state on honeycomb lattice.** A single site of the AKLT state on the honeycomb lattice is shown [205]. Projection (P) locates one spin 3/2 particle with dimension $d = 4$. This valence-bond solid representation could be constructed with photonic qubits (dark circles), paired in singlet states (edges).

To summarize, in the first part of this thesis, we have encoded quantum bits into the polarisation degrees of freedom of single photons. The multi-photon states generated shared quantum correlations, namely entanglement, which is a fundamental feature of quantum information science. With systematic actions on our prepared quantum states, mainly in the form of projective measurements, we were able to quantify the strength of those correlations, prove the existence of bound entanglement in nature, and demonstrate operations central to measurement-based quantum computing.

The second part of this thesis introduced a novel interface for quantum frequency conversion and waveform manipulation of single photons using chirped-pulse upconversion. In Chapter 6, single photons were produced by our source, chirped and upconverted inside a nonlinear crystal with the help of an oppositely-chirped strong laser pulse. We were able to compress the bandwidth of the single photon from 1740 GHz to 43 GHz. We demonstrated a tunability of the upconverted signal central frequency over 70 times the measured bandwidth, or by 130 times if taking into account the finite resolution of our spectrometer. We brought the fascinating process of classical chirped-pulse upconversion to the quantum regime, and contributed to the ongoing field of quantum frequency conversion and waveform manipulation at the single photon level.

The main challenge encountered for this experiment was to eliminate noise background.

One major source of noise is SHG from the strong laser beam which generates light that overlap spectrally with the upconverted signal bandwidth. Non-collinear upconversion configuration and choosing the signal photon wavelength longer than the laser pulse wavelength was effective at reducing the noise. Cutting the spectral tail of the strong beam above 800 nm further decreased stray light at 400 nm. Finally, residual light from the strong beam and signal were separated from the SFG by dichroic mirrors and a bandpass optical filter was used to remove all left-over second-harmonic radiations of the strong laser beam. We obtained very low noise count rates of 100 counts/sec as measured with the PMT.

Two additional features were not demonstrated but should be included in future directions. The first one consists of polarisation-independent upconversion detection [206, 182]. For example, one could use a pair of nonlinear crystals similar to our down-conversion scheme, a linear double-pass configuration [207] or a Sagnac interferometer [208]. Secondly, although we have shown that our interface conserved strong temporal correlations characteristic to SPDC, further investigation of the statistical properties of the upconverted photon would reveal its true single-photon nature. For example, one could measure the second order correlation function of the upconverted signal in a "triggered experiment" [209], by measuring the anticorrelation between detections occurring on both output of a beam splitter.

With viable improvements to the setup presented in Chapter 6, higher conversion efficiencies would be attainable. The efficiency of the upconversion process in our experiment is 0.06% with 300 mW of average power for the strong beam. Low efficiency is mainly due to the decrease in peak power after dispersion. One major achievement would be to "beat the filter", by showing an overall conversion efficiency higher than what a passive filter would do, neglecting frequency conversion. One achieves a net gain once the efficiency is greater than about $\eta_F \times 100\%$, where η_F is the ratio of the final to initial bandwidth. In our case, the target efficiency would be just over 2.5%. Significantly higher efficiency could be achieved with the use of crystals with periodic poling [210], for quasi-phase-matching, and higher pump powers. However, this is practically hard to implement, especially because of the low power threshold of poled crystals and their narrow acceptance bandwidth.

An interesting alternative approach could combine chirp-pulse upconversion with dif-

ference frequency generation (DFG) [190]. DFG was recently used to convert 910 nm single photons emitted from a quantum dot to 1,560 nm telecommunication band using a PPLN waveguide and a pulsed pump source at 2,200 nm [211]. This technique has not been exploited yet for spectral compression at the single photon level. For the proposed chirped-pulse DFG scheme (potentially all-fiber), both the signal photon and strong laser beam would undergo positive dispersion in long optical fibers, avoiding limitations of a grating-based system. Laser power might have to be lower to avoid nonlinear effects in the fiber, but one could compensate with the high conversion efficiency possible with integrated nonlinear waveguides [212]. If bulk crystals are used instead, one could amplify the laser intensity after dispersion, a technique commonly used in chirped pulse amplification systems [213]. Integrated optics or the use of poled material might introduce new sources of noise [214], not encounter in this thesis.

Whereas the primary interest of our chirp-pulse upconversion technique has been towards translating the central frequency of single photons to a tunable higher frequency, while narrowing spectral bandwidth, the results obtained here suggest a number of potential future directions. For example, tunability from one single wavepacket and a dynamic delay (see Fig. 6.3) could be replaced by a chain of wavepackets, with fix delays, to increase the transmission bandwidth of quantum communication systems. Each wavepacket could hold information in the form of amplitude modulations, angular momentum or polarisation states of light. Ignoring spectrometer resolution and given our measured parameters (σ_P, σ_L, and $|\beta_2|$), one could compact 155 wavepackets within a range of just 42 ps and engender the same number of distinguishable spectral peaks. Such an approach will open the door to temporal multiplexing and wavelength demultiplexing of quantum states of light.

List of publications

1. J. M. Donohue, M. Agnew, J. Lavoie and K. J. Resch, *Coherent ultrafast measurement of time-bin encoded photons*, accepted for publication in Phys. Rev. Lett (2013)

2. J. M. Arrazola, O. Gittsovich, J. M. Donohue, J. Lavoie, K. J. Resch and N. Lütkenhaus, *Reliable Entanglement Verification*, Phys. Rev. A **87**, 062331 (2013)

3. J. Lavoie, J. M. Donohue, L. Wright, A. Fedrizzi and K. J. Resch, *Spectral compression of single photons*, Nature Photonics **7**, 363-366 (2013)

4. J. Lavoie, J. M. Donohue, L. G. Wright, A. Fedrizzi and K. J. Resch, *Bandwidth Compression of Single Photons using Chirped Laser Pulses*, in Frontiers in Optics Conference, OSA Technical Digest (online) (Optical Society of America, 2012)

5. R. Prevedel, K. M. Schreiter, J. Lavoie and K. J. Resch, *A classical analogue for Franson dispersion cancellation with local detection*, Phys. Rev. A **84**, 051803(R) (2011)

6. T.-C. Wei, J. Lavoie and R. Kaltenbaek, *Creating multi-photon polarization bound-entangled states*, Phys. Rev. A **83**, 033839 (2011)

7. J. Lavoie, R. Kaltenbaek, M. Piani and K.J. Resch, *Experimental bound entanglement?*, Nature Physics **6**, 827 (2010)

8. R. Kaltenbaek, J. Lavoie, B. Zeng, S. D. Bartlett and K. J. Resch, *Optical one-way quantum computing with a simulated valence-bond solid*, Nature Physics **6**, 850 (2010)

9. J. Lavoie, R. Kaltenbaek, M. Piani and K. J. Resch, *Experimental bound entanglement in a four-photon state*, Phys. Rev. Lett. **105**, 130501 (2010)

10. J. Lavoie, R. Kaltenbaek and K. J. Resch, *Experimental violation of Svetlichnys inequality*, New J. Phys. **11**, 073051 (2009)

11. K. J. Resch, R. Kaltenbaek, J. Lavoie and D. N. Biggerstaff, *Chirped-pulse interferometry with finite frequency correlations*, Proceedings of SPIE **7465**, 74650N (2009)

12. R. Kaltenbaek, J. Lavoie and K. J. Resch, *Classical analogues of two-photon quantum interference*, Phys. Rev. Lett. **102**, 243601 (2009)

13. J. Lavoie, R. Kaltenbaek and K. J. Resch, *'Quantum-optical coherence tomography' with classical light*, Optics Express **17**, 3818 (2009)

14. R. Kaltenbaek, J. Lavoie, D. N. Biggerstaff and K. J. Resch, *Quantum-inspired interferometry with chirped laser pulses*, Nature Physics **4**, 864 (2008)

References

[1] Saleh, B. E. & Teich, M. C. *Fundamentals of photonics* (John Wiley & Sons, Inc New Jersey, 2007), 2 edn.

[2] Nielsen, M. & Chuang, I. *Quantum Computation and Quantum Information* (Cambridge Univ. Press, Cambridge, 2000).

[3] Bouwmeester, D., Ekert, A. K., Zeilinger, A. *et al. The physics of quantum information*, vol. 38 (Springer Berlin, 2000).

[4] Phillip, K., Laflamme, R. & Mosca, M. *An introduction to quantum computing* (Oxford University Press, New York, 2007).

[5] Jaeger, G. *Quantum information: An overview* (Springer Science+ Business Media, 2007).

[6] Shor, P. W. Polynomial-time algorithms for prime factorization and discrete logarithms on a quantum computer. *SIAM J. Comput.* **26**, 1484–1509 (1997).

[7] Grover, L. K. A fast quantum mechanical algorithm for database search. In *Proceedings of the twenty-eighth annual ACM symposium on Theory of computing*, 212–219 (ACM, 1996).

[8] Feynman, R. P. Simulating physics with computers. *Int. J. Theor. Phys.* **21**, 467–488 (1982).

[9] DiVincenzo, D. P. The physical implementation of quantum computation. *arXiv preprint quant-ph/0002077* (2000).

[10] Barenco, A. *et al.* Elementary gates for quantum computation. *Phys. Rev. A* **52**, 3457 (1995).

[11] Preskill, J. Reliable quantum computers. *Proceedings of the Royal Society of London. Series A: Mathematical, Physical and Engineering Sciences* **454**, 385–410 (1998).

[12] Benhelm, J., Kirchmair, G., Roos, C. F. & Blatt, R. Towards fault-tolerant quantum computing with trapped ions. *Nature Physics* **4**, 463–466 (2008).

[13] Weber, J. *et al.* Quantum computing with defects. *Proceedings of the National Academy of Sciences* **107**, 8513–8518 (2010).

[14] Simmons, S. *et al.* Entanglement in a solid-state spin ensemble. *Nature* **470**, 69–72 (2011).

[15] Clarke, J. & Wilhelm, F. K. Superconducting quantum bits. *Nature* **453**, 1031–1042 (2008).

[16] Ralph, T. C. & Pryde, G. J. Optical quantum computation. *Progress in Optics* **54**, 209–269 (2010).

[17] Bennett, C. H. & Wiesner, S. J. Communication via one-and two-particle operators on Einstein-Podolsky-Rosen states. *Phys. Rev. Lett.* **69**, 2881–2884 (1992).

[18] Mattle, K., Weinfurter, H., Kwiat, P. G. & Zeilinger, A. Dense coding in experimental quantum communication. *Phys. Rev. Lett.* **76**, 4656–4659 (1996).

[19] Barreiro, J. T., Wei, T.-C. & Kwiat, P. G. Beating the channel capacity limit for linear photonic superdense coding. *Nature Physics* **4**, 282–286 (2008).

[20] Bennett, C. H. *et al.* Teleporting an unknown quantum state via dual classical and Einstein-Podolsky-Rosen channels. *Phys. Rev. Lett.* **70**, 1895–1899 (1993).

[21] Bouwmeester, D. *et al.* Experimental quantum teleportation. *Nature* **390**, 575–579 (1997).

[22] Bennett, C. H., Brassard, G. *et al.* Quantum cryptography: Public key distribution and coin tossing. In *Proceedings of IEEE International Conference on Computers, Systems and Signal Processing*, vol. 175 (Bangalore, India, 1984).

[23] Gisin, N., Ribordy, G., Tittel, W. & Zbinden, H. Quantum cryptography. *Rev. Mod. Phys.* **74**, 145–195 (2002).

[24] Einstein, A., Podolsky, B. & Rosen, N. Can Quantum-Mechanical Description of Physical Reality Be Considered Complete? *Phys. Rev.* **47**, 777–780 (1935).

[25] Redhead, M. *Incompleteness, Nonlocality, and Realism* (Oxford University Press, 1987).

[26] Scheibe, E. *The logical analysis of quantum mechanics* (Chapter I, Pergamon Press, 1973).

[27] Bell, J. S. On the Einstein Podolsky Rosen Paradox. *Physics* **1**, 195–200 (1964).

[28] Clauser, J. F., Horne, M. A., Simony, A. & Holt, R. A. Proposed Experiment to Test Local Hidden-Variable Theories. *Phys. Rev. Lett.* **23**, 880–884 (1969).

[29] Aspect, A., Dalibard, J. & Roger, G. Experimental Test of Bell's Inequalities Using Time- Varying Analyzers. *Phys. Rev. Lett.* **49**, 1804–1807 (1982).

[30] Tittel, W., Brendel, J., Zbinden, H. & Gisin, N. Violation of Bell Inequalities by Photons More Than 10 km Apart. *Phys. Rev. Lett.* **81**, 3563–3566 (1998).

[31] Weihs, G., Jennewein, T., Simon, C., Weinfurter, H. & Zeilinger, A. Violation of Bell's Inequality under Strict Einstein Locality Conditions. *Phys. Rev. Lett.* **81**, 5039–5043 (1998).

[32] Matsukevich, D. N., Maunz, P., Moehring, D. L., Olmschenk, S. & Monroe, C. Bell Inequality Violation with Two Remote Atomic Qubits. *Phys. Rev. Lett.* **100**, 150404 (2008).

[33] Rowe, M. A. *et al.* Experimental violation of a Bell's inequality with efficient detection. *Nature* **409**, 791–794 (2001).

[34] Mermin, N. D. Extreme quantum entanglement in a superposition of macroscopically distinct states. *Phys. Rev. Lett.* **65**, 1838–1840 (1990).

[35] Svetlichny, G. Distinguishing three-body from two-body nonseparability by a Bell-type inequality. *Phys. Rev. D* **35**, 3066–3069 (1987).

[36] Brunner, N., Cavalcanti, D., Pironio, S., Scarani, V. & Wehner, S. Bell nonlocality. *arXiv:1303.2849* (2013).

[37] Gisin, N., Ribordy, G., Tittel, W. & Zbinden, H. Quantum cryptography. *Rev. Mod. Phys.* **74**, 145–195 (2002).

[38] Bennett, C. H. *et al.* Purification of Noisy Entanglement and Faithful Teleportation via Noisy Channels[Phys. Rev. Lett. 76, 722 (1996)]. *Phys. Rev. Lett.* **78**, 2031–2031 (1997).

[39] Horodecki, R. Bound entanglement - mysterious invention of nature. *Europhysics News* **41**, 21–24 (2010).

[40] Ozols, M., Smith, G. & Smolin, J. A. Bound entangled states with secret key and their classical counterpart. *ArXiv e-prints* (2013). 1305.0848.

[41] Eisaman, M. D., Fan, J., Migdall, A. & Polyakov, S. V. Invited Review Article: Single-photon sources and detectors. *Rev. Sci. Instrum.* **82**, 071101 (2011).

[42] Lounis, B. & Orrit, M. Single-photon sources. *Reports on Progress in Physics* **68**, 1129 (2005).

[43] O'Brien, J. L. Optical quantum computing. *Science* **318**, 1567–1570 (2007).

[44] Marcikic, I. *et al.* Distribution of Time-Bin Entangled Qubits over 50 km of Optical Fiber. *Phys. Rev. Lett.* **93**, 180502 (2004).

[45] Ursin, R. *et al.* Entanglement-based quantum communication over 144 km. *Nature Physics* **3**, 481–486 (2007).

[46] Nordholt, J. E., Hughes, R. J., Morgan, G. L., Peterson, C. G. & Wipf, C. C. Present and future free-space quantum key distribution. In *High-Power Lasers and Applications*, 116–126 (International Society for Optics and Photonics, 2002).

[47] Stucki, D. *et al.* High rate, long-distance quantum key distribution over 250 km of ultra low loss fibres. *New J. of Phys.* **11**, 075003 (2009).

[48] Sangouard, N., Simon, C., de Riedmatten, H. & Gisin, N. Quantum repeaters based on atomic ensembles and linear optics. *Rev. Mod. Phys.* **83**, 33–80 (2011).

[49] Żukowski, M., Zeilinger, A., Horne, M. A. & Ekert, A. K. "Event-ready-detectors" Bell experiment via entanglement swapping. *Phys. Rev. Lett.* **71**, 4287–4290 (1993).

[50] Knill, E., Laflamme, R. & Milburn, G. J. A scheme for efficient quantum computation with linear optics. *Nature* **409**, 46–52 (2001).

[51] Raussendorf, R. & Briegel, H. J. A One-Way Quantum Computer. *Phys. Rev. Lett.* **86**, 5188–5191 (2001).

[52] Nielsen, M. A. Optical Quantum Computation Using Cluster States. *Phys. Rev. Lett.* **93**, 040503 (2004).

[53] Walther, P. *et al.* Experimental one-way quantum computing. *Nature* **434**, 169–176 (2005).

[54] Prevedel, R. *et al.* High-speed linear optics quantum computing using active feed-forward. *Nature* **445**, 65–69 (2007).

[55] Boyd, R. W. *Nonlinear Optics* (Academic Press, 2008), 3 edn.

[56] Kumar, P. Quantum frequency conversion. *Optics Letters* **15**, 1476–1478 (1990).

[57] Huang, J. & Kumar, P. Observation of quantum frequency conversion. *Phys. Rev. Lett.* **68**, 2153–2156 (1992).

[58] Kimble, H. J. The quantum internet. *Nature* **453**, 1023–1030 (2008).

[59] Hadfield, R. H. Single-photon detectors for optical quantum information applications. *Nature Photonics* **3**, 696–705 (2009).

[60] Midwinter, J. E. & Warner, J. Up-Conversion of Near Infrared to Visible Radiation in Lithium-meta-Niobate. *J. Appl. Phys.* **38**, 519–523 (1967).

[61] Vandevender, A. P. & Kwiat, P. G. High efficiency single photon detection via frequency up-conversion. *Journal of Modern Optics* **51**, 1433–1445 (2004).

[62] Roussev, R. V., Langrock, C., Kurz, J. R. & Fejer, M. Periodically poled lithium niobate waveguide sum-frequency generator for efficient single-photon detection at communication wavelengths. *Optics Letters* **29**, 1518–1520 (2004).

[63] Albota, M. A. & Wong, F. N. Efficient single-photon counting at 1.55 μm by means of frequency upconversion. *Optics Letters* **29**, 1449–1451 (2004).

[64] Pelc, J. *et al.* Cascaded frequency upconversion for high-speed single-photon detection at 1550 nm. *Optics Letters* **37**, 476–478 (2012).

[65] Tanzilli, S. *et al.* A photonic quantum information interface. *Nature* **437**, 116–120 (2005).

[66] Ou, Z. Efficient conversion between photons and between photon and atom by stimulated emission. *Phys. Rev. A* **78**, 023819 (2008).

[67] Radnaev, A. *et al.* A quantum memory with telecom-wavelength conversion. *Nature Physics* **6**, 894–899 (2010).

[68] Zaske, S. *et al.* Visible-to-telecom quantum frequency conversion of light from a single quantum emitter. *Phys. Rev. Lett.* **109**, 147404 (2012).

[69] Pelc, J. *et al.* Downconversion quantum interface for a single quantum dot spin and 1550-nm single-photon channel. *Optics Express* **20**, 27510–27519 (2012).

[70] McKinstrie, C., Harvey, J., Radic, S. & Raymer, M. Translation of quantum states by four-wave mixing in fibers. *Optics Express* **13**, 9131–9142 (2005).

[71] Raymer, M. G. & Srinivasan, K. Manipulating the color and shape of single photons. *Physics Today* **65**, 110000 (2012).

[72] Rakher, M. T. *et al.* Simultaneous Wavelength Translation and Amplitude Modulation of Single Photons from a Quantum Dot. *Phys. Rev. Lett.* **107**, 083602 (2011).

[73] Kielpinski, D., Corney, J. F. & Wiseman, H. M. Quantum Optical Waveform Conversion. *Phys. Rev. Lett.* **106**, 130501 (2011).

[74] Bloembergen, N. *Nonlinear Optics* (World Scientific Publishing, Singapore, 1996).

[75] Loudon, R. *The quantum theory of light* (Oxford, 2003), 3 edn.

[76] Born, M. & Wolf, E. *Principles of optics: electromagnetic theory of propagation, interference and diffraction of light* (1999), 7 edn.

[77] Diels, J.-C. & Rudolph, W. *Ultrashort Laser Pulse Phenomena* (Academic Press, 2006), 2 edn.

[78] Treacy, E. Optical pulse compression with diffraction gratings. *IEEE J. Quantum Electron.* **5**, 454–458 (1969).

[79] Freedman, S. J. & Clauser, J. F. Experimental Test of Local Hidden-Variable Theories. *Phys. Rev. Lett.* **28**, 938–941 (1972).

[80] Fry, E. S. & Thompson, R. C. Experimental Test of Local Hidden-Variable Theories. *Phys. Rev. Lett.* **37**, 465–468 (1976).

[81] Aspect, A., Grangier, P. & Roger, G. Experimental Realization of Einstein-Podolsky-Rosen-Bohm *Gedankenexperiment* : A New Violation of Bell's Inequalities. *Phys. Rev. Lett.* **49**, 91–94 (1982).

[82] Ou, Z. Y. & Mandel, L. Violation of Bell's Inequality and Classical Probability in a Two-Photon Correlation Experiment. *Phys. Rev. Lett.* **61**, 50–53 (1988).

[83] Shih, Y. H. & Alley, C. O. New Type of Einstein-Podolsky-Rosen-Bohm Experiment Using Pairs of Light Quanta Produced by Optical Parametric Down Conversion. *Phys. Rev. Lett.* **61**, 2921–2924 (1988).

[84] Tapster, P. R., Rarity, J. G. & Owens, P. C. M. Violation of Bell's Inequality over 4 km of Optical Fiber. *Phys. Rev. Lett.* **73**, 1923–1926 (1994).

[85] Kwiat, P. G. *et al.* New High-Intensity Source of Polarization-Entangled Photon Pairs. *Phys. Rev. Lett.* **75**, 4337–4341 (1995).

[86] Aspelmeyer, M. *et al.* Long-Distance Free-Space Distribution of Quantum Entanglement. *Science* **301**, 621–623 (2003).

[87] Resch, K. *et al.* Distributing entanglement and single photons through an intra-city, free-space quantum channel. *Optics Express* **13**, 202–209 (2005).

[88] Ursin, R. *et al.* Entanglement-based quantum communication over 144 km. *Nature Physics* **3**, 481–486 (2007).

[89] Kaltenbaek, R., Prevedel, R., Aspelmeyer, M. & Zeilinger, A. High-fidelity entanglement swapping with fully independent sources. *Phys. Rev. A* **79**, 040302 (2009).

[90] Greenberger, D. M., Horne, M. A., & Zeilinger, A. *Bells Theorem, Quantum Theory, and Conceptions of the Universe.* p. 73 (Kluwer Academics, Dordrecht, The Netherlands, 1989).

[91] Ardehali, M. Bell inequalities with a magnitude of violation that grows exponentially with the number of particles. *Phys. Rev. A* **46**, 5375–5378 (1992).

[92] Klyshko, D. N. The Bell and GHZ theorems: a possible three-photon interference experiment and the question of nonlocality. *Phys. Lett. A* **172**, 399403 (1993).

[93] Belinskiĭ, A. V. & Klyshko, D. N. Interference of light and Bell's theorem. *Phys. Usp.* **36**, 653 (1993).

[94] Żukowski, M. & Kaszlikowski, D. Critical visibility for N-particle Greenberger-Horne-Zeilinger correlations to violate local realism. *Phys. Rev. A* **56**, R1682–R1685 (1997).

[95] Gisin, N. & Bechmann-Pasquinucci, H. Bell inequality, Bell states and maximally entangled states for n qubits. *Phys. Lett. A* **246**, 1–6 (1998).

[96] Cabello, A. Bell's theorem with and without inequalities for the three-qubit Greenberger-Horne-Zeilinger and W states. *Phys. Rev. A* **65**, 032108 (2002).

[97] Gühne, O., Tóth, G., Hyllus, P. & Briegel, H. J. Bell Inequalities for Graph States. *Phys. Rev. Lett.* **95**, 120405 (2005).

[98] Scarani, V., Acìn, A., Schenck, E. & Aspelmeyer, M. Nonlocality of cluster states of qubits. *Phys. Rev. A* **71**, 042325 (2005).

[99] Leggett, A. J. Nonlocal Hidden-Variable Theories and Quantum Mechanics: An Incompatibility Theorem. *Found. Phys.* **33**, 1469–1493 (2003).

[100] Gröblacher, S. *et al.* An experimental test of non-local realism. *Nature* **446**, 871–875 (2007).

[101] Cereceda, J. L. Three-particle entanglement versus three-particle nonlocality. *Phys. Rev. A* **66**, 024102 (2002).

[102] Seevinck, M. & Uffink, J. Sufficient conditions for three-particle entanglement and their tests in recent experiments. *Phys. Rev. A* **65**, 012107 (2001).

[103] Mitchell, P., Popescu, S. & Roberts, D. Conditions for the confirmation of three-particle nonlocality. *Phys. Rev. A* **70**, 060101 (2004).

[104] Tóth, G., Gühne, O., Seevinck, M. & Uffink, J. Addendum to "Sufficient conditions for three-particle entanglement and their tests in recent experiments". *Phys. Rev. A* **72**, 014101 (2005).

[105] Ghose, S., Sinclair, N., Debnath, S., Rungta, P. & Stock, R. Tripartite Entanglement versus Tripartite Nonlocality in Three-Qubit Greenberger-Horne-Zeilinger-Class States. *Phys. Rev. Lett.* **102**, 250404 (2009).

[106] Seevinck, M. & Svetlichny, G. Bell-Type Inequalities for Partial Separability in N-Particle Systems and Quantum Mechanical Violations. *Phys. Rev. Lett.* **89**, 060401 (2002).

[107] Collins, D., Gisin, N., Popescu, S., Roberts, D. & Scarani, V. Bell-Type Inequalities to Detect True n-Body Nonseparability. *Phys. Rev. Lett.* **88**, 170405 (2002).

[108] Laskowski, W. & Żukowski, M. Detection of N-particle entanglement with generalized Bell inequalities. *Phys. Rev. A* **72**, 062112 (2005).

[109] Pan, J. W., Bouwmeester, D., Daniell, M., Weinfurter, H. & Zeilinger, A. Experimental test of quantum nonlocality in three-photon GreenbergerHorneZeilinger entanglement. *Nature* **403**, 515–519 (2000).

[110] Zhao, Z. *et al.* Experimental Violation of Local Realism by Four-Photon Greenberger-Horne-Zeilinger Entanglement. *Phys. Rev. Lett.* **91**, 180401 (2003).

[111] Walther, P., Aspelmeyer, M., Resch, K. J. & Zeilinger, A. Experimental Violation of a Cluster State Bell Inequality. *Phys. Rev. Lett.* **95**, 020403 (2005).

[112] Resch, K. J., Walther, P. & Zeilinger, A. Full Characterization of a Three-Photon Greenberger-Horne-Zeilinger State Using Quantum State Tomography. *Phys. Rev. Lett.* **94**, 070402 (2005).

[113] Peres, A. *Quantum Theory: Concepts and Methods*. pp 164–165 (Kluwer, Dordrecht, 1993).

[114] Kwiat, P. G., Waks, E., White, A. G., Appelbaum, I. & Eberhard, P. H. Ultrabright source of polarization-entangled photons. *Phys. Rev. A* **60**, R773–R776 (1999).

[115] Bouwmeester, D., Pan, J.-W., Daniell, M., Weinfurter, H. & Zeilinger, A. Observation of Three-Photon Greenberger-Horne-Zeilinger Entanglement. *Phys. Rev. Lett.* **82**, 1345–1349 (1999).

[116] Hong, C. K., Ou, Z. Y. & Mandel, L. Measurement of subpicosecond time intervals between two photons by interference. *Phys. Rev. Lett.* **59**, 2044–2046 (1987).

[117] de Burgh, M. D., Langford, N. K., Doherty, A. C. & Gilchrist, A. Choice of measurement sets in qubit tomography. *Phys. Rev. A* **78**, 052122 (2008).

[118] James, D. F. V., Kwiat, P. G., Munro, W. J. & White, A. G. Measurement of qubits. *Phys. Rev. A* **64**, 052312 (2001).

[119] Schrödinger, E. Die gegenwärtige Situation in der Quantenmechanik. *Die Naturwissenschaften* **23**, 807–812; 823–828; 844–849 (1935).

[120] Horodecki, R. *et al.* Quantum entanglement. *Rev. Mod. Phys.* **81**, 865–942 (2009).

[121] Ekert, A. K. Quantum cryptography based on Bell's theorem. *Phys. Rev. Lett.* **67**, 661–663 (1991).

[122] Jennewein, T. *et al.* Quantum Cryptography with Entangled Photons. *Phys. Rev. Lett.* **84**, 4729–4732 (2000).

[123] Bennett, C. H. *et al.* Concentrating partial entanglement by local operations. *Phys. Rev. A* **53**, 2046–2052 (1996).

[124] Bennett, C. H. *et al.* Mixed-state entanglement and quantum error correction. *Phys. Rev. A* **54**, 3824–3851 (1996).

[125] Horodecki, M., Horodecki, P. & Horodecki, R. Mixed-State Entanglement and Distillation: Is there a "Bound" Entanglement in Nature? *Phys. Rev. Lett.* **80**, 5239–5242 (1998).

[126] Yang, D. *et al.* Irreversibility for All Bound Entangled States. *Phys. Rev. Lett.* **95**, 190501 (2005).

[127] Piani, M. Relative Entropy of Entanglement and Restricted Measurements. *Phys. Rev. Lett.* **103**, 160504 (2009).

[128] Brandão, F. G. S. L. & Plenio, M. A Generalization of Quantum Steins Lemma. *Communications in Mathematical Physics* **295**, 791–828 (2010).

[129] Gühne, O. & Tóth, G. Entanglement detection. *Physics Reports* **474**, 1 – 75 (2009).

[130] Smith, G. & Yard, J. Quantum Communication with Zero-Capacity Channels. *Science* **321**, 1812–1815 (2008).

[131] Masanes, L. All Bipartite Entangled States Are Useful for Information Processing. *Phys. Rev. Lett.* **96**, 150501 (2006).

[132] Horodecki, K. *et al.* Secure Key from Bound Entanglement. *Phys. Rev. Lett.* **94**, 160502 (2005).

[133] Horodecki, K. *et al.* Low-Dimensional Bound Entanglement With One-Way Distillable Cryptography Key. In *IEEE Transactions on Information Theory*, vol. 54, 2621–2625 (2008).

[134] Piani, M. & Watrous, J. All Entangled States are Useful for Channel Discrimination. *Phys. Rev. Lett.* **102**, 250501 (2009).

[135] Kampermann, H. *et al.* Experimental generation of pseudo-bound-entanglement. *Phys. Rev. A* **81**, 040304(R) (2010).

[136] Amselem, E. & Bourennane, M. Experimental four-qubit bound entanglement. *Nat. Phys.* **5**, 748–752 (2009).

[137] Smolin, J. A. Four-party unlockable bound entangled state. *Phys. Rev. A* **63**, 032306 (2001).

[138] Augusiak, R. & Horodecki, P. Bound entanglement maximally violating Bell inequalities: Quantum entanglement is not fully equivalent to cryptographic security. *Phys. Rev. A* **74**, 010305 (2006).

[139] Tóth, G. & Gühne, O. Entanglement detection in the stabilizer formalism. *Phys. Rev. A* **72**, 022340 (2005).

[140] Pittenger, A. O. & Rubin, M. H. Convexity and the separability problem of quantum mechanical density matrices. *Linear Algebra and its Applications* **346**, 47–71 (2002).

[141] Hong, C. K., Ou, Z. Y. & Mandel, L. Measurement of subpicosecond time intervals between two photons by interference. *Phys. Rev. Lett.* **59**, 2044–2046 (1987).

[142] Kwiat, P. G., Waks, E., White, A. G., Appelbaum, I. & Eberhard, P. H. Ultrabright source of polarization-entangled photons. *Phys. Rev. A* **60**, R773–R776 (1999).

[143] Lavoie, J., Kaltenbaek, R. & Resch, K. J. Experimental violation of Svetlichny's inequality. *New J. Phys.* **11**, 073051 (2009).

[144] Schreiter, K. M. *et al.* Optical implementation of a unitarily correctable code. *Phys. Rev. A* **80**, 022311 (2009).

[145] Ježek, M. *et al.* Quantum inference of states and processes. *Phys. Rev. A* **68**, 012305 (2003).

[146] Jozsa, R. Fidelity for Mixed Quantum States. *J. Mod. Opt.* **41** (1994).

[147] Werner, R. F. Quantum states with Einstein-Podolsky-Rosen correlations admitting a hidden-variable model. *Phys. Rev. A* **40**, 4277–4281 (1989).

[148] Bennett, C. H. & DiVincenzo, D. P. Quantum information and computation. *Nature* **404**, 247–255 (2000).

[149] Raussendorf, R., Harrington, J. & Goyal, K. A fault-tolerant one-way quantum computer. *Ann. Phys. (N.Y.)* **321**, 2242 – 2270 (2006).

[150] Raussendorf, R., Harrington, J. & Goyal, K. Topological fault-tolerance in cluster state quantum computation. *New J. Phys.* **9**, 199 (2007).

[151] Vallone, G., Pomarico, E., De Martini, F. & Mataloni, P. One-way quantum computation with two-photon multiqubit cluster states. *Phys. Rev. A* **78**, 042335 (2008).

[152] Tokunaga, Y., Kuwashiro, S., Yamamoto, T., Koashi, M. & Imoto, N. Generation of High-Fidelity Four-Photon Cluster State and Quantum-Domain Demonstration of One-Way Quantum Computing. *Phys. Rev. Lett.* **100**, 210501 (2008).

[153] Biggerstaff, D. N. *et al.* Cluster-State Quantum Computing Enhanced by High-Fidelity Generalized Measurements. *Phys. Rev. Lett.* **103**, 240504 (2009).

[154] Gao, W.-B. *et al.* Experimental Realization of a Controlled-NOT Gate with Four-Photon Six-Qubit Cluster States. *Phys. Rev. Lett.* **104**, 020501 (2010).

[155] Browne, D. E. & Rudolph, T. Resource-Efficient Linear Optical Quantum Computation. *Phys. Rev. Lett.* **95**, 010501 (2005).

[156] Dawson, C. M., Haselgrove, H. L. & Nielsen, M. A. Noise thresholds for optical cluster-state quantum computation. *Phys. Rev. A* **73**, 052306 (2006).

[157] Nielsen, M. A. Cluster-state quantum computation. *Rep. Math. Phys.* **57**, 147–161 (2006).

[158] Bartlett, S. D. & Rudolph, T. Simple nearest-neighbor two-body hamiltonian system for which the ground state is a universal resource for quantum computation. *Phys. Rev. A* **74**, 040302 (2006).

[159] Gross, D., Flammia, S. T. & Eisert, J. Most Quantum States Are Too Entangled To Be Useful As Computational Resources. *Phys. Rev. Lett.* **102**, 190501 (2009).

[160] Verstraete, F. & Cirac, J. I. Valence-bond states for quantum computation. *Phys. Rev. A* **70**, 060302 (2004).

[161] Gross, D. & Eisert, J. Novel Schemes for Measurement-Based Quantum Computation. *Phys. Rev. Lett.* **98**, 220503 (2007).

[162] Gross, D., Eisert, J., Schuch, N. & Perez-Garcia, D. Measurement-based quantum computation beyond the one-way model. *Phys. Rev. A* **76**, 052315 (2007).

[163] Brennen, G. K. & Miyake, A. Measurement-Based Quantum Computer in the Gapped Ground State of a Two-Body Hamiltonian. *Phys. Rev. Lett.* **101**, 010502 (2008).

[164] Chen, X., Zeng, B., Gu, Z.-C., Yoshida, B. & Chuang, I. L. Gapped Two-Body Hamiltonian Whose Unique Ground State Is Universal for One-Way Quantum Computation. *Phys. Rev. Lett.* **102**, 220501 (2009).

[165] Verstraete, F., Murg, V. & Cirac, J. I. Matrix product states, projected entangled pair states, and variational renormalization group methods for quantum spin systems. *Adv. Phys.* **57**, 143–224 (2008).

[166] Affleck, I., Kennedy, T., Lieb, E. H. & Tasaki, H. Rigorous results on valence-bond ground states in antiferromagnets. *Phys. Rev. Lett.* **59**, 799–802 (1987).

[167] Popp, M., Verstraete, F., Martín-Delgado, M. A. & Cirac, J. I. Localizable entanglement. *Phys. Rev. A* **71**, 042306 (2005).

[168] Gross, D. & Eisert, J. Quantum computational webs. *Phys. Rev. A* **82**, 040303 (2010).

[169] Darmawan, A. S. & Bartlett, S. D. Optical spin-1 chain and its use as a quantum-computational wire. *Phys. Rev. A* **82**, 012328 (2010).

[170] Hagiwara, M., Katsumata, K., Affleck, I., Halperin, B. I. & Renard, J. P. Observation of S=1/2 degrees of freedom in an S=1 linear-chain Heisenberg antiferromagnet. *Phys. Rev. Lett.* **65**, 3181–3184 (1990).

[171] Buluta, I. & Nori, F. Quantum Simulators. *Science* **326**, 108–111 (2009).

[172] Lanyon, B. P. *et al.* Manipulating Biphotonic Qutrits. *Phys. Rev. Lett.* **100**, 060504 (2008).

[173] James, D. F. V., Kwiat, P. G., Munro, W. J. & White, A. G. Measurement of qubits. *Phys. Rev. A* **64**, 052312 (2001).

[174] Doherty, A. C., Gilchrist, A. & de Burgh, M. D. (2009). Unpublished.

[175] Kaltenbaek, R., Lavoie, J., Zeng, B., Bartlett, S. D. & Resch, K. J. Optical one-way quantum computing with a simulated valence-bond solid. *Nature Physics* **6**, 850–854 (2010).

[176] Duan, L., Lukin, M., Cirac, I. & Zoller, P. Long-distance quantum communication with atomic ensembles and linear optics. *Nature* **414**, 413–418 (2001).

[177] Hosseini, M., Sparkes, B., Campbell, G., Lam, P. & Buchler, B. High efficiency coherent optical memory with warm rubidium vapour. *Nature Commun.* **2**, 174 (2011).

[178] Huang, J. & Kumar, P. Observation of quantum frequency conversion. *Phys. Rev. Lett.* **68**, 2153–2156 (1992).

[179] Vandevender, A. P. & Kwiat, P. G. High efficiency single photon detection via frequency up-conversion. *J. Mod. Opt.* **51**, 1433–1445 (2004).

[180] Tanzilli, S., Tittel, W., Halder, M. & al. A photonic quantum information interface. *Nature* **437**, 116–120 (2005).

[181] Langrock, C. *et al.* Highly efficient single-photon detection at communication wavelengths by use of upconversion in reverse-proton-exchanged periodically poled LiNbO3 waveguides. *Opt. Lett.* **30**, 1725–1727 (2005).

[182] Ramelow, S., Fedrizzi, A., Poppe, A., Langford, N. & Zeilinger, A. Polarization-entanglement-conserving frequency conversion of photons. *Phys. Rev. A* **85**, 13845 (2012).

[183] McGuinness, H. J., Raymer, M. G., McKinstrie, C. J. & Radic, S. Quantum Frequency Translation of Single-Photon States in a Photonic Crystal Fiber. *Phys. Rev. Lett.* **105**, 093604 (2010).

[184] Dudin, Y. O. *et al.* Entanglement of Light-Shift Compensated Atomic Spin Waves with Telecom Light. *Phys. Rev. Lett.* **105**, 260502 (2010).

[185] Pelc, J. S. *et al.* Long-wavelength-pumped upconversion single-photon detector at 1550 nm: performance and noise analysis. *Optics Express* **19**, 21445–21456 (2011).

[186] Lvovsky, A. I., Sanders, B. C. & Tittel, W. Optical quantum memory. *Nature Photonics* **3**, 706–714 (2009).

[187] Liu, C., Dutton, Z., Behroozi, C. H. & Vestergaard Hau, L. Observation of coherent optical information storage in an atomic medium using halted light pulses. *Nature* **409**, 490–493 (2001).

[188] Raoult, F. *et al.* Efficient generation of narrow-bandwidth picosecond pulses by frequency doubling of femtosecond chirped pulses. *Opt. Lett.* **23**, 1117–1119 (1998).

[189] Osvay, K. & Ross, I. N. Efficient tuneable bandwidth frequency mixing using chirped pulses. *Opt. Commun.* **166**, 113–119 (1999).

[190] Veitas, G. & Danielius, R. Generation of narrow-bandwidth tunable picosecond pulses by difference-frequency mixing of stretched pulses. *J. Opt. Soc. Am. B* **16**, 1561–1565 (1999).

[191] Simon, C. *et al.* Quantum memories. *Eur. Phys. J. D.* **58**, 1–22 (2010).

[192] Reim, K. F. *et al.* Towards high-speed optical quantum memories. *Nature Photonics* **4**, 218–221 (2010).

[193] Eckstein, A., Brecht, B. & Silberhorn, C. A quantum pulse gate based on spectrally engineered sum frequency generation. *Optics Express* **19**, 13770–13778 (2011).

[194] Baek, S.-Y., Cho, Y.-W. & Kim, Y.-H. Nonlocal dispersion cancellation using entangled photons. *Optics Express* **17**, 19241–19252 (2009).

[195] Ramelow, S., Ratschbacher, L., Fedrizzi, A., Langford, N. K. & Zeilinger, A. Discrete Tunable Color Entanglement. *Phys. Rev. Lett.* **103**, 253601 (2009).

[196] Lavoie, J., Kaltenbaek, R., Piani, M. & Resch, K. J. Experimental bound entanglement? *Nature Physics* **6**, 827 (2010).

[197] Barreiro, J. T. *et al.* Experimental multiparticle entanglement dynamics induced by decoherence. *Nature Physics* **6**, 943–946 (2010).

[198] Diguglielmo, J. *et al.* Experimental Unconditional Preparation and Detection of a Continuous Bound Entangled State of Light. *Phys. Rev. Let.* **107**, 240503 (2011).

[199] Horodecki, K., Horodecki, M., Horodecki, P. & Oppenheim, J. Secure Key from Bound Entanglement. *Phys. Rev. Lett.* **94**, 160502 (2005).

[200] Gao, W.-B. *et al.* Experimental measurement-based quantum computing beyond the cluster-state model. *Nature Photonics* **5**, 117–123 (2011).

[201] Kiesel, N., Schmid, C., Weber, U., Ursin, R. & Weinfurter, H. Linear Optics Controlled-Phase Gate Made Simple. *Phys. Rev. Lett.* **95**, 210505 (2005).

[202] Wei, T.-C., Affleck, I. & Raussendorf, R. Affleck-Kennedy-Lieb-Tasaki State on a Honeycomb Lattice is a Universal Quantum Computational Resource. *Phys. Rev. Lett.* **106**, 070501 (2011).

[203] Wei, T.-C., Affleck, I. & Raussendorf, R. Two-dimensional Affleck-Kennedy-Lieb-Tasaki state on the honeycomb lattice is a universal resource for quantum computation. *Phys. Rev. A* **86**, 032328 (2012).

[204] Miyake, A. Quantum computational capability of a 2D valence bond solid phase. *Annals of Physics* **326**, 1656–1671 (2011).

[205] Kwek, L. C., Wei, Z. & Zeng, B. Measurement-Based Quantum Computing with Valence-Bond. *International Journal of Modern Physics B* **26**, 30002 (2012).

[206] Takesue, H., Diamanti, E., Langrock, C., Fejer, M. M. & Yamamoto, Y. 1.5- μm single photon counting using polarization-independent up-conversion detector. *Optics Express* **14**, 13067–13072 (2006).

[207] Steinlechner, F. *et al.* Phase-stable source of polarization-entangled photons in a linear double-pass configuration. *Optics Express* **21**, 11943 (2013).

[208] Fedrizzi, A., Herbst, T., Poppe, A., Jennewein, T. & Zeilinger, A. A wavelength-tunable fiber-coupled source of narrowband entangled photons. *Optics Express* **15**, 15377–15386 (2007).

[209] Grangier, P., Roger, G. & Aspect, A. Experimental evidence for a photon anticorrelation effect on a beam splitter: a new light on single-photon interferences. *EPL (Europhysics Letters)* **1**, 173 (1986).

[210] Myers, L. *et al.* Quasi-phase-matched optical parametric oscillators in bulk periodically poled LiNbO3. *JOSA B* **12**, 2102–2116 (1995).

[211] de Greve, K. *et al.* Quantum-dot spin-photon entanglement via frequency downconversion to telecom wavelength. *Nature* **491**, 421–425 (2012).

[212] Tanzilli, S. *et al.* On the genesis and evolution of Integrated Quantum Optics. *Laser & Photonics Reviews* **6** (2012).

[213] Strickland, D. & Mourou, G. Compression of amplified chirped optical pulses. *Optics Communications* **56**, 219–221 (1985).

[214] Pelc, J. S. *et al.* Long-wavelength-pumped upconversion single-photon detector at 1550 nm: performance and noise analysis. *Optics Express* **19**, 21445 (2011).